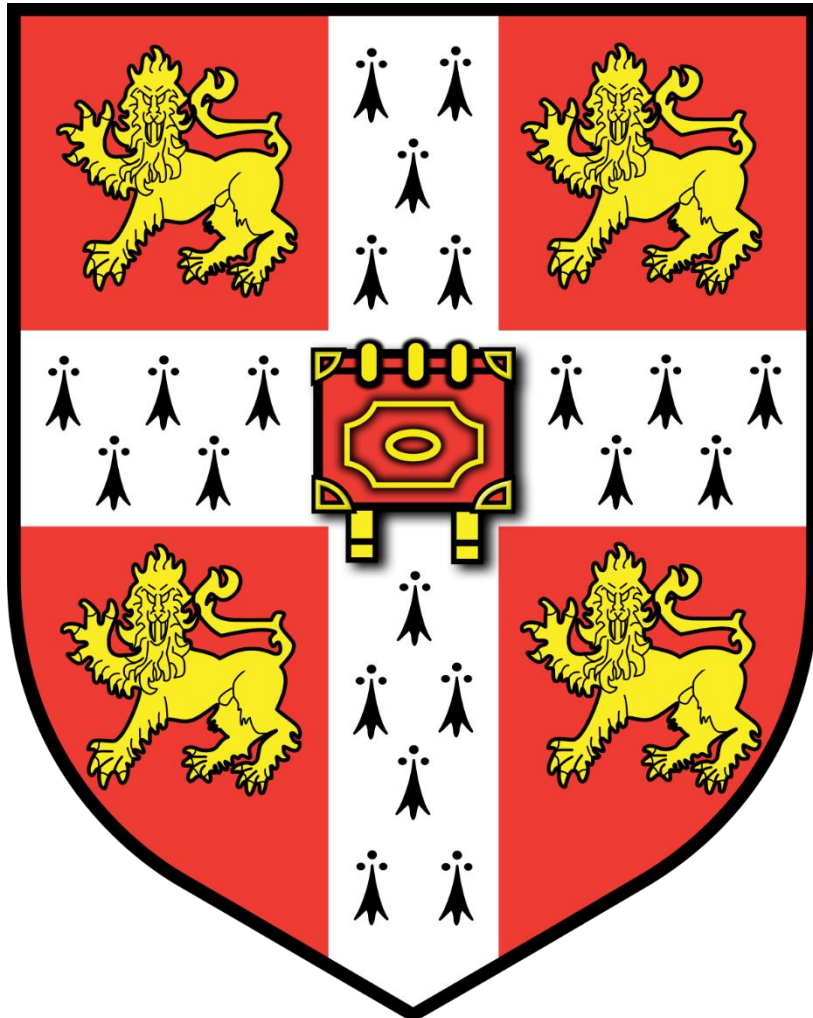


# In vitro reconstitution of Central Spindle Motility



**Samya Aich**

MRC Laboratory of Molecular Biology

Girton College

University of Cambridge

September 2021

This thesis is submitted for the degree of *Doctor of Philosophy*



# **PREFACE**

This dissertation is the result of my own work and includes nothing, which is the outcome of work done in collaboration except where specifically indicated in the text.

This work is not substantially the same as any that I have submitted, or is being concurrently submitted for a degree or diploma, or other qualification at the University of Cambridge, or any other University or similar institution except as declared in the Preface and specified in the text. I further state that no substantial part of my dissertation has already been submitted, or is being concurrently submitted for any such degree, diploma or other qualification at the University of Cambridge or any other University or similar institution except as declared in the Preface and specified in the text. It does not exceed the prescribed word limit for the relevant Degree Committee.

## In vitro reconstitution of Central Spindle Motility

Samya Aich

Precise localisation of intracellular organelles impacts a myriad of cellular processes including cell motility, polarisation and mitosis. Positioning is actively controlled by organelle specific attachment, often involving dedicated motor proteins, to cytoskeletal network. While much is known about the biophysics of motors on isolated tracks, how the complex cytoskeleton topologies found in cells, such as antiparallel microtubule (MT) overlaps, can influence the steady state distribution of cargoes is not understood molecularly. For example, in dividing sensory organ precursor cells, the antiparallel MT overlap of the central spindle controls the asymmetric segregation of signalling endosomes containing fate determinants in only one daughter cell. A modest asymmetry in the density of microtubules within the antiparallel MT overlap of central spindle, with more MTs on the anterior side of the spindle, generates one order of magnitude higher (than the microtubule asymmetry) bias distribution of endosomes. How such moderate asymmetry in the cytoskeleton is translated by motor proteins to produce strong non-linear effects and how different endosomes respond to this asymmetry is unknown.

In this work, I have aimed to address both these questions by using a combination of *in vivo* imaging and *in vitro* reconstitution using purified proteins and micropatterning.

To address how different endosomes segregate on an asymmetric microtubule track I utilised knock-in Rab-GFP lines and internalised labelled anti-delta antibodies. Remarkably, a class of late endosomes containing anti-delta antibodies indeed partitioned symmetrically during mitosis even on an asymmetric central spindle. This suggested that endosome partitioning is dictated by both the microtubule track and the endosome specific motor proteins *in vivo*.

To gain insight into how the motor content affects endosome behaviour, particularly on defined microtubule network, I attempted to reconstitute the process *in vitro*. The central spindle, an interdigitated antiparallel microtubule structure, is formed by balanced activity between both motor and non-motor microtubule associating proteins (MAPS). To control the geometry of such antiparallel microtubule tracks I utilised an improved micropatterning technology and purified central spindle proteins. This combined approach successfully led to formation of asymmetric antiparallel overlaps akin to the central spindle for the first time

## **Acknowledgements**

This long, at times difficult, scientific journey would have been impossible without the constant support and encouragement of my supervisor, Dr. Emmanuel Derivery. His unfailing cheerfulness and guidance have been a key element in this journey. I would also like to acknowledge our collaborators, Dr. Radhika Subramnaiam and Dr. Masanori Mishima for providing key ingredients at crucial junctures during the project. I would like to thank my lab members, Joe, Vicente, Alice, Kerrie, Akaash and Sarah, for making the lab a delightful place to do science. I am grateful for the various inputs I have received from people across the floor, including my second supervisor, Dr. Simon Bullock and Dr. Paul Conduit, university supervisor.

I would like to thank all my friends here- Venkat, Sridhar, Rohit, Arjun, Shikhar, Nipun, Arthi, Bianka, Alicia for their constant efforts in keeping my spirits up. More than anyone else, great many thanks to Anushka, for her unflinching support over the past couple of months. I would like to thank Sangeet for her constant support during the revisions.

This journey wouldn't have been possible without the warmth and patience of my parents from afar. Though themselves facing a devastating pandemic, their care and adoration was my keen solace.

# Table of Contents

List of Abbreviations .....	8
Chapter 1: Introduction .....	10
Mechanisms of organelle inheritance .....	10
Segregation of ER and Golgi.....	11
Segregation of Mitochondria.....	12
Segregation of Endosomes .....	13
Function and Regulation of Kinesin-3 .....	19
Mechanochemical cycle of Kinesins.....	19
Distinctive properties of Kinesin-3.....	21
Determinants of Kinesin-3 processivity .....	22
Mechanism of auto-inhibition .....	24
Cargo specificity of Kinesin-3 .....	25
Track specificity of Kinesin-3.....	27
Assembly and function of the Central spindle.....	29
Organisation and origins of central spindle MTs .....	29
Stability of Central spindle .....	31
Molecular determinants of central spindle .....	32
Overview of PRC1 family of MAPs .....	32
Domain organisation of PRC1 .....	32
Localisation and Mitotic Functions of PRC1.....	33
Molecular mechanism of PRC1 action .....	34
PRC1 as a major protein interaction hub for central spindle assembly.....	37
Thesis Aims.....	43
Chapter 2.....	46
Materials and Methods.....	46
2.1. Protein Purification .....	46
2.2 Imaging.....	49
2.3 Coverslip Preparation.....	50
2.4 Photo-initiator synthesis.....	50
2.5 Optical design of UV-LED DMD illuminator .....	50
2.6 DMD based micropatterning of Microtubules.....	52
2.7 Gliding Assay .....	52
2.8. In vitro motility Assay .....	53
2.9 Preparation of Stabilised microtubules .....	53

2.10 Microtubule Polymerisation .....	54
2.11 Synthesis of Fibrinogen-Biotin .....	54
2.12 Cloning .....	55
2.13 Cell culture and transfection.....	56
2.14 Antibody uptake assay .....	56
2.15 Fly genotypes .....	56
2.16 Image analysis .....	57
Chapter 3.....	60
Delta segregation pattern changes during late chase .....	62
Rab7 marks sara endosomes .....	65
Golgi-derived vesicles and fast recycling endosomes are independent of delta endosomes.....	66
Summary .....	69
Chapter 4.....	70
Fibrinogen anchors offer high efficiency of micropatterning .....	72
Improved micropatterning of MTs.....	77
Ase1 forms long bundles MT networks .....	79
Summary .....	83
Chapter 5.....	85
Preparation of active Centralspindlin complex.....	85
Pavarotti accumulates as clusters at MT tip .....	88
Pavarotti induced changes in MT networks.....	92
Symmetric and Asymmetric overlaps organised by Pavarotti .....	95
Discussion.....	97
Chapter 6.....	100
Fascetto selectively recognises antiparallel overlaps .....	100
Klp3A is an active motor that accumulates as a cluster on microtubule tips.....	101
Feo and Klp3A forms a sliding competent complex in vitro .....	103
Feo and Klp3A inhibits plus end growth and regulates sliding .....	104
Feo and Klp3A regulate formation of stable overlap.....	106
Asymmetric antiparallel overlaps can be generated by patterned microtubule growth .....	109
Discussion.....	111
General Discussion and Future Directions.....	113
Endosomes at the central spindle.....	113
How to build a Central Spindle .....	114
Reconstituting central spindle motion.....	116
References .....	117

## List of Abbreviations

Ase1	Abnormal Spindle Elongation-1
BSA	Bovine Serum Albumin
CDK1	Cyclin Dependent Kinase-1
CLASP	Cytoplasmic Linker Associated Protein
CLIP-170	Cytoplasmic Linker protein of 170KDa
sCMOS	Scientific Complementary Metal Oxide Semiconductor
CYK-4	CYTOKinesis defective 4
EB1	End Binding protein 1
EMCCD	Electron Multiplying Charge Coupled Device
ER	Endoplasmic Reticulum
Feo	Fascetto
GAP	GTPase Activating Protein
k-fibre	Kinetochore fibre
KIF16B	Kinesin family protein 16B
KIF4A	Kinesin family protein 4A
KIF5B	Kinesin family protein 5B
Klp3A	Kinesin Like Protein 3A
Klp98A	Kinesin Like Protein 98A
MKLP1	Mitotic Kinesin-like Protein 1
MKLP2	Mitotic Kinesin-like Protein 2
MT	Microtubule
Pav	Pavarotti
PRC1	Protein Responsible for Cytokinesis-1
Rab	Ras Associated Binding protein
SOP	Sensory Organ Precursor
Tum	Tumbleweed
ZEN4	Zygotic epidermal Enclosure defective- 4



# Chapter 1: Introduction

At each cell division, cellular components are distributed between newly formed cells. Each newly formed cell must be able to process nutrients immediately and respond to cell-intrinsic and extrinsic cues. Aside from inheriting a complete set of chromosomal material, each daughter cell must be allotted a portion of cellular organelles to be functional. Consequences of failing to inherit an adequate portion of cellular organelles depend on both the identity of the organelle and the extent to which the organelle is lacking in the newly formed cell. Cells without endoplasmic reticulum (ER) are unlikely to survive but cells without a centrosome can rely upon de novo biogenesis (Babour et al., 2010; Warren and Wickner, 1996). Since most organelles originate from pre-existing organelles, a complete lack of an organelle would be catastrophic. However, partial loss of organelle abundance could be compensated by biogenesis (Carlton et al., 2020; Lowe and Barr, 2007). Despite the fundamental importance of organelle inheritance, how mitotic cells partition organelles to newly formed daughter cells remains poorly understood. How proper distribution of organelles is achieved during division, ensuring their inheritance, will be the focus of this part of the Introduction.

## Mechanisms of organelle inheritance

There are, in principle, two ways to achieve organelle partitioning depending on the copy number of organelle (Lowe and Barr, 2007; Warren and Wickner, 1996). First, for single or low copy number organelles, only an active mechanism, often relying on direct interaction of the organelle with cytoskeletal networks, guarantees equal inheritance. Active partitioning is typically exemplified by centrosomes and chromosomes which are duplicated and inherited actively by spindle movement. Second, in contrast to such active segregation machinery, organelles that exist in multiple copies can be partitioned passively provided they are distributed homogeneously throughout the cytoplasm and cytokinesis occurs along the equator. On average daughter cells would be expected to receive half of the original number of organelles present in the mother cell, though individual cells of the population deviate from the average. Considering each copy of the organelle is statistically independent and has a 50% chance of segregating into either of the two daughter cells, the resulting variance in copy number between daughter cells, termed binomial partitioning error, is inversely proportional to the original number of organelles in the mother cell (inversely proportional to the square root of the total number, to be exact) (Huh and Paulsson, 2011). Therefore, greater the initial number

of organelles, smaller the variance between daughter cells and more accurate the partitioning (Carlton et al., 2020; Goyal et al., 2011; Lowe and Barr, 2007). Herein, I briefly review aspects of partitioning of membrane-bound organelles, focusing on the Endoplasmic Reticulum (ER), golgi and mitochondria, and highlight the mechanisms that ensure symmetric and asymmetric segregation.

### Segregation of ER and Golgi

The stochastic approach of organelle partitioning suits networks of extended morphology, for instance, the ER, because it is spread homogenously across the cell volume (Warren and Wickner, 1996). Halving the cell volume during mitosis would expectedly lead to equal partitioning. In metazoans, the ER maintains extensive contacts with the microtubule (MT) cytoskeleton and is continuous with the outer membrane of the nuclear envelope (NE) (Kumar et al., 1995). NE breakdown during prophase severs the connection between ER and the outer membrane of the NE (Güttinger et al., 2009). Simultaneously phosphorylation of STIM-1, an ER resident integral membrane protein, inhibits its interaction with EB-1 and uncouples the ER from MTs (Smyth et al., 2012). Uncoupling from MTs results in an ER network absent from the spindle zone but present homogenously around it, ensuring equal inheritance (Lu et al., 2009; Puhka et al., 2007).

The two strategies for mitotic partitioning, stochastic and active segregation, are not mutually exclusive (Jongsma et al., 2015). Low copy number organelles can be transformed into multiple vesicles during division and partitioned without an active mechanism (Carlton et al., 2020). During interphase, the Golgi apparatus exists as a single or low copy number organelle and consists of cisternal structures composed of interlinked Golgi ribbons (Rios and Bornens, 2003; Tang et al., 2012; Wang et al., 2003). On entry into mitosis, the C-terminal Binding Protein - 1/Brefeldin-A ADP Ribosylation substrate (CtBP-1/BARS) unlinks the stacked cisternal structure into isolated tubular ribbons (Colanzi et al., 2007; Hidalgo Carcedo et al., 2004). Subsequently, these tubular ribbons of Golgi are vesiculated into multiple smaller vesicles during division (Acharya et al., 1998), which have been proposed to undergo stochastic partitioning (Jesch et al., 2001). Contradicting reports suggest an alternate mechanism of Golgi partitioning might exist that includes complete re-absorption of the Golgi into the ER during mitosis (Farmaki et al., 1999; Zaal et al., 1999). While controversy still shrouds the exact nature of Golgi inheritance (Barr, 2004), one striking experiment reveals that different aspects of Golgi organisation could follow different routes. Indeed, monopolar spindles inherited by only

one of the two daughter cells reform a mother cell-like stacked ribbon Golgi architecture while the other daughter cell assembles a series of poorly stacked, though transport competent, cisternae. When microinjected with tubulin and Golgi membrane extract exogenously, the original ribbon structure is re-established indicating at least a part of the Golgi apparatus is inherited in a spindle dependent manner in HeLa cells (Wei and Seemann, 2009).

### Segregation of Mitochondria

During cell division, mitochondria undergo prolific cycles of fission and fusion, changing from an interconnected tubular form to discrete particulate organelles (Mishra and Chan, 2014). Mitochondrial segregation must solve two challenges simultaneously- a) partitioning of mitochondria equally among daughter cells and b) meeting the metabolic demands of the dividing cell. Both these challenges are met by finely regulating the fission-fusion cycle. Fission is mediated by recruitment of Dynamin Related Protein-1 (DRP1), a GTPase that actively constricts the tubular mitochondrial network to yield discrete membrane bound organelles (Labbé et al., 2014). As the cell enters division, CDK-1 directly and Aurora indirectly phosphorylates DRP-1 to activate it (Kashatus et al., 2011; Taguchi et al., 2007). Along with potent activation of the fission machinery, mitochondrial fragmentation is also driven by inhibiting the fusion machinery composed of MFN-1, MFN-2 (for the outer membrane) and OPA-1 (for the inner membrane) (Park and Cho, 2012). Upon fragmentation the numerous resulting particles disperse across the cell volume surrounding the mitotic spindle. Homogenous distribution during mitosis, a pre-requisite for passive inheritance of these organelles, requires detachment from cytoskeletal filaments. Continued attachment of mitochondria with the mitotic spindle results in division failure (Chung et al., 2016). This is achieved by kinesin and dynein shedding triggered by Aurora A and CDK-1 respectively from the mitochondrial surface (Chung et al., 2016). Therefore, on mitotic entry, mitochondria are fragmented, decoupled from motors and dispersed along the entire cell volume regulated by CDK-1 and Aurora A. What mediates their inheritance?

Because fragmentation leads to a sharply increased copy number, mitochondria might be expected to partition passively according to cell volume. However, in fission yeast, mitochondria are observed to segregate by the spindle machinery in metaphase and accumulate at the spindle poles, contradicting a passive inheritance mechanism (Yaffe et al., 1996). Mitochondrial accumulation at the spindle poles has been proposed to be crucial for spindle orientation (Krüger and Tolić-Nørrelykke, 2008). Careful examination of mitochondrial

movements has recently uncovered a rapid, even redistribution of mitochondria from the spindle poles in late anaphase facilitating proportionate inheritance of mitochondrial volume according to cell volume (Jajoo et al., 2016). Although this suggests a passive inheritance mechanism, the observed partitioning errors are significantly lower than the expected binomial partitioning error, suggesting other control mechanisms may act to reduce partitioning errors arising from passive segregation (Jajoo et al., 2016). In mammalian cells, fragmented mitochondria have been observed to associate with dense “actin clouds” (Moore et al., 2021). Spontaneous symmetry breaking in these actin clouds leads to formation of propulsive actin comets that circulates mitochondria across the cell volume (Mitsushima, 2010; Moore et al., 2021). This unique actin-based circular movement, though redundant for symmetric inheritance, has been shown to be important for mitochondrial “shuffling”, where locally damaged or dysfunctional mitochondria, are mixed with functional mitochondria across the cell volume to yield functionally comparable mitochondria populations between daughter cells. Mitochondrial heterogeneity, caused by variability of its genome, proteome, age, and oxidative potential, is a key parameter of cellular physiology (Aryaman et al., 2017; Stewart and Chinnery, 2020). In particular, during asymmetric division of stem-like cells in human breast tissue, healthy mitochondrial population is predominantly inherited by the daughter cell retaining stem cell properties (Katajisto et al., 2015). This is supported by evidence in budding yeast asymmetric divisions, where aged mitochondria are preferentially retained in the mother cell, contributing to replicative ageing (McFaline-Figueroa et al., 2011). Therefore, whereas in symmetric divisions, mitochondria-associated actin waves ensure its homogenous distribution and inheritance, during asymmetric divisions, specialised mechanisms ensure mitochondrial heterogeneity between daughter cells.

### Segregation of Endosomes

The endo-lysosomal network is a collection of small membrane-bound organelles that control intracellular communication, sorting and intracellular trafficking. Given their sheer numbers, a stochastic partitioning mechanism has been proposed for endosomes (Bergeland et al., 2001; Dunster et al., 2002). Their functioning and even their existence during mitosis has long been doubted with common consensus towards complete inhibition of classical endocytosis upon entry into mitosis (Boucrot and Kirchhausen, 2007; Fielding et al., 2012; Hinze and Boucrot, 2018). Evidence from various cell types has led to a shift in perspective with general recognition of the undisputed role played by endosomes during later stages of cell division, in particular, cytokinesis (Albertson et al., 2005). However, even earlier during cell division,

Rab11 positive recycling endosomes congregate towards spindle poles and contribute to spindle organisation (Hehnly and Doxsey, 2014). Similar spindle pole mediated segregation has also been reported for peroxisomes, highlighting spindle pole separation as a major mode of organelle partitioning (Knoblauch and Rachubinski, 2016). Active partitioning strategies are pivotal for endosomes that direct cell signalling during development. Symmetric partitioning of signalling endosomes has been shown to propagate the levels of TGF $\beta$  signalling experienced by the mother cell to its daughter cells (Bokel et al., 2006), likely by associating with the spindle structure.

While polarized trafficking ensures symmetric organelle partitioning during mitosis, it also controls asymmetric organelle positioning during asymmetric cell division. During *Drosophila* sensory organ precursor (SOP) division, each SOP divides asymmetrically to produce two intrinsically dissimilar daughter cells- a notch-active posterior pIIa cell and a signal sending notch-inactive anterior pIIb cell (Hartenstein and Posakony, 1990; Rhyu et al., 1994). This notch signalling asymmetry between the two daughter cells is controlled by polarized trafficking of Sara (Smad Anchor for Receptor Activation) with redundant contribution from Rab11 recycling endosomes (Fig 1) (also see Chapter 3). Sara containing endosomes are a subset of Rab5 and PI3P positive multi-vesicular endosomes that contain internalised Delta and Notch even before SOP division (Coumailleau et al., 2009). During division endosomes containing Sara and endocytosed Notch and Delta are specifically targeted to the pIIa cell (300% enrichment into this cell) (Coumailleau et al., 2009; Derivery et al., 2015). Although it is not entirely clear whether this pool of Notch in the SOP reflect an activated signalling station, NICD (Notch IntraCellular Domain), a marker of activated notch, is rapidly lost from these endosomes soon after division suggesting that at least immediately after division Sara endosomes represent an active signalling entity (Coumailleau et al., 2009). Consequently, perturbations in asymmetric Sara endosome segregation leads to Notch-related fate phenotypes (Coumailleau et al., 2009; Derivery et al., 2015a; Loubéry and González-Gaitán, 2014; Loubéry et al., 2014). Thus, asymmetric segregation of Sara endosomes is important for directional notch signalling (Montagne and Gonzalez-Gaitan, 2014). How is this population of endosomes targeted specifically to one of the daughter cells?

Elegant work from Derivery et al., 2015 has shown that Sara containing endosomes are selectively targeted to anaphase-specific central spindle by the plus-end directed kinesin-3, Klp98A, mammalian orthologue of KIF16B. Once targeted to the central spindle, biased inheritance is achieved because the central spindle itself is asymmetric, with a higher MT

density on the pIIb side than the pIIa side of the cell (Fig. 1A, late anaphase). Using novel image-analysis algorithms and nanobody targeting, it was shown that central spindle asymmetry is controlled by the antagonistic relationship between MT depolymerising kinesin-13, Klp10A (Rogers et al., 2004) and negative end capping protein Patronin (Goodwin and Vale, 2010) (Fig 1A). Patronin is specifically enriched on the pIIb side and selectively stabilises central spindle MTs. Since central spindle MT plus ends point towards the equator, Klp98A mediated movement leads to biased partitioning of Sara endosomes into pIIa.

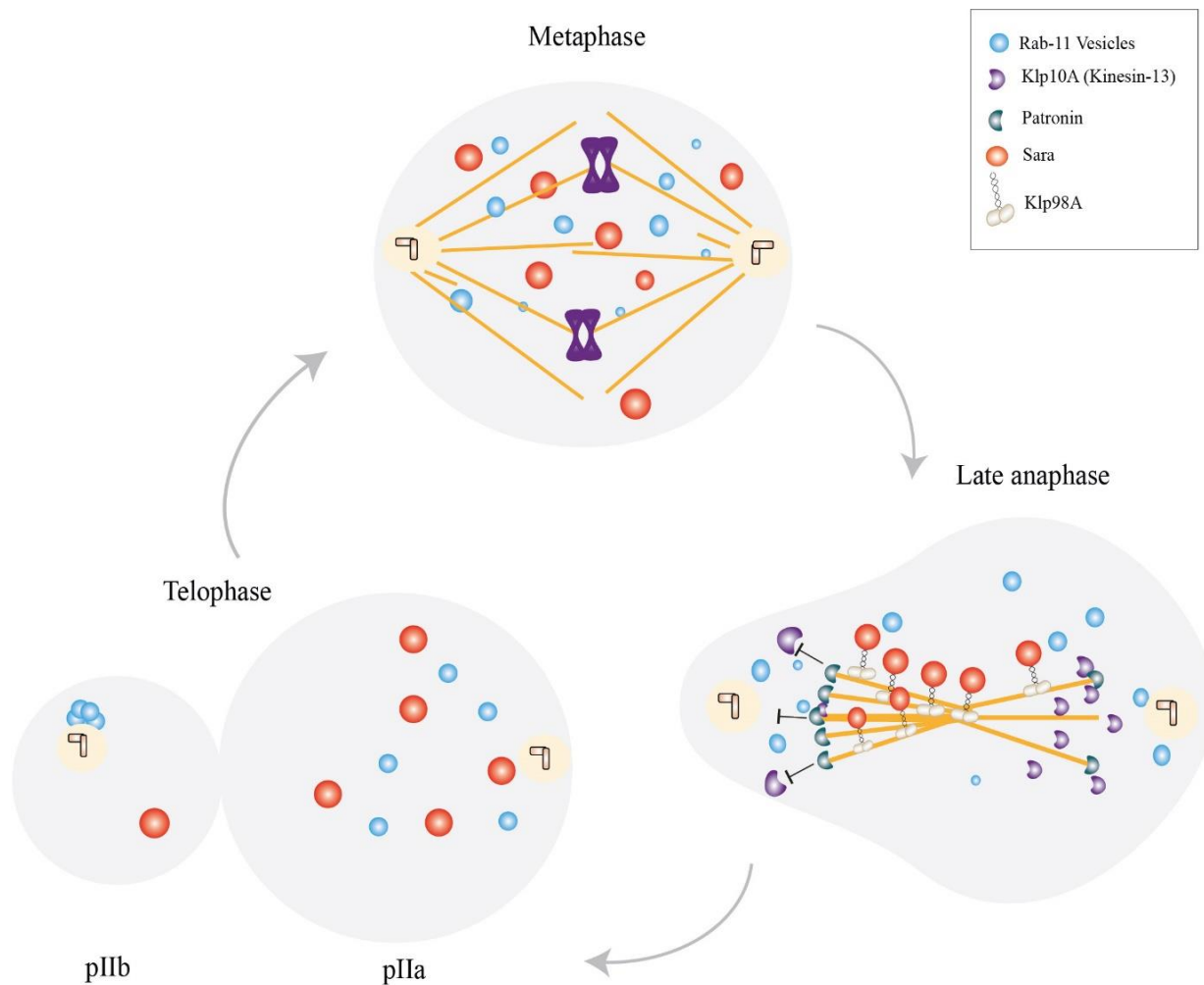


**Fig 1. Mechanism of Endosome movement.** During metaphase Sara endosomes (in red) are distributed around the cell along with Rab11 endosomes (in blue). In late anaphase, Kinesin-3, Klp98A recruits Sara endosomes onto the central spindle. The central spindle is asymmetric due to biased enrichment of Patronin on the pIIb side, counteracting MT depolymerase Klp10A. This results in higher tubulin intensity on the pIIb side. Consequently, higher number of Sara endosomes arrive in pIIa, driven by plus end-directed motion of Klp98A. Although the

exact nature of Rab11 segregation is unclear, in newly formed pIIb specifically, Rab11 forms a stable centrosome associated cluster.

---

Central spindle-based trafficking of endosomes is a completely new paradigm in our understanding of organelle partitioning. Asymmetric dispatch of Sara containing endosomes requires an asymmetric central spindle. If MT asymmetry of the central spindle is reversed, direction of asymmetric dispatch of endosomes also reverses. Similarly, if central spindle MTs are symmetric on either side, Sara containing endosomes partition symmetrically (Derivery et al., 2015). A theoretical model was proposed to explain how central spindle asymmetry controls asymmetric endosome dispatch (Derivery et al., 2015) (Fig 2). Central to this model is the MT asymmetry on either side of the central spindle (termed  $\rho_a$  on the pIIa side and  $\rho_b$  on the pIIb side). MT density on the pIIb side-  $\rho_b$ , is greater than MT density on the pIIa side-  $\rho_a$  ( $\rho_b > \rho_a$ ), and the resultant probability of endosomes on either side of the central spindle (denoted by  $P^{pIIb}$  and  $P^{pIIa}$  respectively) follows the equation-

$$\frac{P^{pIIa}}{P^{pIIb}} = \frac{\rho_b}{\rho_a} e^{\frac{v k_{on} l (\rho_b - \rho_a)}{D k_{off}}}$$

$l$  denotes the length of overlap of MTs at the central spindle,  $D$  denotes the diffusion coefficient of an endosome detached from the MT,  $v$  denotes the velocity of endosomes on MTs and  $k_{on}$ ,  $k_{off}$  denote rate constants of attachment to and detachment from MTs respectively.

The parameters  $v$ ,  $k_{on}$ ,  $k_{off}$  reflect properties of the kinesin-3 motor, Klp98A. Klp98A is responsible for carrying the endosomes at the central spindle (Derivery et al., 2015). The velocity of the kinesin motor along with its rate of MT attachment (on-rate) and rate of MT detachment (off-rate) determines the final distribution of Sara containing endosomes.

As mentioned above, partitioning of Sara containing endosomes during mitosis depends on the kinesin motors carrying such endosomes. Therefore, to understand how Sara containing endosomes are dispatched first requires a detailed understanding of the kinesin motor itself. In the following section, I describe the properties of kinesin-3 family of motors with a particular focus on the parameters described here namely, the velocity and the on and off-rate of the motor.

An asymmetric central spindle is central to asymmetric dispatch of Sara containing endosomes. Spindle targeting and biased dispatch of Sara endosomes is not restricted to SOP lineage of flies and has been generalised to intestinal stem cells in flies and neural precursors in zebrafish (Kressmann et al., 2015; Montagne and Gonzalez-Gaitan, 2014).

In the section titled “Assembly and function of the Central spindle”, I describe how the central spindle is built. Once again, I particularly focus on the parameters described in this section. I explore how the length of antiparallel overlap of MTs ( $l$ ) is controlled. I also describe where central spindle MTs originate from in an attempt to understand how MT density ( $\rho_b$  and  $\rho_a$ ) could be regulated.

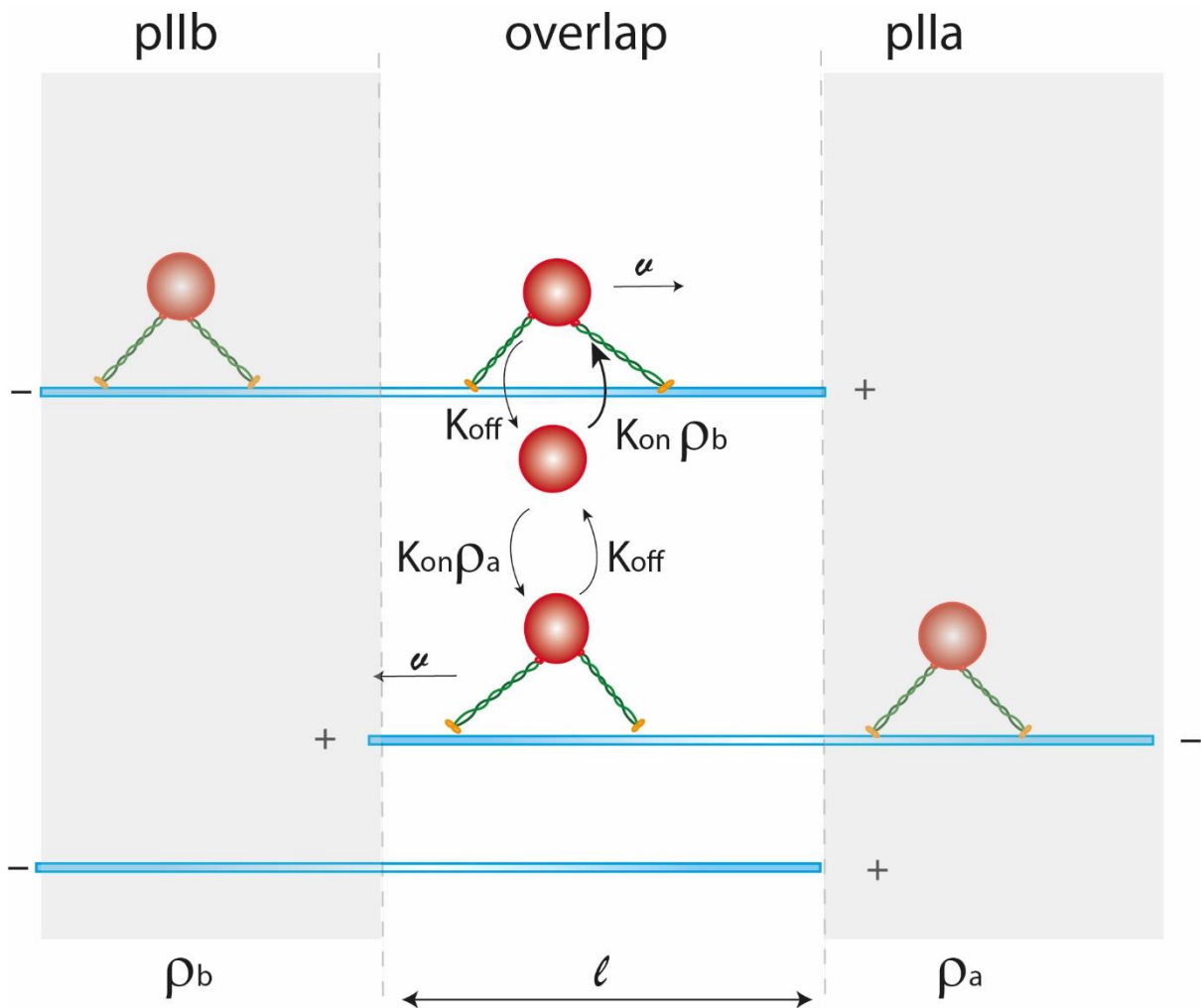


**Fig 2. Mechanism of Endosome movement.** At the central spindle MTs (in blue) from either side of the cell, pIIb and pIIa, interdigitate to form an antiparallel overlap of length  $\ell$ . MT densities at either side of the overlap is denoted by  $\rho_b$  and  $\rho_a$  respectively. Sara containing endosomes (in red) are targeted to the central spindle by kinesin-3 motor, Klp98A (in green). Endosomes detach from the MTs with a dissociation constant,  $k_{off}$ . Dissociated endosomes can either move away from the central spindle with a diffusion co-efficient D (not shown in the figure) or can reattach to the central spindle MTs. Reattachment can occur with an on rate  $k_{on}$   $\rho_b$  or  $k_{on} \rho_a$ . Because  $\rho_b > \rho_a$ , the former is the favoured option (see text for details).

# Function and Regulation of Kinesin-3

Intracellular transport of cargoes is powered by molecular motors, moving unidirectionally on cytoskeletal tracks. Transport of a vast variety of cargoes, involved in almost all cellular processes, from signal transduction to cell division, is mediated by three major classes of molecular motors- myosin, kinesin and dynein (Vale, 2003). Among these, microtubular transport is driven by the latter two, kinesin and dynein, with myosin transporting exclusively on actin filaments.

Kinesins constitute a large superfamily of proteins moving on MTs by ATP hydrolysis (Schnitzer and Block, 1997). Their functions range from intracellular transport of vesicles and organelles to controlling MT dynamics and mitosis (Hirokawa et al., 2009). Despite this wide-ranging functionality, all kinesins possess remarkably similar molecular organisation (Vale and Fletterick, 1997). Kinesins involved in intracellular transport contain- a) a motor head domain of approximately 360 amino acids, tasked with both nucleotide and MT bunding, b) a neck region, further composed of a neck-linker immediately following the motor domain and a neighbouring neck coil region facilitating dimerization and c) a motor specific tail region which binds to the cargo, either directly or through intermediary adaptor proteins (Cross, 2016; Vale and Fletterick, 1997). The motor domain, which has the highest conservation amongst the different family members, is composed of a central eight beta sheet barrel flanked on either side by three alpha helices, with a rather open nucleotide binding pocket (Hou et al., 2004; Kull et al., 1996; Rice et al., 1999). Minute structural changes upon ATP binding and hydrolysis at this small pocket, is amplified by the neck region to result in a forward motion (towards the plus end of MT) of the tail region (Asenjo et al., 2003; Hwang et al., 2008; Kozielski, 1997; Rice et al., 1999; Sindelar et al., 2002).

## Mechanochemical cycle of Kinesins

Since the discovery of kinesin-1, the founding member of this class of molecular motors, extensive research has focused on unravelling how the chemical energy released by ATP hydrolysis is converted into effective mechanical motion which allows the motor to move, on average  $\sim 1\mu\text{m}$  before detaching, towards the plus end of MTs (Vale et al., 1985a, 1985b). The mechanochemical cycle allowing for such robust transport requires efficient communication between the two head domains of the kinesin dimer, always keeping them out-of-phase in their respective motion cycles (Hackney, 1994) (Fig 3). Each motion cycle is characterised by periodic changes between strong (ATP bound and nucleotide free) and weak (ADP bound)

states of MT binding affinity (Hackney, 1988). Universally, for each ATP hydrolysed, kinesins take an 8nm step (Coy et al., 1999a; Schnitzer and Block, 1997). With kinesin-1 traversing an average ~1um before detachment, this means typically more than 100 successive steps are taken by the dimeric motor before falling off the MT. Such effective transport requires that during the period of motion, at least one head of dimeric kinesins remain bound to the MT (bound head)(Hancock and Howard, 1999).

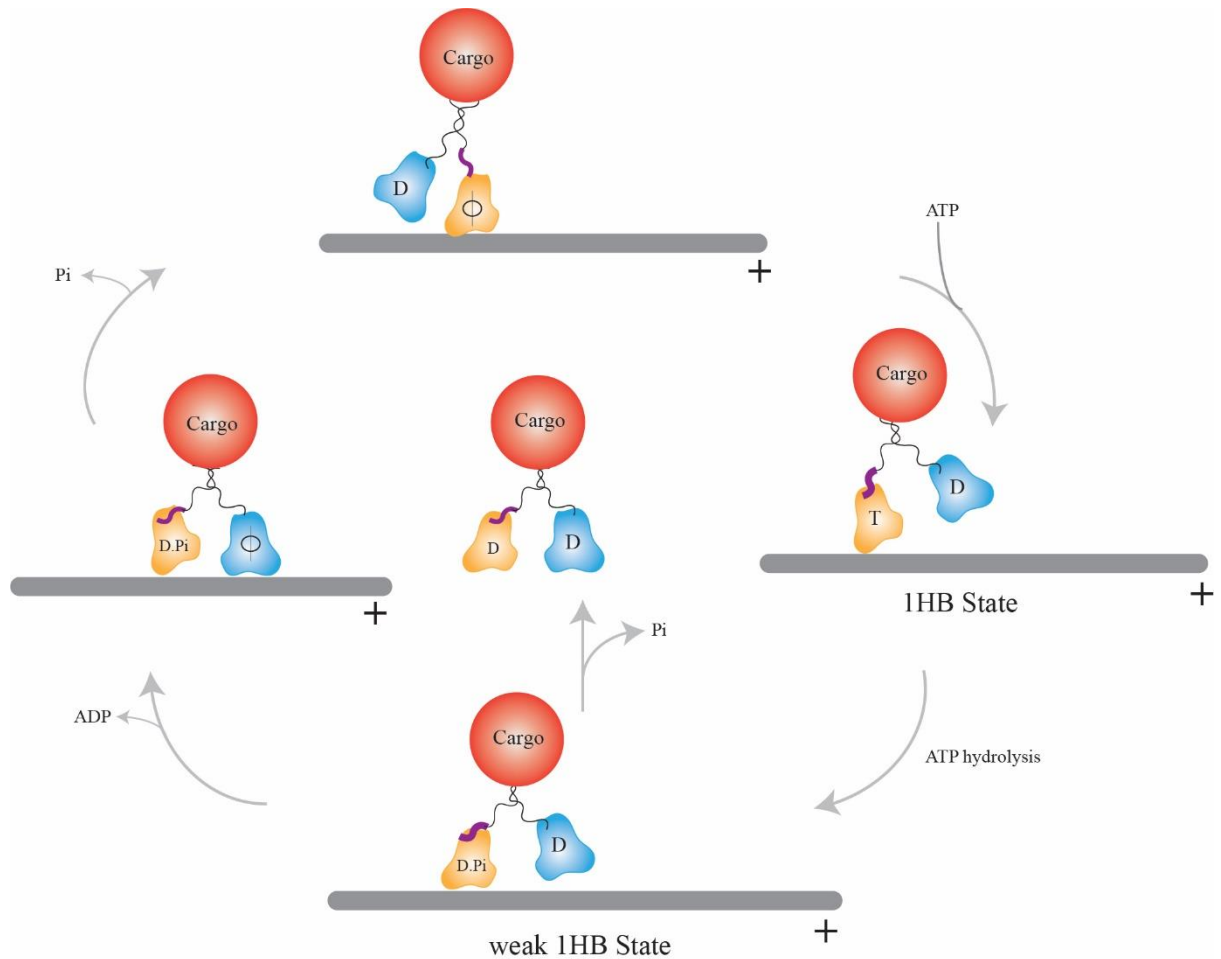


**Figure 3. Mechanochemical cycle of Kinesin motion.** A nucleotide free (apo state) kinesin head makes initial contact with the MT lattice with its neck linker (purple) positioned rearward (top). ATP binding to this head (bound head) leads to partial neck linker docking onto the motor head, pulling the ADP bound tethered head (in blue) forward. Upon ATP hydrolysis, the neck-linker docks completely pushing the tethered head closer to the next tubulin binding site. At this weak one head bound state, the motor can detach if phosphate is released from the bound rear head faster than tether head binding. Tethered head binding to MT releases ADP and leads to a stabler conformation. Having successfully moved to the next binding site, phosphate release from the trailing head returns the motor to its initial conformation, with this head now becoming the trailing tethered head of the next cycle.

During the motion cycle, a nucleotide-free motor head (apo-state) initially contacts the MT lattice with the other head trailing behind in an ADP bound state (tethered head). ATP binding to the bound head triggers two important changes- firstly, ATP binding leads to partial docking of neck linker against the central beta sheet of the bound motor head (Hancock and Howard, 1999; Milic et al., 2014; Rosenfeld et al., 2001). This throws the tethered head forward towards the plus end (Yildiz et al., 2004). Secondly, ATP hydrolysis results in full docking of the neck linker, forming a cover bundle with the motor head, that pushes the tethered head closer to the next tubulin binding site, 8nm away (Andreasson et al., 2015; Khalil et al., 2008; Rice et al., 1999, 2003; Tomishige et al., 2006). This results in formation of a critical weak one head bound state (1HB), where the probability of motor detachment is highest. Initial feeble tethered head contact with the MT immediately releases the bound ADP, generating a strongly attached forward head. On phosphate release, the rear head, in its ADP bound form detaches from the MT, completing the cycle. The kinetic race at the vulnerable 1HB state, between phosphate release and tethered head binding determines how many cycles of motion the motor can complete. If phosphate release from the rear bound head precedes tethered head attachment, then the motor will completely disengage from the MT (Andreasson et al., 2015; Mickolajczyk and Hancock, 2017; Milic et al., 2014). Processivity, the ability to move continuously after a single landing event, is an important element of motor movement and is a defining feature of kinesins, in particular for those involved in long range transport in neurons where cargoes typically move five to ten-fold longer distances (Hirokawa et al., 2010; Vale, 2003). The largest group of kinesins involved in neuronal transport, optimised by a processivity almost five-fold higher than conventional kinesins, is the kinesin-3 family (Lo et al., 2011).

### **Distinctive properties of Kinesin-3**

First identified in *C.elegans* as Unc-104, the disruption of which leads to neuronal dysfunction and consequent movement failure of the organism (Hall and Hedgecock, 1991), Kinesin-3s constitute one of the largest families of molecular motors, with five different subgroups, KIFF1, KIF13, KIF16, KIF28, in mammalian cells (Lawrence et al., 2004). A diverse set of cargo compartments including synaptic vesicles, dense core vesicles, recycling endosomes is transported in anterograde fashion by the kinesin-3 family (Hirokawa et al., 2010). This class of motors functionally differs distinctly from conventional kinesins by a) a rapid speed, 2-fold higher than kinesin-1 (Sekine et al., 1994), b) a substantially higher processivity, termed super-processivity, (~9  $\mu\text{m}$  for KIF16B compared to ~1 $\mu\text{m}$  for kinesin-1, KIF5B) (Soppina et al., 2014) and c) a markedly lower capacity to withstand opposing forces (Okada et al., 2003). The

ability to travel for much longer distances while maintaining a fast velocity appears particularly puzzling, since increased contact with the MT lattice to enhance processivity would incur a significant cost against rapid motor stepping. What property of motor might allow it to undergo uninterrupted cycles of fast motion without detaching from the MT?

### **Determinants of Kinesin-3 processivity**

Mechanochemical cycle of kinesin motion described above necessitates that kinesins function as dimers for processive unidirectional movement. Despite this, the oligomeric status of kinesin-3 family of motors remains controversial. In particular KIF1A, a kinesin-3 involved in anterograde neuronal transport of Rab3a vesicles, and Unc-104, the founding member of this family have both been reported to exist as monomer (Al-Bassam et al., 2003; Sekine et al., 1994). Surprisingly, monomeric KIF1A has even been reported to undergo processive movement in vitro, albeit at a far reduced velocity (0.2  $\mu\text{m/sec}$  compared to 1.5  $\mu\text{m/sec}$  in vivo) (Okada and Hirokawa, 1999). Processive movement of a monomeric motor directly contradicts the “hand-over-hand” mechanism of kinesin stepping described earlier (Yildiz et al., 2004). Motion of the monomeric motor is postulated to occur by a biased diffusion mechanism, whereby the weakly bound motor head undergoes one-dimensional bidirectional diffusive motion with a preference towards the plus end (Okada and Hirokawa, 2000). Whether in vivo, monomeric kinesin-3 exists remains controversial with growing evidence indicating that in vivo, members of kinesin-3 family either likely exists as stable dimers or undergo a monomer to dimer transition for cargo transport (Hammond et al., 2009; Soppina et al., 2014). This is strengthened by the observation that on cargo surfaces, monomeric Unc-104 can undergo transition into a dimeric form, likely due to motor clustering (Klopfenstein et al., 2002). Although limited in their velocity and processivity, monomeric KIF1A can work as efficient teams to generate membrane tubules from GUVs (Giant Unilamellar Vesicles), suggesting teams of monomeric motor can withstand substantial mechanical load (Oriola et al., 2015).

Nonetheless, movement of monomeric kinesins do offer us a clue to what determines its unusually high processivity. The weak binding of monomeric KIF1A is stabilised by interaction between positively charged lysine rich segment of loop 12 of the motor domain, termed the K-loop, with the exposed, negatively charged tails of tubulin (Kikkawa et al., 2000). The K-loop appears to have evolved specifically in this family of kinesins and is therefore a prime candidate for determining family specific motility properties-velocity and processivity (Okada et al., 2003). Although clearly important for movement of monomeric motors (deletion

or replacement of lysins leads to complete abrogation of MT binding), dimeric motors of kinesin-3 family, including KIF1A, are still capable of processive movement even without it (Soppina and Verhey, 2014). The only major contribution of these K-loops, appear to be in increasing the rate at which kinesins attach to the MT, termed the landing rate, suggesting that although there is clearly some affinity offered by the K-loop it is unlikely to be a major determinant of processivity.

Comparing structures of kinesin-1 and kinesin-3 provides a vital hint to the source of increased processivity. Three major residues specifically in kinesin-3 motor domain, R167 in loop 8, K266 in loop 11 and R367 in alpha six helix, mediates direct contact with the MT lattice (Scarabelli, 2015). Importantly, mutating either of these residues to uncharged versions, results in a sharply decreased processivity, similar to kinesin-1 (Scarabelli, 2015).

Processivity of dimeric motors is determined by inter head strain between motors, regulated primarily by the neck linker region (Yildiz et al., 2008). Consequently, increasing neck-linker length by addition of a single amino acid to this region leads to a 3-fold decrease in Kinesin-1 processivity (Shastry and Hancock, 2010, 2011). Shorter neck-linker region of KIF13B has been postulated to lead to an increased inter-head tension, leading to faster stepping rate and tenacious attachment to MTs (Ren et al., 2018). Evidence from structural studies suggest that shorter neck-linker makes fewer hydrogen bonds while docking onto the motor head during the power stroke, resulting in faster undocking and rapid speeds. How does this affect the kinetic cycle and processivity of the motor? Biochemical studies strongly indicate that kinesin-3 motion is rate-limited by attachment of the tethered head to the onward binding site on the MT lattice, despite ADP-bound heads having a ~15-fold higher affinity than kinesin-1 for MTs (Soppina and Verhey, 2014; Zaniewski et al., 2020). This perhaps reflects a decreased kinetics of neck-linker docking of the bound head which positions the tethered head. Kinesin-3s spend most of their motion cycle in a vulnerable one-head bound state post ATP hydrolysis, where competition between bound rear head detachment and forward tethered head attachment determines overall motor off rate and thus processivity (Hancock and Howard, 1999; Zaniewski et al., 2020). This one head-bound state is surprisingly durable for Kinesin-3, suggesting additional electrostatic interactions with the MT lattice (Zaniewski et al., 2020). This leads to a higher probability of the kinesin exiting this vulnerable stage successfully towards a more stable two-head bound state. However, one cost of this durable one-head bound state is the kinesins fragility against opposing forces resulting in significantly higher chances of motor detachment under opposing load (Arpağ et al., 2019; Arpag et al., 2014).

## Mechanism of auto-inhibition

Even in the absence of MT binding, kinesins contain residual ATPase activity. Without cargo binding, this can result in futile cycles of precious ATP consumption. Thus, in the absence of cargo transport, kinesins must be held in an inactive state. Presently two contending models of catalytic inhibition explain how such a feat is achieved in cells (Figure 4B). Both models operate under the assumption that recruitment of the kinesin to its cargo results in MT binding and active transport. However, this does not exclude the possibility that cargo recruited kinesins may yet be inactive or un-engaged in vivo and this remains an unexplored question.

The first model of kinesin auto-inhibition is specific to kinesin-3 family, due to its unique ability undergo oligomeric transitions. The monomer-dimer model posits that monomeric kinesins are held in a cytosolic, inactive state that becomes dimeric upon cargo recruitment, possibly due to enhanced local concentration (Al-Bassam et al., 2003; Klopfenstein et al., 2002; Rashid et al., 2005; Soppina et al., 2014; Tomishige et al., 2002). The transition is chiefly mediated by an intramolecular rection between the neck coil and the first coiled coil region following it that holds the kinesin in an inactive monomeric state but forms intermolecular interaction when present at high concentrations. This switch between intra to intermolecular reaction has been observed for members of KIF1 and KIF13 subgroups. For KIF13 in particular, the NC and CC1 is separated by a proline induced kink, allowing CC1 segment to fold back onto the NC (Soppina et al., 2014). KIF1A also executes a similar fold between NC and CC1, with L478, M481 and V483 constituting key residues of the intervening flexible linker, instead of a single prominent proline residue (Huo et al., 2012). Member of the KIF1 family, Unc104 shares features of this monomer-dimer transition, though the switching coiled-coil pair forms entirely within two helices of the neck region (Al-Bassam et al., 2003).The second mode of auto-inhibition invokes the tail region, intruding onto the motor head and abolishing its ATPase activity, in the dimeric state of the motor (Coy et al., 1999b). The tail is released from this inhibitory position by binding to its cognate cargo (Friedman and Vale, 1999). This general mechanism of kinesin inhibition, first proposed for conventional kinesin-1, operates in select members of the kinesin-3 family, KIF13B (also known as GAKIN), KIF16B and KIF1C. Full-length KIF13B, a stable dimer, exhibits poor MT activated ATPase activity and reduced velocity as compared to a truncated construct lacking the terminal C-terminal region but containing the NC, CC1 and FHA domain suggesting that the C-terminal region inhibits kinesin activity (Yamada et al., 2007). This inhibition is relieved by binding of its cargo, hDlg (Human Discs Large), to the C-terminal stalk region (Yamada et al., 2007).

Additionally, the KIF13B motor-tail interaction is also shown to be sensitive to phosphorylation (Yoshimura et al., 2010). A similar mechanism has been proposed for KIF1C where both the FHA domain and the following CC3 docks onto the alpha four helix of the motor domain in the dimeric inactive state and is undocked by binding of the protein tyrosine phosphatase N21 (PTPN21) to the CC3 (Siddiqui et al., 2019).

### **Cargo specificity of Kinesin-3**

Members of the kinesin-3 superfamily is characterised by presence of a lipid binding domain at its C-terminal (Fig 4A) (Siddiqui and Straube, 2017). This includes a Pleckstrin homology (PH) domain present in KIF1A and KIF1B that binds PI(4,5)P<sub>2</sub>. Similarly, KIF16B is characterised by a PX (Phox homology) domain that interacts directly with PI(3,4,5)P<sub>3</sub>, present on early endosome membranes in vivo (Blatner et al., 2007; Hoepfner et al., 2005). Surprisingly, KIF1C does not contain any discernible lipid-binding domain, instead featuring a C-terminal proline rich region that mediates its interaction with Rab6 GTPase (Lee et al., 2015b). In fact, Rab6 additionally contacts KIF1C at its motor domain inhibiting its MT binding. Further, the stalk domain of KIF1C interacts with non-muscle Myosin II (Kopp et al., 2006).

C-terminal of KIF13B contains a CAP-Gly domain that can directly bind C-terminal tail of MTs. In addition, kinesin-3 specific FHA domain of KIF13B binds Centaurin-alpha1 that directly interacts with PI(4,5)P<sub>2</sub> and PI(3,4,5)P<sub>3</sub> (Tong et al., 2010; Venkateswarlu et al., 2005).

Apart from direct interaction with membrane lipids, kinesins are often recruited to its cognate cargo by intermediary adaptor proteins. These adaptor proteins include Bicaudal (BICD), BICD-related protein 1 (BICDR1) and Hook3 (Bielska et al., 2014; Schlager et al., 2010). Along with kinesin recruitment, these proteins also mediate interaction of the cargo with minus-end directed Dynein complex, thus setting up a race between opposite polarity motors.

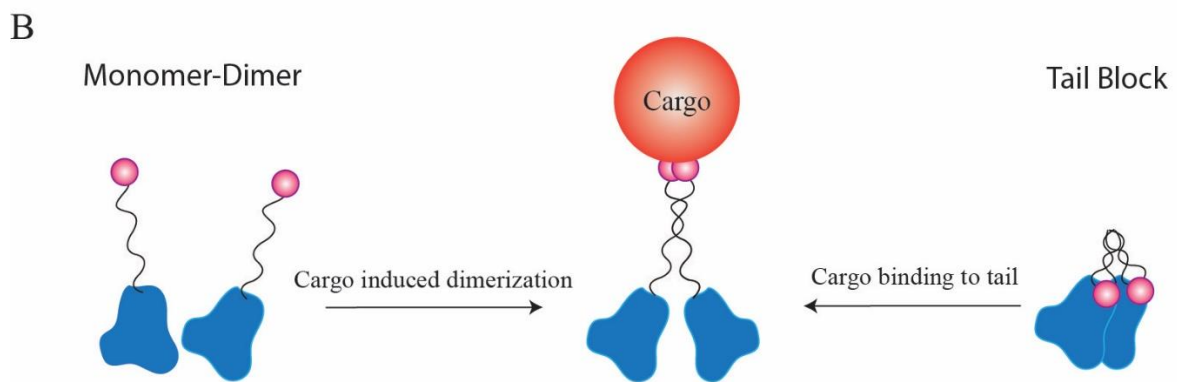
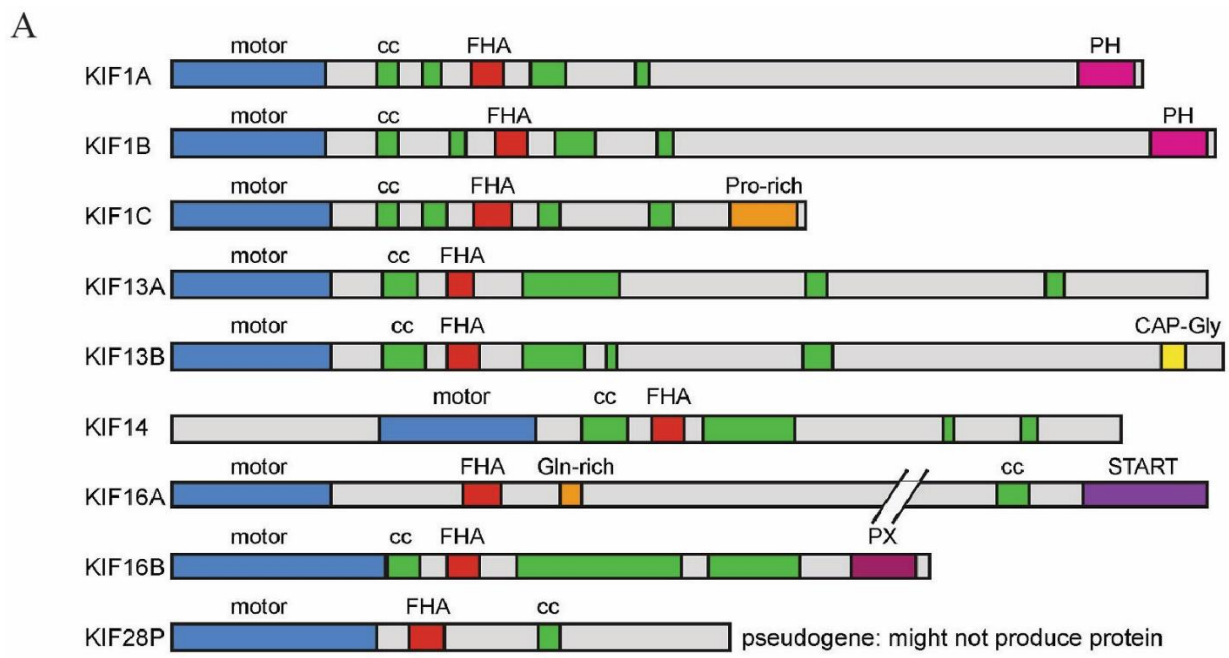


**Figure 4. Cargo binding of kinesin-3 family.** A) All five subfamilies of kinesin-3 motors (KIF1, KIF13, KIF14, KIF16, KIF28) share a similar domain organisation, characterised by an FHA domain in the stalk and several short coiled-coil (CC in green) segments in the tail. (Adapted from Siddiqui and Straube, 2017) B) Activation mechanism of kinesin-3. Monomer-dimer transition model, kinesin is held in an extended but monomeric state that becomes dimeric on cargo surface, likely due to increased concentration. In the alternatively tail-block model, kinesin is locked in a folded conformation with the tail region blocking motor activity. This inhibition is lifted by cargo binding and formation on inter-dimer coiled coils.

### **Track specificity of Kinesin-3**

From a motor perspective, not all MT tracks are equivalent in terms of permitting motility. Although kinesin binds at the inter-dimer interface of tubulin, conserved in all MTs, binding is modulated by presence of C-terminal tail modifications of tubulin (Janke, 2014; Verhey and Gaertig, 2007). Alternative tubulin isoforms and myriad PTMs present on tubulin subunits has led to the provocative proposal of motor transport being governed by specific identity of the tubulin subunit (tubulin code) (Sirajuddin et al., 2014). Indeed, polyglutamylation of  $\alpha$ -tubulin tails is predicted to increase its affinity for K-loop. In vitro, KIF1A motion on polyglutamated taxol-stabilised MTs has been shown to involve a period of pausing between continuous runs, increasing the overall processivity (Lessard et al., 2019). Interaction of the K-loop with polyglutamated tubulin tail positively modulates the frequency of such pausing events as deletion of charged residues sharply reduces both the frequency and duration pausing (Lessard et al., 2019). Mice devoid of tubulin polyglutamylation, exhibit severe disruption of kinesin-3 mediated delivery of synaptic vesicles to axon terminals (Ikegami et al., 2007). Together this suggests, that polyglutamylation positively regulates kinesin-3 transport. In contrast, tubulin acetylation has been reported to inhibit KIF1C movement (Bhuwania et al., 2014).

Similarly selective MAP binding to different MTs, has led to similar proposals of motor transport being governed by presence of specific combination of MAPs (MAP code). Tau, the principal MAP responsible for various neurodegenerative disorders, inhibits movement of both kinesin-1 and kinesin-3 (Dixit et al., 2008; Kellogg et al., 2018; Shigematsu et al., 2018). MAP7, which localises to both axon and dendrites like MAP9, inhibits KIF1A movement, though positively modulating kinesin-1 movement (Chaudhary et al., 2019; Hooikaas et al., 2019).

In contrast, dendrite associated MAP, Doublecortin (DCX), directly binds the motor domain of kinesin-3, KIF1A, increasing its interaction with the MT lattice and KIF1A velocity (Lipka et al., 2016). Similarly, MAP9, localised to both axons and dendrites, stimulates KIF1A landing on MTs, potentially by interacting with its K-loop (Monroy et al., 2020). However, in presence of inhibitory MAP7, KIF1A movement was significantly reduced even in the presence of stimulating MAP9 (Monroy et al., 2020). Though inhibitory action of MAP7 on KIF1A can't be compensated by other positively regulating MAPs, this is not the case for kinesin-1. In fact, MAP7 can overcome the inhibitory action of Tau filaments to facilitate kinesin-1 movement (Monroy et al., 2018).



# **Assembly and function of the Central spindle**

During cell division, proper chromosome segregation requires ordered assembly of the mitotic spindle, a bipolar, fusiform shaped specialised MT structure (Flemming 1882; Reber and Hyman, 2015). Sister chromosomes attach to opposing spindle poles by their kinetochore and undergo pole-wards movement in anaphase (Vukušić and Tolić, 2021). Beginning in anaphase, plus ends of MTs from opposing sides bundle and interdigitate between segregating chromosomes to form a specialised MT structure, the central spindle, that directs cytokinesis, vesicular traffic and abscission (Glotzer, 2009). As cells undergo cytokinesis, this antiparallel, bundled structure concentrates into a 2 μm wide densely packed region called the Flemming body (or the midbody) (Mastronarde et al., 1993).

Functionally, the central spindle influences spindle elongation in diverse cell types and acts as a signalling platform for orchestrating cytokinesis (Glotzer, 2009). Cytokinesis involves assembly of an equatorial actomyosin ring, that constricts along with the plasma membrane to separate two daughter cells (Glotzer, 2017; White and Borisy, 1983). Assembly of the ring in mammalian cells is triggered by activation of a small GTPase, RhoA, by a cognate GTPase Activating Protein (GAP)-ECT2 (Su et al., 2011; Tatsumoto et al., 1999; Wagner and Glotzer, 2016). Across evolution, equatorial recruitment and concentration of ECT-2 depends on the presence of a proximal overlapping, bundled antiparallel microtubular structure (Rappaport, 1971). In most cell types, central spindle fulfils this role (in large cells, long astral MTs extending from opposing spindle poles can from antiparallel overlaps near the cortex) (Baruni et al., 2008; Foe and Von Dassow, 2008; Murthy and Wadsworth, 2008; Su et al., 2014; Werner et al., 2007). Additionally, central spindle MTs provide a track for vesicular transport and fusion at the abscission site (Green et al., 2012).

## **Organisation and origins of central spindle MTs**

Compared to metaphase spindle, structural organisation of the central spindle is poorly understood. During metaphase, spindle MTs could be broadly divided into three categories-a) kinetochore fibres (K-fibres), parallel MTs with their plus ends captured at the kinetochore of chromosomes b) astral MTs, that emanate from the spindle poles towards the cell cortex and c) interpolar MTs with their plus ends forming antiparallel crosslinks at the equatorial zone (Kapoor, 2017). K-fibres, which constitute ~20% of the metaphase spindle mass, could be directly coupled to interpolar MTs (Yu et al., 2019). The subset of interpolar MTs directly

coupled to k-fibres, termed bridging fibres, form long antiparallel overlaps to keep sister kinetochores apart and recruit known markers of the central spindle (Kajtez et al., 2016; Polak et al., 2017; Vukušić et al., 2017). Given the similarity between bridging fibres in metaphase and central spindle in anaphase, both in terms of MT polarity and molecular composition, it is tempting to speculate that the former structure matures into the later or serves as a template (Vukušić and Tolić, 2021). This is strengthened by two lines of evidence- firstly, cryo-electron tomography (cryo-ET) of human and *C.elegans* anaphase spindle indicate that MT bundles of the central spindle never reach spindle poles, often terminating either near chromosomes or k-fibres (Yu et al., 2019). This is in agreement with previous electron tomogram studies of PtK1 cells, suggesting MT structure of the spindle is well conserved across evolution (Mastronade et al., 1993). Secondly, depletion of Augmin, an octameric protein complex responsible for MT branching, is known to cause a severe reduction in numbers of central spindle MTs and significantly impair number of bridging fibre MTs between sister kinetochores (Goshima et al., 2008; Kamasaki et al., 2013; Manenica et al., 2020; Uehara et al., 2009). Taken together, ultrastructural evidence of close contacts between central spindle MTs and k-fibres and Augmin dependent MT nucleation of both population of MTs strongly suggest that bridging fibres represent a true precursor to central spindle MTs. Despite this, an alternative hypothesis proposing centrosome nucleated interpolar MTs released from the spindle pole during anaphase constitute the main fraction of central spindle MTs can not be completely ruled out (Glotzer, 2009). However, a functional central spindle is shown to form in the absence of either chromosomes or centrosomes in insect spermatocytes (Alsop and Zhang, 2003; Bucciarelli et al., 2003). These findings raise the question: can a central spindle be formed de novo?

Pre-anaphase MT depolymerisation, by nocodazole or cold treatment, and subsequent regrowth studies have been particularly instructive in answering whether a central spindle can form de novo (Canman et al., 2003; Uehara and Goshima, 2010). After complete MT depolymerisation, cells can undergo fresh MT nucleation and form a stable, bipolar, functional central spindle capable of completing cytokinesis (Canman et al., 2003). This de novo central assembly heavily relies on Augmin dependent MT nucleation, accounting for almost 70% of the regrown MTs (Uehara and Goshima, 2010). But Augmin can only act to amplify MT numbers and its branching activity requires pre-existing MT lattices (Hsia et al., 2014). What provides these initial template MTs during regrowth? Careful analysis indicates that HURP (Hepatoma Up-Regulated Protein), a component of the Ran-GTP dependent MT nucleation pathway, plays a crucial role in MT nucleation in such cells (Silljé et al., 2006). In unperturbed anaphase, this

pathway likely acts redundantly with centrosome dependent MT nucleation to generate pre-existing MTs that are subjected to Augmin dependent MT branching and amplification to form a dense, bipolar central spindle (Uehara and Goshima, 2010). Therefore, although there is no absolute requirement of either functional centrosome or chromosomes alone in central spindle formation, they likely function redundantly to generate pre-existing template MTs during normal mitotic progression.

Additionally, central spindle MTs appear to be unfocused in the absence of Asp (Abnormal Spindle Poles), a 220KD MAP first identified in *Drosophila* (Wakefield et al., 2001). As a consequence of disorganised central spindle structure, these cells fail in cytokinesis with particularly dire consequences for larval brain cells (Ito and Goshima, 2015; Wakefield et al., 2001). In vitro, Asp was demonstrated to bundle MT minus ends (Ito and Goshima, 2015; Jiang et al., 2017). Therefore, it is plausible that minus ends of the central spindle MTs, nucleated by Augmin, is further bundled by Asp to create crosslinked parallel arrays that interdigitate at their plus ends with similar parallel arrays from opposing sides forming bipolar, antiparallel overlapping MTs. Additional minus end stabilising MAPs, such as Patronin, might co-operate to protect MT minus ends against depolymerisation (Goshima and Vale, 2003).

### **Stability of Central spindle**

There is general consensus that MTs are stabilised prior to anaphase. Central spindle MTs in particular, have been shown to be extremely stable with 5-fold slower tubulin turnover compared to metaphase MTs in FRAP studies across yeasts and mammalian cells (Higuchi and Uhlmann, 2005; Mallavarapu et al., 1999; Saxton and McIntosh, 1987). However, in *Drosophila* embryos, both metaphase spindle and equatorial MTs of the central spindle exhibit rapid tubulin turnover with a half-life of around 3 sec, with only centrosome proximal MTs showing significant change in turnover fraction (Cheerambathur et al., 2007). This discrepancy could be explained, at least partially, by the particularly rapid pace of embryonic divisions. The idea of increased MT stability is supported by the fact that mild dose of MT depolymerisation agents, sufficient to destroy MT asters, doesn't abrogate central spindle structure (Murthy and Wadsworth, 2008). Though stable, EB1 (End-Binding protein 1) comets specifically highlighting growing dynamic MT plus ends, have been shown to localise to the central spindle (Cheerambathur et al., 2007; Rogers et al., 2002). However, the speed of MT polymerisation, measured by EB1 comet speed, dampens considerably during late anaphase, indicating a transition to slower MT growth period (Asthana et al., 2021).

## **Molecular determinants of central spindle**

Central spindle is characterised by formation of antiparallel crosslinks between parallel bundles of MTs emanating from opposing sides between segregating chromosomes. Both motors and non-motor MAPs combine to form the central spindle. Their functions range from controlling MT dynamics (CLASP, EB1), force generation (MKLP1, MKLP2) to forming antiparallel overlaps (PRC1). PRC1, tasked with forming stable antiparallel overlaps as well as recruiting diverse set of motors and MAPs, is recognised as the principal organiser of the central spindle (Glotzer, 2005). Herein, I review the roles played by PRC1 and its associated partners, CLASP, KIF4A, Centralspindlin complex in central spindle formation.

### **Overview of PRC1 family of MAPs**

First identified in BY-2 cell extract as a 65kDa microtubule associated protein (MAP) capable of crosslinking MTs, MAP-65 family of proteins has since been found to exist as conserved, dimeric MT bundler in all higher eukaryotes (Chang-Jie and Sonobe, 1993). Its role as a conserved mitotic spindle organiser, responsible for bundling spindle structures during anaphase was first uncovered through a genetic analysis in its budding yeast orthologue, Abnormal Spindle Elongation-1, Ase1 (Pellman et al., 1995). Ase1 is critical to the formation of a crosslinked antiparallel bundle of MTs- the central spindle, a structure responsible for the positioning and execution of cytokinesis (Schuyler et al., 2003). Subsequently, the Ase1 orthologue in mammalian cells was found in a screen for Proteins Responsible for Cytokinesis-PRC1 (Jiang et al., 1998).

With at least one orthologue present in all eukaryotes examined, from Ase1p in Fission yeast, Feo in *Drosophila*, SPD-1 in *C.elegans*, to the nine isoforms of MAP-65 (MAP65-1 to MAP65-9) in plants, PRC1 constitutes a large, conserved family of MAPs important for MT bundling, central spindle organisation, cytokinesis and abscission (Gaillard et al., 2008; Pellman et al., 1995; Verbrugghe and White, 2004; Verni et al., 2004). Although, the mechanism of action, primarily MT bundling, is similar among the various members of the family, significant differences exist in their overall functionality.

### **Domain organisation of PRC1**

All members of the Ase1/MAP65/PRC1 family contain a N-terminal dimerization domain (1-66), a rod domain (67-345), a central spectrin domain (346-467) and an unstructured C-terminal tail (467-620) (Fig 2A) (Mollinari et al., 2002; Subramanian et al., 2010; Zhu et al., 2006). The

N-terminal predominantly alpha-helical region, comprising of the dimerization and the rod domain, localises weakly to the spindle midzone even in the absence of notable MT binding (Molinari et al., 2002). The central spectrin domain and the C-terminal unstructured Lys/Arg rich region is sufficient to bind MTs (Subramanian et al., 2010). A recent 4Å cryo-EM structure of this truncated region bound to MT offers important insights into MT binding and bundling activity of PRC1 (Kellogg et al., 2016). In agreement with previous crystal structures, a three-helix bundle (H7, H8, H9) within the central spectrin domain makes multiple contacts with the inter-tubulin dimer interface of MTs, with the rest of the spectrin domain protruding at a 70° angle from the MT surface towards the minus end (Kellogg et al., 2016; Subramanian et al., 2013). This binding is further strengthened by the interaction of the unstructured C-terminal tail of PRC1 with the acidic C-terminal tail of neighbouring proto-filaments (Kellogg et al., 2016). Surprisingly, the same inter-dimer tubulin surface is also involved in binding of motor proteins- kinesin and dynein, setting up a fascinating competition between MAP and motor occupancy on the MT lattice.

### **Localisation and Mitotic Functions of PRC1**

Although nuclear in interphase, PRC1 localises to the mitotic spindle in metaphase, becoming progressively enriched at the equatorial region of MT overlaps as cells undergo anaphase and finally constrained to a short, bright foci in the post anaphase midbody (Molinari et al., 2002). Nuclear localisation is likely mediated by a canonical Nuclear Localisation Signal (NLS) at the junction of the spectrin and C-terminal region.

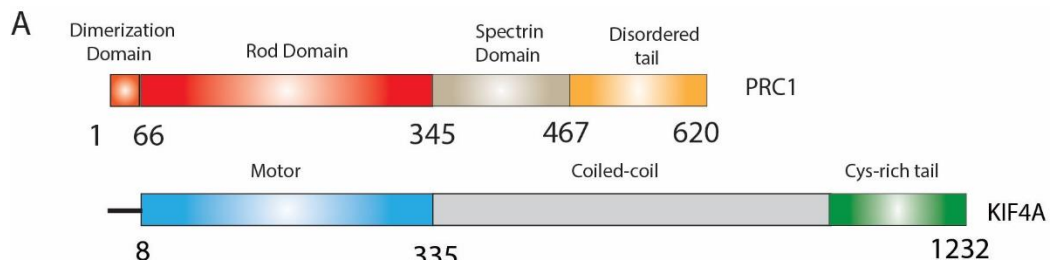
The exact role of PRC1 in metaphase has remained elusive for a long time, in part due to absence of any significant defect of the metaphase spindle upon PRC1 knockdown in mammalian cells. Recent discovery of a specialised subset of overlapping MTs between sister kinetochore fibres, termed bridging fibres, in metaphase has significantly furthered our understanding of PRC1's role in metaphase (Kajtez et al., 2016; Polak et al., 2017). Acute removal of PRC1 from the metaphase spindle, using optogenetic tools, leads to significant reduction of number of bridging fibre MTs (Jagrić et al., 2021). Thinning of these fibres, as a consequence of MT loss, results in chromosome misalignment at the metaphase plate, reduction in inter-kinetochore distance and frequent occurrence of lagging chromosomes (Jagrić et al., 2021).

Upon siRNA mediated knockdown of PRC1, cells undergo unperturbed mitosis till mid-anaphase, wherein the absence of banded equatorial MT overlaps leads to complete

disengagement of spindle halves (Molinari et al., 2002). Absence of an organised spindle midzone results in furrow regression and consequent cytokinesis failure. Across evolution, from yeasts to humans, the distinct lack of antiparallel MT bundling and central spindle organisation upon loss of PRC1 family members is remarkably well-conserved (Jiang et al., 1998; Loiodice et al., 2005; Verbrugge and White, 2004). In addition, upon deletion of Ase1 in fission yeast, which lacks any canonical NLS, longitudinal MT bundles do not form in interphase, suggesting a role of Ase1 beyond spindle organisation (Janson et al., 2007; Loiodice et al., 2005).

### Molecular mechanism of PRC1 action

Consistent across divergent members of PRC1 family is its ability to selectively crosslink plus ends of antiparallel MTs at the spindle midzone. Although monomeric PRC1 constructs, lacking the N-terminal dimerization domain, can bind MTs with an average lifetime of ~3sec and undergo one-dimensional diffusive motion, it can't bundle MTs (Forth et al., 2014). Bundling of MTs require dimerization. Full-length PRC1 exists as stable homodimers in solution and dimerization increases the average lifetime of full-length PRC1 to ~ 7sec on single, stable MTs (Subramanian et al., 2010; Zhu et al., 2006). Similarly, fission yeast PRC1 orthologue- Ase1p, also binds MTs as stable dimers capable of one-dimensional diffusion on the MT surface with an average lifetime of ~11sec, suggesting a conserved mode of MT binding (Loiodice et al., 2005). Remarkably, whereas in sub nanomolar concentrations, on single MTs, Ase1p exists as dimers, on crosslinked MTs Ase1p is found to form higher order oligomers (Kapitein et al., 2008). Although PRC1 has not yet been shown to form such higher order oligomers, MT binding of PRC1 does show significant cooperativity, indicating multimerization could indeed be a conserved mode of MT binding for Ase1/PRC1/MAP65 family (Subramanian et al., 2010). Electron tomography suggests that bundled antiparallel MTs are held 35nm apart when crosslinked by PRC1 (Subramanian et al., 2010). This is consistent with an elongated length of 31.7nm of dimeric PRC1 (Kellogg et al., 2016; Subramanian et al., 2013). Selective binding to antiparallel overlaps is a defining feature of this family of MAPs, although the extent of this selectivity might differ amongst its members. In vitro, fission yeast Ase1p forms antiparallel MT overlaps with a probability of 75%, while the same for PRC1 is close to 90% (Janson et al., 2007; Subramanian et al., 2010).



**B**

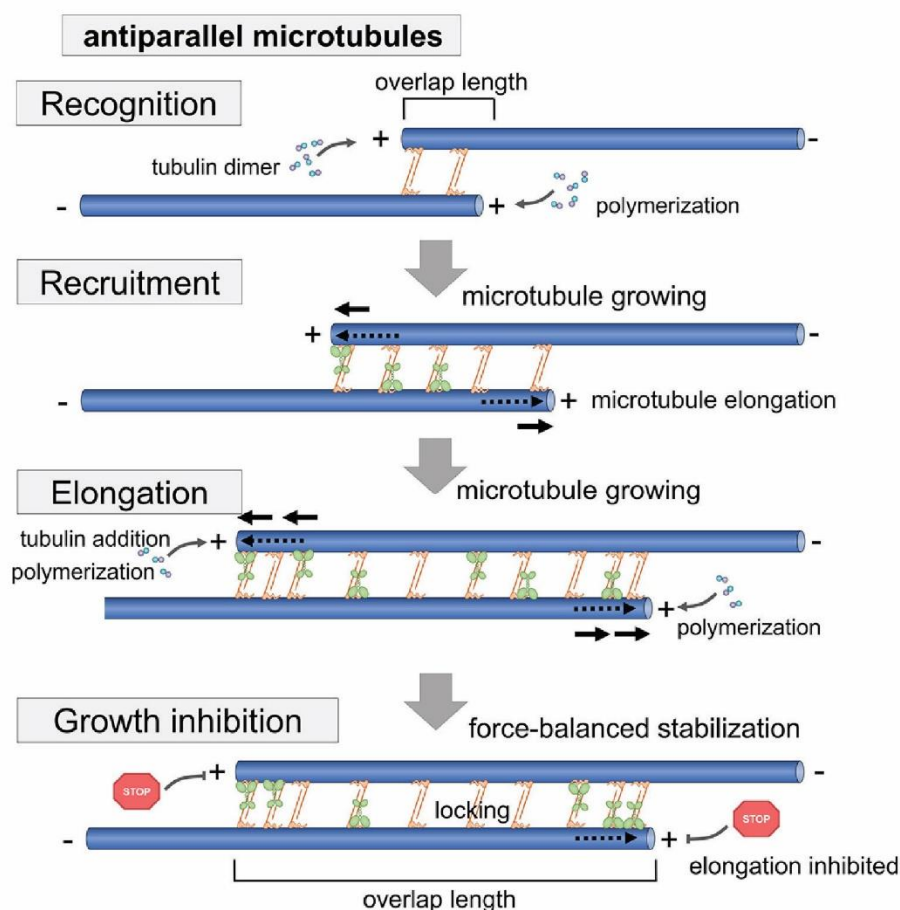


**Figure 5: Molecular mechanisms of PRC1 action. A)** Domain structure of full-length PRC1 and KIF4A. The N-terminal dimerization domain (1-66) and rod domain (67-345) is required for its interaction with the C-terminal coiled coil and tail regions of KIF4A. The Spectrin and C-terminal region of PRC1 binds MTs. **B)** PRC1 (in orange) and KIF4A (in green) forms a two-component system to control overlap length of antiparallel MTs. Dimeric PRC1 alone recognises antiparallel overlaps followed by recruitment of KIF4A (in green). Competition between MT elongation by tubulin addition and speed of KIF4A binding to the plus end determines final overlap length. Figure adapted from (She et al., 2019). See text for details.

The Xenopus orthologue of PRC1, almost exclusively forms antiparallel crosslinks (Bieling et al., 2010). Therefore, although all members majorly form antiparallel overlaps, the selectivity appears to be less stringent for Ase1p.

How does PRC1 specifically recognise antiparallel contacts? This is particularly surprising given the simple arrangement of PRC1 and its molecular flexibility (Subramanian et al., 2010). Molecular simulations indicate that such specificity is a result of the relative orientation of the two spectrin domains of the dimer. When bound to a single MT, PRC1 dimers can undergo significant rotational flexibility, however, the relative orientation of the spectrin domain predominantly prefers a second MT to be in antiparallel configuration to the first (Kellogg et al., 2016). This bias in antiparallel conformation is strengthened by binding of multiple PRC1 molecules, steering and aligning the two MTs in stable antiparallel arrangement (Kellogg et al., 2016).

Given multiple PRC1 molecules strongly interact with an antiparallel MT pair and late anaphase central spindle is composed of both active motors and MAPs such as PRC1, how does PRC1-MT contacts respond to motor generated forces? A particularly compelling idea is PRC1 acts as a molecular brake, offering a resistive force against motor driven sliding forces. This would explain why upon loss of PRC1 or its orthologues, the spindle halves separate completely (Gaillard et al., 2008). In vitro, Ase1p can dynamically resist sliding forces generated by Kinesin-14 (Braun et al., 2011). As MT pairs slide apart, Ase1p, due to its low off-rate, concentrates in the shrinking overlap offering increasing resistance and eventually halting motor driven sliding. Recently, PRC1 was also found to offer similar resistive action to external pulling forces using novel force measuring assays (Gaska et al., 2020). To accurately measure resistive forces one end of a PRC1 crosslinked MT pair was attached to an optical trap while the other surface attached MT was carefully pulled away at a defined velocity by a piezo controlled stage (Gaska et al., 2020). As the overlaps shortened, PRC1 provided measurable piconewton range resistive forces, that depended solely on the number of PRC1 molecules in the overlap and scaled with the velocity of bundle separation (Gaska et al., 2020). Unexpectedly, when two pulling events were interrupted by a short pause, PRC1 molecules offered substantially more resistance, indicating molecular rearrangement within a shrinking overlap can lead to higher resistive forces (Gaska et al., 2020). Further studies are needed to address the possible nature of such rearrangements, including formation of higher order oligomers, akin to Ase1p.

Although, both Ase1p and PRC1 can offer substantial resistive forces to MT sliding, there are significant differences in their response to bundle separation. During MT sliding in vitro, force generated by PRC1 remain relatively stable even as the density of PRC1 in the shrinking overlap increase gradually (Gaska et al., 2020). In similar conditions however, Ase1p offers increasing resistive forces, that scale with increasing Ase1p density within the shortening overlap (Braun et al., 2011; Lansky et al., 2015). This “gas spring” like behaviour of Ase1p, where compressed Ase1p molecules apply an expansive force (entropic expansion) against overlap shortening is notably absent in PRC1 (Lansky et al., 2015).

If PRC1-MT contacts are consistently under strain due to motor action, how stable is PRC1 itself at the central spindle? FRAP studies at the central spindle suggest a relatively slow turnover of Ase1p at the central spindle ( $t_{1/2} \sim 7\text{min}$ ). This contrasts with single MTs, where Ase1p shows a faster recovery time of around  $\sim 35\text{sec}$ . Therefore, Ase1p binds stably at the central spindle. This stable binding appears to be a conserved element of Ase1/PRC1 family. Similar to Ase1p, endogenous PRC1 exhibits progressively slower recovery times, from 6s in metaphase to 44s in late anaphase (Asthana et al., 2021). This progressively stabler interaction of PRC1 has been hypothesised to reflect a myriad of post-translational modifications at the beginning of anaphase (She et al., 2019)

### **PRC1 as a major protein interaction hub for central spindle assembly**

PRC1 acts as the principal organiser of the densely packed, interdigitating MTs of central spindle, that simultaneously act as a mechanical element as well as a regulatory platform for cytokinesis, vesicle trafficking and abscission (Glotzer, 2009). At the core of this organisation, is the ability of PRC1 to engage multiple proteins, both motor and MAPs, to regulate MT network. These proteins can be broadly divided, by their functionality, into distinct nodes that serve critical functions- a) MAPs controlling MT dynamics (CLASP1), b) MAPs regulating overlap length (KIF4A), c) Motors for mechanical stability (Centralspindlin complex).

#### **a) MAPs controlling MT dynamics**

In fission yeast, the central region CLASP1 orthologue, Cls1p, interacts physically with the N-terminal of Ase1p (Rincon et al., 2017). Like its mammalian orthologue, Cls1p promotes MT rescue (Bratman and Chang, 2007). Association with Ase1p recruits Cls1p to MT bundles in interphase and to spindle midzone in mitosis, where it acts to prevent premature MT depolymerisation. This interaction is pivotal for the assembly of bipolar spindles in the absence of Kinesin-5 action, demonstrating how the force of MT polymerisation and bundling can be

harnessed to compensate for loss of motor activity (Rincon et al., 2017). In mammalian cells, the C-terminal of PRC1 directly binds and recruits CLASP1 to the central spindle in late anaphase B (Liu et al., 2009). PRC1-CLASP1 interaction is important for spindle midzone stabilization as disruption of this interaction by membrane permeable peptides leads to rapid reduction of the number of MT bundles at the central spindle (Liu et al., 2009). As mentioned before, during the course of anaphase, PRC1 becomes more stably bound to midzone MTs with progressively slower turnover rates (Asthana et al., 2021). However, CLASP1, though recruited by PRC1 to the central spindle, does not follow this trend and remain dynamic throughout anaphase and telophase with a turnover rate of 1.3 to 2.9 sec (Asthana et al., 2021). Therefore, although CLASP1 is recruited to the central spindle by PRC1, this interaction appears to be weak. Although CLASP1's role in stabilising MTs at the central spindle is undisputed, the exact mechanism of CLASP1's effect on MTs remains enigmatic, with interaction with other MAPs such as CLIP-170 and EB1 proposed to at least in part be responsible for CLASP1 action (Al-Bassam et al., 2010). EB1 is also present at the central spindle in late anaphase, and overlaps significantly with PRC1, though a direct interaction between the two is not yet reported (Asthana et al., 2021).

### b) MAPs regulating overlap length

The N-terminal of PRC1 is also involved in recruiting KIF4A, a kinesin involved in chromosome compaction and segregation, to the central spindle (Mazumdar et al., 2004; Sekine et al., 1994). The C-terminal half of this motor, consisting of both the stalk and the tail region, directly binds PRC1 (Kurasawa et al., 2004; Subramanian et al., 2013). Upon loss of KIF4A, MTs fail to form a rigidly bundled central spindle structure. Consequently, PRC1 and other central spindle markers fail to localise to the spindle midzone (Kurasawa et al., 2004). Apart from a direct structural role of KIF4A motor in organising central spindle, mislocalisation of PRC1 raises the interesting possibility of it being carried to the MT plus end by KIF4A motor action (Zhu and Jiang, 2005). In support of this, PRC1 localisation and central spindle organisation is restored by expression of full-length KIF4A in these cells but not a motor-dead mutant, suggesting that KIF4A motor activity is essential for correct PRC1 localisation (Zhu and Jiang, 2005). Direct evidence of a motor, KIF4A, carrying a MAP, PRC1 to plus ends of MTs, where it acts to cross-link antiparallel MTs comes from elegant in vitro studies by Subramanian et al., 2013 (Fig 2B). On stabilised MTs, PRC1 and KIF4A accumulate strongly at the plus end of single MTs, forming “end-tags” in the absence of MT bundling. Excitingly, the size of such end-tags of PRC1 and KIF4A, scale with the length of MTs. Concentration of

PRC1-KIF4A complex at MT plus ends has been proposed to occur by a “traffic jam” mechanism, whereby high-affinity complex of KIF4A and PRC1 arrives at the plus-end and dissociates slowly. Persistent traffic across the MT initially leads to a build-up of PRC1-KIF4A complexes at the plus end, forming a protein-tag of growing size that eventually reaches a stable length when dissociation of PRC1-KIF4A complexes from the plus-end balances incoming traffic. Longer MTs with proportionately more binding sites would cause a longer traffic jam of PRC1-KIF4A complexes, assuming that once bound such complexes can travel across the entire length of longer MTs. Although, growing evidence points towards existence of such “end-tag” scaling mechanism *in vivo*, the nature of its function in the context of spindle organisation remains unanswered. In vitro, PRC1-KIF4A complex, in addition to forming end-tags, can also slide antiparallel MTs with the sliding velocity increasing linearly with initial overlap length (Wijeratne and Subramanian, 2018). Motor-driven sliding slows down as they approach MT plus-ends decorated by crowded PRC1-KIF4A complexes, with the final overlap length scaling with MT lengths. Considerable evidence suggests that PRC1-KIF4A complex is responsible, along with Eg-5, for similar antiparallel MT sliding in anaphase B *in vivo* (Vuković et al., 2021).

It is conceivable that the essential role of KIF4A, in complex with PRC1, in antiparallel MT sliding explains why in its absence a well-arranged central spindle fails to organise. In addition, upon KIF4A reduction in anaphase B, cells experience hyper-segregated chromosome halves (Kurasawa et al., 2004; Nunes Bastos et al., 2013). This is likely due to hyper extended, though disorganised, MT bundles pushing chromosomes apart, suggesting KIF4A is crucial for midzone length control (Hu et al., 2011). What property of KIF4A might explain this specific overlap length regulation?

In *Xenopus*, the KIF4A orthologue, Xklp1, effectively blocks plus-end dynamics *in vitro* at a high concentration (Bringmann et al., 2004). At physiological concentrations, along with PRC1, KIF4A forms an efficient two component system *in vitro* that specifically controls antiparallel overlap length, with PRC1 recruiting KIF4A and providing specificity for antiparallel overlaps (Fig 2C) (Bieling et al., 2010). Control of overlap length at this minimal reconstituted midzone is mediated by relative concentrations of the two proteins with higher amounts of KIF4A leading to shorter overlaps (Bieling et al., 2010; Hannabuss et al., 2019). Upon KIF4A knockdown, metaphase bridging fibres also undergo similar extension suggesting the same KIF4A mediated length control of PRC1 crosslinked overlaps is used both in metaphase and in late anaphase (Jagrić et al., 2021). Such specific control of antiparallel

overlap length is also used to prune astral overlaps in large *xenopus* oocytes demonstrating adaptation of this modular two component system *in vivo* (Nguyen et al., 2018).

### c) Motors for mechanical stability

In fission yeast, MT sliding in the spindle midzone is responsible for anaphase B spindle elongation. The principal motor executing this important function is kinesin-6, Klp9, which localises and concentrates at the central spindle in anaphase (Fu et al., 2009). Klp9p is recruited at the spindle midzone by its interaction with the C-terminal tail of Ase1p, the major component organising antiparallel MT bundles (Fu et al., 2009). This interaction at the spindle midzone stabilises both the components, with a sharply reduced FRAP recovery rate in anaphase. For a kinesin motor, to autonomously execute MT sliding, it must undergo sufficient oligomerisation to be able to both bind and move MTs in opposite directions. Indeed, *in vitro* purified Klp9p exists as stable combination of dimers and tetramers (Fu et al., 2009). Although direct *in vitro* evidence of MT sliding, akin to kinesin-5, Eg5, is lacking, Klp9p can influence rate of spindle elongation in a dose dependent manner *in vivo*, suggesting teams of Klp9p can act together to generate additive forces (Krüger et al., 2019). Along with controlling the rate of spindle elongation, Klp9p was recently shown to influence MT polymerisation speed (Krüger et al., 2021). Working with monopolar spindles, formed after inhibition of kinesin-5, Kruger et al., 2021, provided evidence for Klp9p localisation at the tip of MT bundles and increasing MT polymerisation rate. This was also corroborated by *in vitro* experiments with purified Klp9p. However *in vitro*, Klp9p also appeared to decrease MT polymerisation rate at high tubulin concentration in a dose-dependent manner contrary to its role in enhancing the same at low tubulin concentration, suggesting Klp9p acts to set a constant polymerisation rate across variable tubulin concentrations (Krüger et al., 2021). How the same motor can tune the rate of tubulin incorporation, either enhancing or reducing polymerisation speed depending on tubulin concentration remain a mystery.

Role of kinesin-6 orthologues in central spindle organisation appears to be remarkably well conversed (Adams et al., 1998; Raich et al., 1998). Like Klp9p, the mammalian orthologue, MKLP1 (also known as CHO1), first identified as a spindle localised mitotic MAP, is responsible, in conjunction with Eg-5, for anaphase spindle elongation (Nislow et al., 1992). However, unlike Klp9p, kinesin-6 orthologues in higher eukaryotes exist in a complex with RacGAP subunit, MgcRacGAP50 (Touré et al., 1998). This complex, first identified and characterised in *C.elegans*, is termed Centralspindlin, owing to its vital role in organising

central spindle (Mishima et al., 2002). Deletion of either of the subunits of this complex leads to a disorganised central spindle and cytokinesis failure (Jantsch-Plunger et al., 2000; Raich et al., 1998). In addition, the localisation of either member of the complex to spindle midzone is dependent on the other (Mishima et al., 2002). Centralspindlin exists as a stable heterotetrameric complex of a dimer of kinesin-6 subunit, Zen-4 and a dimer of RacGAP subunit-Cyk-4 in *C.elegans* (Mishima, 2017; Mishima et al., 2002; Pavicic-Kaltenbrunner et al., 2007). The RacGAP subunit, Cyk-4, is well-conserved across evolution and is thought to influence cytokinesis by altering the activity of ECT-2, the principal Rho GTPase directing the assembly of cytokinetic actin ring (Yüce et al., 2005). Thus, by physically interacting with the motor component, the complex provides a crucial link between central spindle assembly and cytokinesis. How does this interaction affect the function of Zen-4, the kinesin-6 subunit? This is of substantial interest because the N-terminal ~40 amino acids of Cyk-4 directly contact the neck linker section of Zen-4, a region important for directionality and force generation in other kinesin sub-classes (Davies et al., 2015). Although detailed ultrastructural evidence probing this interaction is presently unavailable, careful analysis of bead movement indicates that Cyk-4 association allows for frequent side-stepping of the complex to a neighbouring protofilament, circumventing obstacles on MTs (Maruyama et al., 2021). Cyk-4 binding causes Zen-4 to preferentially bundle overlapping antiparallel MTs in vitro compared to Zen4 alone which exhibits a slight preference for parallel overlaps (Davies et al., 2015). The specific contribution of the RacGAP subunit to motor activity of the complex may also be species specific. This bodes well with the observation that although the interaction between the subunits is broadly conserved, there is considerable sequence variation within the contact region. Indeed, the *Drosophila* Zen-4 orthologue, Pavarotti is activated solely as part of complex with Tumbleweed, the Cyk-4 orthologue but not without it (Tao et al., 2016). This is in direct contrast with *C.elegans* Centralspindlin complex wherein, Zen-4 activity, measured by MT gliding velocity, is reduced on Cyk-4 binding, suggesting a brake like mechanism.

Similar to Ase1-Klp9 interaction in fission yeast, the *C.elegans* Centralspindlin complex has been shown to directly bind the PRC1 orthologue, SPD-1, with the C-terminal of SPD-1 interacting with the last coiled coil and tail region of Cyk-4 subunit (Lee et al., 2015a). Disruption of this interaction results in spindle breakage in late anaphase after normal formation of central spindle, indicating that SPD-1 interaction with Centralspindlin complex is not necessary for central assembly per se but is required for its maintenance. The requirement for this interaction could be compensated by a reduction in cortical pulling forces acting to

segregate the spindle poles in anaphase B (Lee et al., 2015a). Thus, SPD-1-Centralspindlin complex interaction is critical for structural resilience of the central spindle under pulling forces in cells.

In contrast to other kinesin motors, Zen-4, as part of the Centralspindlin complex, shows extremely poor processivity in vitro with most motors unbinding after a short distance (Hutterer et al., 2009). How does the Centralspindlin then reach the spindle midzone, where two opposing spindle halves meet with their plus ends in antiparallel orientation? In cells, Centralspindlin is observed to translocate as distinct punctate clusters (Hutterer et al., 2009). Clustering of the complex, mediated by a short coiled-coil region in the C-terminal of Zen-4, dramatically improves processivity of the complex by 5-fold in vitro, demonstrating that multiple motors can periodically engage with the MT lattice, reducing the off-rate of the complex. Consequently, a Zen-4 mutant lacking the clustering region (586-601), fails to localise at the midzone and leads to cytokinesis failure (Hutterer et al., 2009).

Once at the central spindle, Centralspindlin complex appears remarkably stable. However, as the central spindle matures into midbody, recent careful immunofluorescence analysis indicates that MKLP1 and by association the Centralspindlin, occupies a central ring like localisation around the densely bundled MTs, distinctly different from PRC1, which still resides at the narrow MT bundle (Hu et al., 2012) . What might contribute to this relocalization? The Centralspindlin complex, specifically the Cyk-4 subunit contains an atypical C1 domain that has been previously shown to bind membrane lipids, PI(4)P and PI(4,5)P<sub>2</sub> , albeit weakly (Lekomtsev et al., 2012). Mutations abolishing this membrane association leads to furrow regression at the midbody stage leaving in its wake an unusual gap between the ingressing membrane and the midbody which are otherwise tightly juxtaposed in wild type cells at this stage. This has led to the exciting proposal that during cytokinesis, Centralspindlin directly links the bundled MTs of the midbody to the overlying plasma membrane (Lekomtsev et al., 2012).

While other proteins namely, MKLP2, CEPP55, Aurora B kinase, also participate in central formation (Carmena et al., 2012; Glotzer, 2009), PRC1, KIF4A and Centralspindlin constitute the principal mechanical parts of the structure. In accordance with observations of asymmetric central spindle (Derivery et al., 2015), a mechanically robust central spindle would also have to accommodate structural flexibility to perform its various functions. The major question

therefore is how do these components come together to form such a structure? And how do different kinesins, such as Klp98A, move on such tracks? (See Thesis Aims)

## Thesis Aims

Most of our understanding of complex biological systems stem from observations made upon disrupting a component of the system. While this approach remains a cornerstone in our understanding of any cellular process, key insights have been gained when this is combined with a bottom-up reconstitution approach. For instance, while Sec mutants had pioneered the field of membrane trafficking, reconstitution of protein trafficking using purified components had led to the breakthrough discovery of COPI (coat protein I) and COPII (coat protein II) (Orci et al., 1986). Such reductionist approaches offer several key advantages- firstly, by taking away the complexity and redundancy of cellular systems, it provides a platform to uncover minimal set of components sufficient to recapitulate a cellular process. For instance, pioneering studies of mitotic spindle reconstitution using DNA coated microspheres in cell lysates showed that neither centrosomes nor kinetochores were required for spindle assembly (Heald et al., 1996). Secondly, by studying components in isolation unforeseen molecular behaviour may emerge that underscores flexibility or limitation of a system (Surrey et al., 2001). Importantly, once reconstituted, such system offers a fundamental platform to study direct effects of other key components.

Therefore, for my PhD project, I attempted to:

**1) Reconstitute an asymmetric central spindle-like architecture to study endosome motility**

Using purified proteins, I attempted to recapitulate key features of central spindle MT architecture (Chapter 4,5,6) including importantly a defined region of stable densely bundled antiparallel overlap (Chapter 5 and 6). My aim is to use this system to study how motors move on such tracks and therefore a high density of MT tracks with the option of modulating its density, to create asymmetric overlaps, is of paramount importance. This is assisted by micropatterning MT seeds at sufficiently high density (Watson et al., 2021) (Chapter 4)

**2) Uncover endosomes that also exploit the central spindle geometry**

Indeed, while it seems unlikely that all organelles/cargo in the cell require biased dispatch, the central spindle in dividing SOPs is always asymmetric (Derivery et al., 2015). This asymmetry could for instance be bypassed by recruiting motors of opposite polarity (tug-of-war), or by changing the motor characteristics. Are there cargoes that also exploit central spindle track but segregate symmetrically?

To address this question, I attempted to find cargoes that are targeted to the central spindle during SOP division yet are symmetrically dispatched (Chapter 3).

It must be emphasized that these questions are general and thus the results will be applicable beyond asymmetric cell division to all forms of polarised transport where MT overlaps are observed, for instance in neurons (Hirokawa et al., 2010).



# **Chapter 2**

## **Materials and Methods**

Unless stated otherwise, all reagents were obtained from Sigma.

### **2.1. Protein Purification**

All protein purifications were performed at 4°C. Final protein concentrations were measured by gel densitometry with known Bovine Serum Albumin (BSA) standards and independently confirmed by absorbance at 280 nm (NanoDrop, Thermo). (See section 2.14 for cloning of the constructs used)

Full length recombinant *Drosophila* proteins, Faschetto (Feo) and Kinesin-like protein 3A (Klp3A), were purified by expression from a homologous system, D.Mel2 cells grown in suspension. Cells were transfected with puromycin resistant plasmids containing the protein of interest with a C-terminal protein C (PC) epitope tag and induced with 0.5mM Cu<sup>2+</sup> for three days before harvesting.

For purification of Feo-GFP-PC conditions were adapted from those described previously for its homologue in Xenopus (XPRC1) and human (PRC1) (Bieling et al., 2010; Subramanian et al., 2013). Briefly, cells were lysed in Buffer A (20 mM K<sup>+</sup>HEPES pH 7.4, 400 mM KCl, 5% Glycerol, 1 mM DTT) supplemented with CaCl<sub>2</sub> and 2X cOmplete protease inhibitors (Roche) by Dounce homogenisation. Lysates were clarified by ultracentrifugation at 45000 rpm in a Ti70 rotor for 30 mins and the supernatant was allowed to bind HPC4 resin for 2 hrs. Resin was subsequently washed with two column volumes (CV) of Buffer A supplemented with CaCl<sub>2</sub> and two CV of only Buffer A. Protein was eluted in Buffer A supplemented with 5mM EGTA in 1ml fractions. Peak fractions were pooled and concentrated (Amicon UltraPure 10KDa). Further purification was performed by size exclusion chromatography on Superdex 200 increase 10/300 column (GE healthcare) equilibrated with Buffer A, at a flow rate of 0.45 ml/min. Relevant fractions, assessed by SDS-PAGE, were concentrated to 1mg/ml before addition of sucrose to a final 20% (w/v) and flash frozen in liquid nitrogen. Once thawed, Feo-GFP-PC was stable for 1 hr on ice in storage buffer (buffer A + 20% sucrose).

For Klp3A-GFP-PC, identical procedures were followed except buffer A was modified to contain 20mM K<sup>+</sup>HEPES pH 7.4, 300mM KCl, 10% Glycerol, 1mM DTT, 1mM MgCl<sub>2</sub> and 0.1mM ATP.

Recombinant motor domains of Kinesin-1(dKHC1-400) and Kinesin-3 Klp98A (1-400) were expressed and purified from *E. coli* BL21 (DE3) pLysS rosetta 2 cells (Novagen), grown in 2XTY till O.D.600 of 0.6 and induced with 0.5 mM IPTG and 30 mg/L biotin overnight at 18°C.

For purification of dKHC (1-400) BCCP PC (His)<sub>6</sub>, cells were lysed in 20 mM K<sup>+</sup>HEPES pH 7.4, 150 mM KCl, 10% Glycerol, 1 mM DTT, 1 mM MgCl<sub>2</sub>, 0.1 mM ATP and 20 mM Imidazole supplemented with 1% Triton X-100, 0.7 mg/ml Lysozyme, 10 ug/ml DNase I and 1X cOmplete protease inhibitors by sonication (40% amplitude) for 10 min. Lysate was clarified at 30,882 x g for 30min by centrifugation in a Beckman JA25.5 rotor before incubating with Ni-NTA-Agarose beads (Qiagen, 30210) for 2hr with rocking. Beads were subsequently washed with three CV of wash buffer (20 mM K<sup>+</sup>HEPES pH 7.4, 150 mM KCl, 10% Glycerol, 1 mM DTT, 1 mM MgCl<sub>2</sub>, 0.1 mM ATP and 20 mM Imidazole) by gravity flow followed by High ATP wash (wash buffer with 10mM ATP, 10mM MgCl<sub>2</sub>) to remove associated chaperones. This was followed by a single wash with one CV wash buffer before eluting in final elution buffer – 20 mM K<sup>+</sup>HEPES pH 7.4, 150 mM KCl, 10% Glycerol, 1 mM DTT, 1mM MgCl<sub>2</sub>, 0.1mM ATP and 250mM Imidazole. Peak fractions, monitored by Bradford assay, were pooled and further purified by anion-exchange chromatography. For anion-exchange chromatography, sample was first diluted 1:11 (vol eluate:vol QA) in buffer QA (20 mM Hepes, 20 mM KCl, 1 mM MgCl<sub>2</sub>, 0.05 mM ATP, and 1 mM DTT, pH 7.6). This sample was loaded onto an MonoQ 5/50 GL (GE healthcare) anion exchange column (0.5 ml/min) and eluted in a 0.05–1 M gradient of KCl. Relevant fractions were pooled, dialyzed against storage buffer (20 mM K<sup>+</sup>HEPES, pH 7.4, 150 mM KCl, 1 mM MgCl<sub>2</sub>, 0.05 mM ATP, 1 mM DTT, and 20% (w/v) sucrose, pH 7.6), flash frozen in liquid N<sub>2</sub>, and kept at -80°C.

Klp98A (1-400) BCCP PC His was purified by similarly except ion-exchange was replaced by size-exclusion chromatography (SEC) using a Superdex 200 increase 10/300 column (GE), operated at 0.45 ml/min.

GFP-Ase1-His<sub>6</sub> was purified as described previously(Janson et al., 2007). Briefly, cells were lysed in 25 mM K<sup>+</sup> Phosphate buffer pH 7.4, 300 mM KCl, 1 mM DTT and 30 mM Imidazole supplemented with 1% Triton X-100, 0.7 mg/ml Lysozyme, 10 µg/ml DNase I and 1X

cComplete protease inhibitors by sonication. Lysate was centrifuged at 30,882 x g for 30 min and the supernatant was incubated with Ni-Agarose beads for 2hrs. Resin was then washed with three CV of wash buffer (25 mM Phosphate buffer pH 7.4, 300 mM KCl, 1 mM DTT, 30 mM Imidazole) and eluted in the same buffer with 250 mM Imidazole. Elution fractions were pooled and concentrated to 200 $\mu$ L (Amicon ultra 3KDa cut-off). Protein was further purified by SEC on a S200 increase 10/300 column (0.5ml/min) and resulting fractions were pooled and dialysed in 25 mM Phosphate buffer pH 7.4, 300 mM KCl, 1mM DTT and 20% Glycerol.

Recombinant *C. elegans* Centralspindlin complex, a heterotetramer of N-terminal Chitin binding domain (CBD) tagged ZEN-4 motor and N-terminal GST tagged CYK-4, was purified as described previously (Mishima, 2017). Briefly, since the complex not individual components is the active entity, a two-step affinity purification ensures stoichiometric purification which is further validated by gel filtration. Cells were first lysed in 20 mM Tris pH 8.0, 300 mM KCl, 10% Glycerol, 1 mM DTT, 1 mM MgCl<sub>2</sub>, 0.1 mM ATP with 0.1% Triton X-100, 0.7 mg/ml Lysozyme, 10 ug/ml DNase I and 1X cComplete protease inhibitors by sonication. Following centrifugation, clarified lysate was incubated with Chitin beads for 4hrs. Beads were then washed once with wash buffer (20 mM Tris pH 8.0, 300 mM KCl, 10% Glycerol, 1mM DTT, 1mM MgCl<sub>2</sub>, 0.1mM ATP) followed by once with High ATP buffer (20 mM Tris pH 8.0, 300 mM KCl, 10% Glycerol, 1 mM DTT, 10 mM MgCl<sub>2</sub>, 10 mM ATP) to remove a 14KDa chaperone that associates otherwise. Protein was eluted overnight by excess DTT (40 mM) in the same buffer. To remove excess ZEN-4 (not associated with CYK-4) the eluate was directly incubated with GST beads for 2 hrs. Beads were washed once with wash buffer and incubated overnight with excess GST-3C protease (GE) to cleave the GST tag. The resulting cleaved complex was then gel filtrated using a S200 increase 10/300 column, at 0.45 ml/min. Fractions containing both ZEN-4 and CYK-4 were pooled, concentrated to 1mg/ml and flash frozen with 20% sucrose(w/v).

For *Drosophila* Centralspindlin complex, CBD-TEV-Pavarotti-GFP-PC (ZEN-4 homologue) was expressed along with GST-3C-Tumbleweed in E.coli. Cells were lysed in 20 mM Tris pH 8.0, 300 mM KCl, 10% Glycerol, 1 mM DTT, 1 mM MgCl<sub>2</sub>, 0.1 mM ATP with 0.1% Triton X-100, 0.7 mg/ml Lysozyme, 10  $\mu$ g/ml DNase I and 1X cComplete protease inhibitors by sonication. Lysate was clarified by ultracentrifugation and the supernatant was incubated first with GST beads for 2hrs. Beads were washed with two column volume of wash buffer (20 mM Tris pH 8.0, 300 mM KCl, 10% Glycerol, 1 mM DTT, 1 mM MgCl<sub>2</sub>, 0.1 mM ATP) and eluted in the same buffer with 10mM reduced glutathione (pH 8.0). Eluate was incubated overnight

with both His-TEV and His-tagged Precision 3C protease (GE). Following protease cleavage, sample was incubated with 200 µL of HPC4 resin for 2hrs in 20 mM Tris pH 8.0, 300 mM KCl, 10% Glycerol, 1 mM DTT, 1 mM MgCl<sub>2</sub>, 0.1 mM ATP with 1 mM CaCl<sub>2</sub> to remove both proteases and cleaved fragments. Following binding, beads were washed with 10ml of wash buffer and eluted with 5mM EGTA. The complex was subsequently concentrated to 1 mg/ml and flash frozen with 20% sucrose (w/v).

## 2.2 Imaging

Imaging was performed on a custom built TIRF/Spinning disk confocal setup using a Nikon Ti2 stand with a fast piezo controlled z-stage (ASI) and a dedicated perfect focus system equipped with 405nm (100mW OBIS LX), 488nm (150mW OBIS LX), 561nm (100mW OBIS LX) and 637nm (140mW OBIS LX) solid state lasers. For uniform illumination across a large field of view, the TIRF system employed an azimuthal illumination module (iLas2, Roper France) modified with a custom-built large collimator (Cairn). TIRF imaging was performed with a PLAN Apo Lambda 100X NA 1.45 objective. Images were acquired using a Photometrics 95B back-illuminated sCMOS camera synchronised with the rotation of the azimuthal illumination. For imaging at 37°C, the entire stage and objective was heated using a custom temperature-controlled enclosure (Digital Pixel Microscopy). Uniform depth of field across different wavelengths was achieved by varying the TIRF angle independently for different channels. For dual colour imaging, sequential images were obtained by dedicated bandpass filters (Chroma 525/50, 595/50 and ET655LP) driven by a fast filter wheel (Cairn Optospin).

Confocal imaging for dissected fly notum was performed on the same system using a 60X PLAN Apochromat Lambda NA 1.4 objective at 25°C. Z stacks were acquired at 0.3 µm interval. The confocal arm was equipped with a Yokogawa CSU-X1 spinning disc head and a Photometrics back-illuminated 95B sCMOS camera synchronised with the rotation of the spinning disk head. For multi colour imaging, dedicated bandpass filters (Chroma 525/50, 595/50 and Chroma 680/40) were driven by a fast filter wheel (Cairn).

To enable fast acquisition, the entire setup is synchronized at the hardware level by a Zynq-7020 Field Programmable Gate Array (FPGA) stand-alone card (National Instrument sbrio 9637) running custom code. In particular fast z-stacks are obtained by synchronizing the motion of the piezo z-stage during the readout time of the cameras. Images were acquired by custom written codes in Metamorph software.

### **2.3 Coverslip Preparation**

For single molecule in vitro assays, clean room grade coverslips (Nexterion 22X22 mm) were first plasma activated under pure oxygen at 0.4mBar for 4min. Plasma activated coverslips were immediately immersed in 1mg/ml methoxy-polyethylenegyl-silane (mPEG-Silane) in 96% ethanol solution overnight. mPEG-Silane coated coverslips were sequentially cleaned in ethanol, ultra-pure water and dried with nitrogen gas flow. A custom chamber was then constructed between silanized coverslips and clean microscope slide (Thermo, 75X25 mm) with double-sided tape as spacer. To ensure reproducibility of the flow chamber volume, the double-sided tape was precisely cut within a cutting plotter (Graphtec). Each clean room assembled chamber contained three channels of approximately 12  $\mu$ L volume.

### **2.4 Photo-initiator synthesis**

For micropatterning experiments, we (me with the help of Dr. Emmanuel Derivery and Dr. Benjami Silva) synthesised the UV-based photo-initiator 4-bezoylbenzyl-trimethylammonium bromide (BTBB) as described previously (Watson et al., 2021). Briefly, 2.1 ml trimethylamine (2.2. eq, 16mM, Sigma) solution in 4.2 M ethanol (1.2 eq, 8.8 mmol; Sigma-Aldrich) was added to 2 gm of 4-(bromomethyl) benzophenone (1 eq, 7.3 mmol; Sigma-Aldrich) and diluted in 40 ml acetonitrile in a 100ml flask. The mixture was placed under reflux in a nitrogen atmosphere for 2hr. After completion of the reaction, the solvent phase was evaporated to obtain a white solid, further dried under vacuum. Purity of compound was verified by HPLC (95% pure) and matched the predicted molecular weight by NMR.

### **2.5 Optical design of UV-LED DMD illuminator**

Construction of the UV-LED based DMD illuminator for micropatterning was inspired from laser-based DMD illumination modules such as the one described by Straale and colleagues (Straale et al., 2016). The design incorporates a UV-DMD illumination onto the previously described TIRF setup for simultaneous micropatterning and TIRF imaging (See Fig 5A, Chapter 4). Briefly, a bright 385nm UV LED light source (1650 mW; Thorlabs; M385LP1), collimated an antireflective (AR)-coated aspheric lens (Thorlabs ; ACL2520U-A), is used to illuminate a DMD development board (DLPLCR6500EVM; Texas Instruments) at a 24° angle of incidence (the individual mirrors of the DMD have a tilting angle of 12°). The illumination pattern of the DMD is relayed onto the conjugate of the sample plane at the backport of the microscope through a 4f system ( $f_1 = f_2 = 125$  mm, Thorlabs; LB4913-UV). This intermediate image is further projected onto the sample plane by a 25 X 125mm UV rated tube lens (Edmond

Optics) and the objective (100× Plan Apochromat lambda NA 1.45 or 60× Plan Apochromat lambda NA 1.4). Combination of the DMD-UV illumination with TIRF illumination is achieved by an ultra-flat dichroic (Chroma; T470lpxr) placed after f2 within a custom backport assembly (Cairn). In DMD-UV illumination mode, a 473nm dichroic (Semrock; Di03-R473), compatible with spinning disk illumination, is placed onto the optical path. In TIRF illumination mode, this is replaced by a quad-bandpass ultraflat dichroic filter (Chroma; TRF89901-EM).

Our (me in collaboration with Dr. Joeseph Watson and Dr. Emmanuel Derivery) final design relies on a commercially available cage system (Thorlabs) with swivel couplers cut at the right length to set the +24° angle and a custom mount for the DMD board (machined by the LMB workshop). This greatly facilitates alignment of the setup, as this essentially locks all pieces into the correct angle during assembly, which is critical for alignment of DMD setups. Note that care must be taken with the adjustment of the collimating lens of the LEDs to find the best compromise between illumination intensity and flatness of the illumination profile. If necessary, a flatfield correction can be applied on the patterns to be displayed to account for any field inhomogeneities, and if extremely sharp patterns are required, an iris can be put in the Fourier plane between f1 and f2, but I found that this was not required for most applications.

LED intensity is controlled using a custom LED driver providing the maximum 1.7 A tolerated by the LED (2 A for 450 nm LED). Control over LED intensity and on/off state is operated using a digital/analogue card (USB-6001; National Instrument; or Arduino UNO equipped with a custom shield providing a Texas Instrument TLV5618 digital/analogue chip). Importantly, for micropatterning experiments, patterns generated by the DMD were focused using the UV reflection at the glass-water interface, imaged through the spinning disk arm of the system, instead of the perfect focus system of Nikon. Communication to the DMD board from the imaging software is performed using custom code using the DMD Connect library developed by Hueck (2016), available at <https://github.com/deichrenner/DMDConnect>. Control of all parts was integrated into Metamorph using custom scripts to calibrate the DMD with respect to the camera, display user-defined UV micropatterns, and facilitate micropattern alignment for multiprotein micropatterning.

## **2.6 DMD based micropatterning of Microtubules**

Microtubule micropatterning was adapted from the method developed by Portran and colleagues (Portran et al., 2013). In particular, I used a DMD based illuminator and BTBB (Strale et al., 2016) instead of predefined quartz mask for micropatterning. Briefly, PEG-silane coated custom chambers were used for all micropatterning experiments. Regions of interest drawn on the DMD and focused onto the BTBB solution (13.5 mg/ml in 0.1M carbonate buffer pH 9.1) were illuminated for 3sec per field of view. BTBB was removed by washing with more than three times the chamber volume (~40 µL) of carbonate buffer followed by incubation with first anchor protein, fibrinogen-biotin-490LS diluted 20 µg/ml in carbonate for one minute. Next, excess fibrinogen-biotin-490LS was removed by washing with excess carbonate buffer and coverslip was passivated by 0.1 mg/ml PLL-g-PEG (SuSOS chemicals) in 0.1M HEPES buffer pH 7.4. Passivation was further strengthened by 5% Pluronic and 0.5 mg/ml K-casein in HEPES buffer for 5 min. Finally, 0.1 mg/ml Neutravidin was added to the chamber to form a biotin-neutravidin layer. After removal of the excess Neutravidin by BRB80 buffer (80 mM PIPES, pH 6.9, 2mM MgCl<sub>2</sub>), short MT seeds, made fresh on the day of the experiment (see Section 4.9), was added at a high concentration (1µM, in BRB80 buffer) and allowed to bind the pattern. For MT polymerisation from patterned seeds, unless otherwise specified, soluble tubulin was added at 12 µM with proteins at indicated concentrations.

## **2.7 Gliding Assay**

Kinesin functionality was tested by gliding assays for dKhc1, Klp98A, Klp3A, Pavarotti. Coverslips silanized with dichlorodimethylsilane (0.2%) in trichloroethylene for 30 mins. Coverslips were subsequently washed with methanol and ultrapure water before drying under nitrogen flow and storing them under inert gas. Kinesins were attached to the coverslip with anti-PC antibody diluted to 0.02 mg/ml in 0.1M HEPES buffer. Non-specific adsorption of kinesins was prevented by passivating the coverslip with 5% Pluronic acid and 1mg/ml K-casein sequentially. Finally, kinesins were added at a final concentration of 0.05 mg/ml in Motility buffer (See below for composition). After binding of kinesins for 5-10min excess protein was removed by washing the chamber with 40 µL of Fluorescence buffer. GMPCPP stabilised rhodamine labelled microtubules were flowed in 0.05 µM in motility buffer. Images were acquired every 100ms for 5min.

For truncated motor domains of dKHC1-4001 and Klp98A 1-400 motility buffer contained BRB80 (80 mM PIPES/KOH pH 6.9, 2 mM MgCl<sub>2</sub>) 1mM ATP, 0.5 mg ml<sup>-1</sup> K-casein, 0.2%

methylcellulose (4000cP) and anti-fade (40 mM glucose, 40 µg/ml glucose oxidase, 16 µg/ml catalase, 40 mM DTT). For full-length kinesins, Klp3A and Pavarotti, motility buffer contained additional salts with the final composition being 10 mM HEPES pH 7.4, BRB40 (40 mM PIPES/KOH, pH 6.9, 1 mM MgCl<sub>2</sub>), 1 mM ATP, 0.5 mg/ml K-casein, 0.2% methylcellulose (4000cP) and anti-fade (40 mM glucose, 40 µg/ml glucose oxidase, 16 µg/ml catalase, 40 mM DTT) supplemented with 75 mM KCl and 50 mM K-Glutamate.

## 2.8. In vitro motility Assay

Flow chambers assembled from silanized coverslips as described above were first incubated with anti-tubulin (diluted to 0.02 mg/ml in BRB80) antibody to immobilise stable microtubules in the chamber. Chamber was then passivated by 5% Pluronic acid and 1mg/ml K-casein. Long (>4µm) GMPCPP stabilised microtubules were added at a final concentration of 0.05µM in BRB80 for 5 min. Chambers were washed with Motility buffer to remove unattached microtubules. Motor domains of kinesins, dKHC(1-401)BCCP PC His and Klp98A(1-400) BCCP PC His, were bound to streptavidin coated Quantum Dots (Agilent technologies) at equimolar concentrations and incubated for 5min on ice. To observe movements of single QDs onto MTs, kinesins-bound Quantum dots were added at a final concentration of 10nM in Motility buffer. Relatively broad spectrum of excitation for QDs allowed multiplex imaging with 488nm laser used to excite QD705 and visualised with a 680 nm LP filter. Images were taken every 200 ms for 10min per chamber.

## 2.9 Preparation of Stabilised microtubules

For micropatterning experiments, short (<1.5 µm), biotinylated seeds were made by first mixing 4 µL of 50 µM Rhodamine tubulin (Cytoskeleton; TL590M) with 21 µL of Biotinylated tubulin (a kind gift from the Blanchoin-Thery lab) in BRB80 supplemented with 0.5mM GMPCPP (Jena Biosciences) to yield a 15% rhodamine labelled biotinylated tubulin solution. The solution was cleared of aggregates by ultracentrifugation at 100,000 rpm for 5 min in TLA120.1 rotor at 4°C, aliquoted and stored in liquid nitrogen. On the day of the experiment, 1.2 µL of this mixture was directly thawed at 37°C with the addition of fresh 0.5mM GMPCPP and 40 µM taxol (in DMSO) and polymerised for 30min. Polymerised seeds were pelleted in a table-top centrifuge at 13,000 rpm for 8min and diluted in BRB80-0.5mM GMPCPP to 1uM and kept at room temperature till use.

For in vitro gliding assays, long stabilised MTs (<4µm) were generated similarly by polymerising 50µM non-biotinylated tubulin at 37°C in BRB80 supplemented with 0.5mM

GMPCPP without the addition of docataxel. For in vitro motility assays, non-biotinylated tubulin was first diluted to 10  $\mu$ M and polymerised at 37°C in BRB80-GMPCPP to generate longer microtubules ( $> 6\mu$ M).

## 2.10 Microtubule Polymerisation

Tubulin polymerisation from stabilised seeds was done as described previously (Portran et al., 2013). Importantly, background binding of tubulin was observed to be significantly lower in mPEG-Silane coated coverslips and all MT polymerisation experiments were performed on the same. Chamber was first incubated with 40  $\mu$ g/ml Fibrinogen-biotin in carbonate buffer followed by passivation by 5% Pluoronic and 1mg/ml K-casein. Next Neutravidin at 0.1mg/ml in 0.1M HEPES was added to create a biotin-Neutravidin sandwich. Short GMPCPP stabilised seeds were introduced in the chamber at 0.05 $\mu$ M in Fluorescence buffer (BRB80, 0.5 mg/ml K-casein, 0.2% methylcellulose (4000cP) and 40 mM glucose, 40  $\mu$ g/ml glucose oxidase, 16  $\mu$ g/ml catalase, 40 mM DTT). Unless otherwise specified, soluble tubulin was introduced at 12  $\mu$ M. Final buffer in the chamber contained 30% BRB80 and 70% Fluorescence buffer with 1mM GTP. For experiments involving purified proteins along with tubulin, the final buffer contained 30% BRB80, 69.4% Fluorescence buffer with salt and 0.6% of storage buffer of indicated proteins. Images were acquired every 5sec for 20min at 37°C unless otherwise specified.

## 2.11 Synthesis of Fibrinogen-Biotin

Fibrinogen solution of 11  $\mu$ M, made freshly in 0.1M Carbonate buffer was incubated with 10X molar excess of EZlink-LC-LC-Biotin (ThermoFisher;21343), freshly made in anhydrous DMSO (Invitrogen; D12345) for 1 hr at room temperature. Excess NHS-LC-LC-Biotin was then removed by Zeba Spin column equilibrated with 0.1M carbonate buffer. Fibrinogen-biotin-490LS was made similarly by first reacting a 3X molar excess of ATTO490LS NHS ester for 15min followed by a reaction with 40X molar excess of NHS-LC-LC-Biotin for 1 hr at room temperature. Excess esters were similarly removed by Zeba Spin colum. Degree of labelling was measured by absorbance measurements at 280 and XYZ nm and was found to be 2.4 (mol of dye:protein).

## 2.12 Cloning

All constructs were cloned using conventional restriction cloning and sequenced. All Open Reading Frames (ORFs) cloned by PCR for this study were flanked by FseI and AscI sites for convenient shuttling between compatible plasmids.

For eukaryotic protein expression from *D. mel2* cells, a suspension adapted derivative of S2 cells, were expressed from pMT puro plasmids (Derivery et al., 2015), containing a copper inducible metallothionein promoter. *Drosophila* Kinesin-4, Klp3A, was amplified from fly w1118 cDNA using the following primers-

Fse1\_Klp3A 5'-ATGCGGCCGGCCATGTCCAGCGAGGATCCCAG- 3'

Asc1\_Klp3A 5'-ATGCGGCCGGCCAAAGAATTTCGCTTGGCG-3'

The resultant fragment was fused C-terminally to GFP followed by a protein-C (PC) and (His)<sub>6</sub> tag. Proteins tagged with PC binds to anti-PC antibody in a reversible calcium dependent manner and can be eluted by calcium chelating agent EGTA. *Drosophila* homologue of PRC1, Faschetto (Feo) was similarly PCR amplified from fly cDNA using the following primers-

Fse1\_Feo 5'-ATGCGGCCGGCCATGAACCTGCCAGCGCCAT-3'

Asc1\_Feo 5'-ATGCGGCCGGCCCGAACTGTCTGCGCGGCTGCACG-3'

For expression in Bacteria, *Drosophila* Kinesin-1 active motor fragment, (dKhc 1-401) fused C-terminally to a biotin carboxyl carrier protein (BCCP) followed by six histidine tags was a kind gift from Jeff Gelles (Department of Biochemistry, Brandeis University, Waltham, MA; Addgene plasmid no. 15960). *Drosophila* Kinesin-3, Klp98A fragments were codon optimised and the corresponding DNA sequenced synthesised (G-blocks, IDT). The resulting gene fragment was cloned into a modified pET 42 vector engineered to contain FscI and AscI sites and fused C-terminally to tandem BCCP, protein C (PC) and (His)<sub>6</sub> tags. *Drosophila* Kinesin-6, Pavarotti along with its binding partner Tumbleweed was cloned into a modified pGEX bicistronic vector, gifted kindly by Masanori Mishima (Department of Biochemistry, Warwick University, UK). A synthetic codon-optimised Tumbleweed construct, truncated after the first 40 amino acids to increase solubility, was synthesized by IDT and fused N-terminally with GST followed by Precision 3C protease cleavage site (LEVLFQ|GP). Full length Pavarotti, amplified from fly cDNA, was inserted into the vector with an N-terminal chitin-binding domain (CBD) and TEV site (ENFLYQ|G) and C-terminal GFP tag followed by protein-C (PC) tag. The resulting CBD-TEV-Pavarotti-GFP-PC was inserted downstream of a second

ribosome binding site (RBS) to complete the bicistronic vector. Plasmid containing Ase1, expressed with an N-terminal His tag and C-terminal GFP tag as His-Ase1-GFP (Janson et al., 2007), was a kind gift from Phong Tran (Institute Curie, France).

### **2.13 Cell culture and transfection**

D.mel2 cells are derived from fly embryos and can be grown in serum free medium in suspension with a typical doubling time 48hrs. Cells were grown in Insect Express medium (Lonza) without serum at 27°C at 140rpm.

On the day of transfection, D.mel2 cells were diluted to  $2.5 \times 10^6$  in 50 ml fresh medium and allowed to grow for 30min. 50ml of cells were transfected with cellfectin II transfection (thermo) by preparing a mixture of 2 mL Opti-MEM with 60ul Expi fectamine and 25 $\mu$ g of vector. After one day, cells were resuspended in 25 mL Insect Express medium without serum and puromycin at 2.5  $\mu$ g/ml. Transfected cells were selected for two weeks by adding fresh medium every alternate day. Cell density was always maintained between 10 to  $30 \times 10^6$  cell/mL throughout. Large scale culture was performed in 2L roller bottles (500 mL/bottle). Cells were induced for three days by addition of CuSO4 at 0.5mM before harvesting.

### **2.14 Antibody uptake assay**

Monoclonal antibody against Notch-ligand Delta labelled with NHS-Atto647N was used through- out the assay at 3.6  $\mu$ g/ml. Antibody uptake was performed according to Loubéry et al. 2014 (Loubéry and González-Gaitán, 2014). Briefly, notum was dissected and washed in 800uL Clone 8 media to wash away the associated fat body. A day prior to the experiment, pupae were staged for imaging. Most of the SOPs divide within a time window of 2 hrs at 25°C, with the first division occurring around 16 hr post puparium formation at 25°C. The notum subsequently incubated with anti-delta antibody in 250uL clone8 media at a final concentration of 3.6  $\mu$ g/ml. After 5 min of pulse, the notum was washed successively in two 1 ml clone 8 baths. Finally, the notum was incubated in Fibrinogen (1mg/ml) for 1 minute before transferring to imaging dish (Fluoro-dish), fibrinogen was clotted with Thrombin (1ul of 10U/ $\mu$ l) and imaged in 300ul of Clone8 media at 25°C. Notum was imaged within 10-45 min for early endosome detection and post 50 min for late endosomes.

### **2.15 Fly genotypes**

For Figure 1:

Jupiter-GFP:  $w^{1118}$ ; *UAS-mRFP-Pon/+*; *neur-Gal4, Jupiter-GFP/+*

For Figure 2:

Rab 7:  $w^{1118}$ ; ; *neur-Gal4, UAS-mRFP-Pon/ Rab7-GFP*

Rab 5:  $w^{1118}$ ; *Rab5-GFP /+; neur-Gal4, UAS-mRFP-Pon/+*

For Figure 3:

Rab 6:  $w^{1118}$ ; *Rab6-YFP /+; neur-Gal4, UAS-mRFP-Pon/+*

Rab 4:  $w^{1118}$ ; *Rab4-YFP /+; neur-Gal4, UAS-mRFP-Pon/+*

## 2.16 Image analysis

All images acquired were processed by FIJI/ImageJ (Schindelin et al., 2012). Registration of time-lapse images were performed by cross-correlation between successive frames using a custom GPU based code (developed by Emmanuel Derivery) to correct for drift during acquisition.

### Average spindle

For Fig 5 average spindles were generated as in Derivery et al., 2015, with Jupiter-GFP used as a marker for spatio-temporal registration instead of Pavarotti-GFP. Briefly, all images were aligned spatially by a cartesian coordinate generated from the Jupiter-GFP signal. As Jupiter-GFP contracts during anaphase progression, this was used to generate a time reference. All movies, sum z projected, were thus aligned spatio-temporally by their Jupiter-GFP signal. To reduce rotation artifacts during registration, bicubic interpolation was performed post image scaling (by 4 without interpolation). Average spindle was generated from these registered movies by background subtraction and signal normalisation.

### Endosome tracking

For Fig 5 endosomes were tracked as in Derivery et al., 2015. Briefly, a 2D gaussain fit was employed to indetify endosomes. A vogel algorithm was used to track these particles in z proected (max projection) images (Holtzer and Schmidt, 2009).

### Micropatterning efficiency

To quantify micropatterning efficiency as in Fig 9 and 10, we (me along with Dr. Joseph Watson and Dr. Emmanuel Derivery) developed three parameters-

a. Pattern selectivity denoted by

Selectivity=

$$\frac{(\text{Average Intensity}_{\text{Pattern}} - \text{Average background}_{\text{camera}})}{(\text{Average Intensity}_{\text{NonPattern}} - \text{Average background}_{\text{camera}})}$$

b. Pattern Homogeneity =

$$\frac{(\text{Average Intensity}_{\text{Pattern}} - \text{Average background}_{\text{camera}})}{(\text{Variance Intensity}_{\text{Pattern}} - \text{Variance background}_{\text{camera}})}$$

Average Intensity<sub>Pattern</sub> denotes Average Fluorescence intensity of protein in the micropatterned region, Average background<sub>camera</sub> denotes Average background noise of the camera, Average Intensity<sub>NonPattern</sub> represents average fluorescence intensity of a non-patterned zone neighbouring the patterned region. Variance Intensity<sub>Pattern</sub> denoted variance of the Fluorescence signal from the micropatterned region, Variance background<sub>camera</sub> denotes variance of background noise of the camera. All measurements were performed in region of interest (ROI) of identical size, with Average background<sub>camera</sub> and Variance background<sub>camera</sub> measured in the dark by blocking light access to the camera. In addition, a third parameter, Amount of bound protein, was also determined as (Average Intensity<sub>Pattern</sub> – Average background<sub>camera</sub>). This parameter is a non-normalised value and therefore could only be compared across same fluorophore.

### Tip cluster analysis

To automatically track tips (For Fig 15) where GFP signal of kinesins were enriched a custom code was developed (in collaboration with Dr. Emmanuel Drivery) by 2D gaussian fitting with thunderstorm to identify tips (Ben-Sasson et al., 2021; Ovesný et al., 2014). Automated Intensity measurement was performed across the fitted gaussian in MATLAB. Each spot was then reported back to the original image with an identifying number that was used to measure the MT length manually. The same code was applied over time, for Fig 16, and could

reproducibly track tips over time. Only tips tracked for more than 50 successive frames were considered for intensity analysis.

### **Kymograph analysis**

Kymographs were generated by an integrated multi-kymo plugin in ImageJ. Kymographs generated were analysed using “Analyze Kymo” function. Only tracks persisting for over 5 successive frames were analysed.

# Chapter 3

Cellular functioning depends on spatial organisation of organelles and vesicles inside cells (van Bergeijk et al., 2016). Large scale robust spatial arrangement of organelles and vesicles is achieved predominantly by molecular motors walking on cytoskeletal filaments (Mogre et al., 2020). Positioning of organelles and vesicles play a particularly pivotal role in the functioning of polarised cells, such as epithelial and neuronal cells. Polarised trafficking of endocytic vesicles, carrying growth factors, nutrients, receptors, and ligands, serve a myriad of cellular functions from cell growth, cell adhesion to signalling.

Endosomes, small membrane bound vesicles formed through plasma membrane invaginations, transport among other things transmembrane receptor and ligands (Doherty and McMahon, 2009). Endocytosis controls the abundance of available receptors at the cell boundary and therefore by consequence strength and period cellular signalling (Gonzalez-Gaitan and Jülicher, 2014). Receptor and ligands once internalised within endosomes can still potentiate signalling events. These signalling endosomes can act as important conductors of cell-to-cell communication. Notch signalling provides an excellent example of a major signalling event modulated by endocytic trafficking, influencing both the direct availability of receptors and ligands as well as formation of signalling endosomes containing internalised receptor-ligand complex (Bray, 2006) .

Across evolution, Notch signalling regulates cell fate during development (Artavanis-Tsakonas et al., 1999; Bray, 2006). Classic examples include development of neural stem cells and gut progenitor cells (Demitrack and Samuelson, 2016; Gaiano and Fishell, 2003; Kageyama et al., 2008; Lehmann et al., 1983; Poulson, 1940). Despite the diverse roles executed by Notch signalling, its fundamental arrangement remains fairly simple across different cell types. A transmembrane ligand, Delta in *Drosophila*, activates membrane exposed Notch receptor in a neighbouring, signal receiving cell (Fehon et al., 1990; Parks et al., 2000; Zeng et al., 1998). Interaction of Delta leads to gamma secretase dependent proteolytic cleavage of the Notch receptor, releasing a small Notch IntraCellular Domain (NICD) in the cytoplasm (Gordon et al., 2007, 2015; Kopan et al., 1994; Mumm et al., 2000; Schroeter et al., 1998). Translocation of the NICD fragment into the nucleus activates transcription of developmentally important Notch effector genes (Jarriault et al., 1995; Lieber et al., 1993; Struhl and Adachi, 1998). Development of External Sensory (ES) organs in *Drosophila* has emerged as a tractable system

for studying cell fate assignment by Notch signalling (Hartenstein and Posakony, 1990). Each ES organ (forming mechanosensory bristles) is composed to four cells and develops from a single Sensory Organ Precursor (SOP) through stereotypic cycles of division. First round of asymmetric SOP division produces an anterior, Notch inactive, signal sending pIIb cell and a posterior Notch active, signal receiving pIIa cell. Successive rounds of division lead the pIIb cell to form the inner neuron and sheath cells while pIIa division gives rise to outer hair and socket cell (Schweisguth, 2015). Notch signalling instructs formation of pIIa cells and unsurprisingly in its absence the fly cuticle is devoid of bristles (Hartenstein and Posakony, 1990).

Notch signalling asymmetry between the pIIa and pIIb cells is controlled by four redundant pathways, all of which require partitioning bias during SOP mitosis: a) Numb is partitioned asymmetrically to the anterior cortex during metaphase and is inherited by pIIb (Rhyu et al., 1994). Numb then acts to downregulate notch receptor in pIIb either by downregulating receptor recycling to plasma membrane and/or by inhibiting another Notch activator Sanpodo (Cotton et al., 2013; Hutterer and Knoblich, 2005); b) Neuralised, an E3 ubiquitin ligase also segregates into anterior pIIb cell (Le Borgne and Schweisguth, 2003) where it activates endocytosis of the Notch ligand Delta (Zeng et al., 1998) selectively in this cell. Endocytosis and subsequent recycling make Delta competent to bind Notch and produce a productive downstream signal; c) soon after division, a Rab-11 positive compartment is specifically established next to the centrosome of pIIb. Rab-11 then promotes Delta recycling and redundantly with numb and neutralised contributes to biased signalling (Emery et al., 2005) and last, d) polarized trafficking of Sara endosomes containing internalised Notch and Delta specifically into the pIIa cell (300% enrichment into this cell) (Coumailleau et al., 2009). Thus, while the endocytic traffic of Notch and Delta is directly affected by Numb, Neuralised and Rab11 mediated recycling Sara endosomes represent a unique subset of signalling endosomes.

Sara endosomes, a subset of Rab5 positive early endosomes, are trafficked through the MT tracks of the central spindle (Coumailleau et al., 2009; Derivery et al., 2015). In late anaphase, the central spindle structure, formed between segregated chromosomes, acquires structural asymmetry with a higher tubulin density on the anterior pIIb side compared to pIIa (Derivery et al., 2015). Higher density of MTs emanating from the pIIb side terminate with their plus ends pointing towards the pIIa side. Indeed, a PX domain containing kinesin-3, Klp98A, has been shown to transport Sara endosomes on this asymmetric central spindle towards the plus ends leading to partition bias towards pIIa (Derivery et al., 2015).

Are there other cargoes that are transported on the central spindle? Although direct evidence of movement on central spindle is lacking, in diverse cell types, during the later stages of cell division, equatorial zones neighbouring the site of cytokinesis experience a large flux of endocytic traffic (Albertson et al., 2005). Fusion of these endosomes provide additional membrane required to support cytokinesis. In addition, endosomal traffic delivers several important proteins regulating abscission, including Exocyst complex and ESCRT proteins (Albertson et al., 2005). In support of this, membrane associated Rab proteins, including Rab8, Rab35 and Rab11 has been shown localise to the furrow region (Yu et al., 2007). Rab11 and Rab11 family Interacting Protein (Rab11-FIP3) play a crucial role in delivery of ESCRT complexes and formation of a stable intracellular bridge (Fielding et al., 2005; Wilson et al., 2005). Along with Rab11, Rab35 is also reported to regulate abscission by its association with OCRL, a PI(4,5)P<sub>2</sub> phosphatase (Chesneau et al., 2012; Kouranti et al., 2006). Strengthening the evidence for the role of endocytic traffic in regulating cytokinesis, depletion of Clathrin leads to cytokinesis failure (Gerald et al., 2001).

During late stages of cell division, the spindle midzone experiences substantial membrane traffic. Does the central spindle also support motility of endosomes apart from Sara containing signalling endosomes? If so, then what are the identity of such vesicles and how do these endosomes partition? Does an asymmetric central spindle lead to asymmetric partitioning of all central spindle targeted endosomes? To answer these questions, I used a collection of Rab-GFP fusions and tracked their movement during cell division, focusing on late anaphase transport involving the central spindle.

## Results

### **Delta segregation pattern changes during late chase**

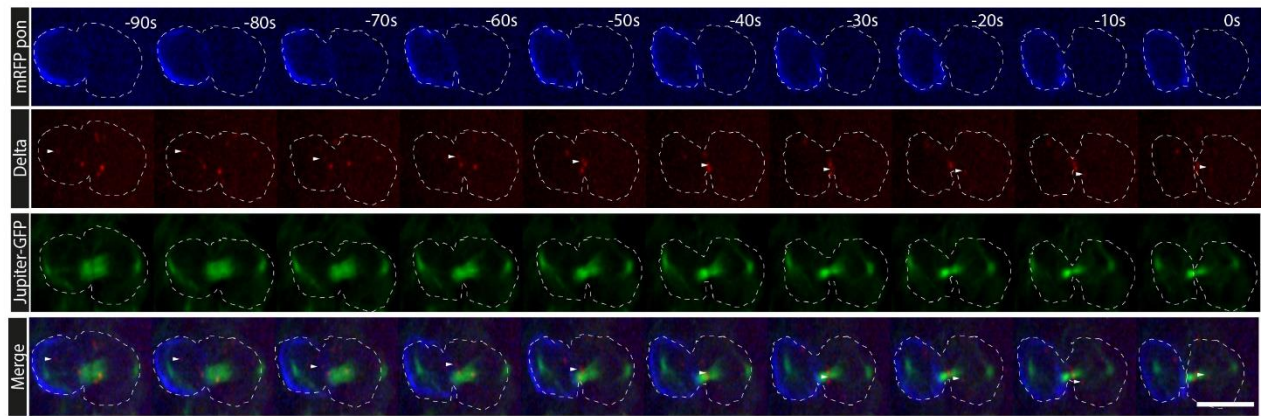
To follow the segregation of endosomes containing endocytosed Delta, I used a previously described antibody uptake assay (Loubéry and González-Gaitán, 2014). Anti-Delta antibody, conjugated to Alexa647, was endocytosed during a 5 min pulse and followed till 40 min. During this duration, the antibody exists in early endosomes (Coumailleau et al., 2009). To improve detection of fluorescent anti-Delta antibodies in endosomes and limit photobleaching during imaging, I used state-of-the-art back-illuminated sCMOS camera (95B, Photometrics), with improved sensitivity and quantum yield, instead of the EMCCDs used previously (Derivery et al., 2015) (See also section 2.2. Imaging in methods, page 49). I reconfirmed that endosomes containing endocytosed Delta indeed segregate asymmetrically during SOP

division (Coumailleau et al., 2009; Derivery et al., 2015). To specifically identify SOPs in the developing notum, I used the membrane binding domain of Pon (Partner of Numb)-RFP, that faithfully marks the anterior pIIb cells (Lu et al., 1999). Between 10 to 40 minutes post chase, endosomes containing endocytosed Delta exhibited strong bias towards pIIa segregation, validating previous reports (Derivery et al., 2015; Loubéry and González-Gaitán, 2014; Loubéry et al., 2014) (Fig 6A). This pool of endocytosed cargo reflects early endosomes (Coumailleau et al., 2009). The spindle, marked by Jupiter-GFP, also showed a strong asymmetry: MT density at the pIIb side was on average 26% higher compared to pIIa (Fig 6A and 6D for n=18 spindles).

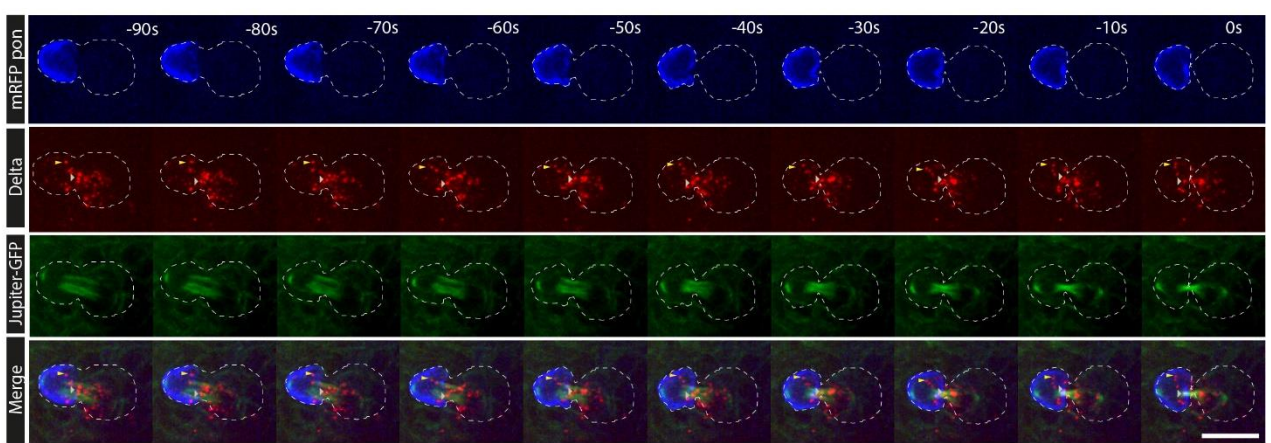
Surprisingly, when the above assay was performed but with a longer chase period (>50 min), Delta endosomes (late Delta) showed a strikingly different pattern of segregation. The bias towards pIIa dispatch was sharply reduced appearing almost symmetric (Fig 6B). Endosomes targeted to the spindle, with approximately similar kinetics, frequently moved towards the pIIb side. I verified that the spindle asymmetry remains unchanged in these cells (Fig 6D), indicative of proper polarisation, with a strong pIIb enrichment of MT density (mean pIIb MT enrichment was 33% for n=18 spindles). I tracked the endosomes using our (developed with Dr. Emmanuel Derivery) automated endosome tracking algorithm (see methods). Compared to early endosomes, pIIa enrichment was dramatically reduced for late endosomes (Fig 6C). Therefore, although the spindle asymmetry is unchanged, even marginally increased at this stage, late endosomes containing endocytosed Delta can traffic symmetrically on central spindle MTs.

The behaviour of late endosomes establishes that some compartments are indeed able to bypass central spindle asymmetry. This suggests an altered motor recruitment to these endosomes and/or presumably a different vesicle identity. Although these endosomes are Delta positive, they may now reflect either late, recycling, or TGN/Golgi related endosomes. Therefore, guided by the late delta experiment, I set out to study Rab4 (recycling pathway), Rab6 (golgi) and Rab7 (late/degradation pathway) to determine the molecular identity of these symmetrically sorting endosomes.

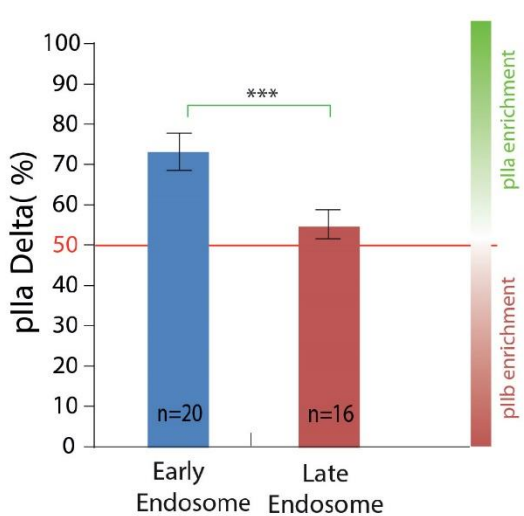
A



B



C



D

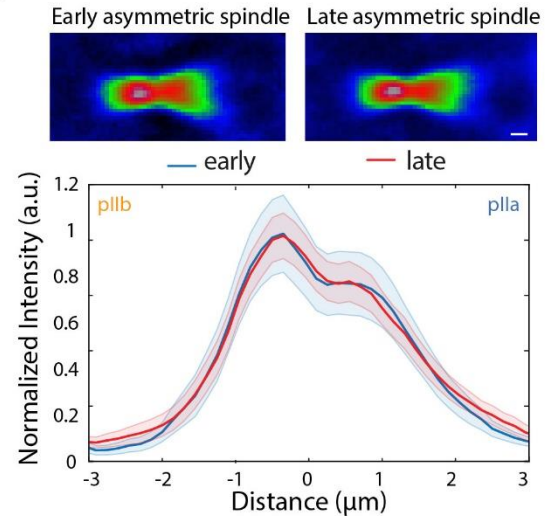


**Fig 6. Late Delta endosomes partition symmetrically.** (A) Early Delta endosomes (between 10 to 40 min post chase) are asymmetrically targeted to posterior pIIa cell (Pon marks the anterior pIIb cell, white arrowhead shows biased segregation to pIIa). The spindle is asymmetric with higher MT density on the pIIb side. (n= 20 cells) (B) Late Delta endosomes (post 50 min chase) partition symmetrically. Not all endosomes however are targeted to the spindle (yellow arrowhead), while some (grey arrowhead) move from the spindle to pIIb. The spindle remains robustly asymmetric during this time. (n=16 cells) (C) Endosome dispatch for early and late endosomes in SOPs. (D) Upper panel, Average spindle at two time points, indicating higher tubulin density in pIIb side. Lower panel, line scan quantification of upper panel. Error bars represent SEM. Students t-test,  $p < 0.001$ . Scale bar 10  $\mu\text{m}$

---

### Rab7 marks sara endosomes

Rab7 is a bona-fide marker of late endocytic compartments (Chavrier et al., 1990; Wichmann et al., 1992). Previous reports suggest that Rab7 segregates symmetrically during SOP division, though the mechanism of segregation is unknown (Coumailleau et al., 2009; Emery et al., 2005). I confirmed that while endogenous Rab7 segregates symmetrically (Fig 7A), Rab7 also co-localises with endosomes containing endocytosed Delta (Fig 7C left panel). Importantly, not all Rab7 positive compartments are targeted to the equatorial region during division suggesting a functional distinction amongst late endosomes (Fig 7A, arrowhead pointing to an endosome not targeted to the spindle). However, the spindle-targeted fraction of Rab7 endosomes follow Delta and is dispatched preferentially to pIIa.

Previous reports using both over-expression, endogenous tagging and antibody staining suggests Delta containing endosomes are a subset of Rab5-positive multi-vesicular endosomes (Coumailleau et al., 2009). I reconfirmed this by imaging Rab5-GFP vesicles under the same conditions (Fig 7B). Delta containing endosomes co-localised extensively with Rab5 vesicles (Fig 7C, Right panel).

Co-localisation of Delta containing endosomes with both Rab5 and Rab7 endosomes, bona-fide markers of early and late endosomes respectively, suggest that during division Rab5 and Rab7 might occupy the same endocytic vesicle (Bucci et al., 1992; Chavrier et al., 1990; Gorvel et al., 1991; Rink et al., 2005). Co-localisation of bona fide markers of early and late endosomes

may reflect a randomisation event in the endocytic pathway, leading to loss of distinct vesicle identity during mitosis. If distinctive vesicle identity is lost during division, markers of other population of endosomes, recycling and Golgi-derived for instance, would also be expected to co-localise with delta endosomes.

### **Golgi-derived vesicles and fast recycling endosomes are independent of Delta endosomes**

I studied the distribution of fast recycling endosome marker Rab4 (McCaffrey et al., 2001) and Golgi-resident Rab6 (Echard et al., 1998; Short et al., 2002) (Fig 8).

Both these markers are weak and bleach rapidly. For Rab6, I could detect targeting to the equatorial zone during division (Fig 8A, arrowhead). Rab6 does not co-localise with Sara containing endosomes extensively. The weak fluorescence, and homogenous expression throughout the notum currently precludes any analysis of segregation (Fig 8A).

For Rab4, I could not detect any fluorescence in dividing SOPs despite repeated trials, although I could detect endosomes in neighbouring epithelial cells (Fig 8B). This may suggest that during division, recycling compartments are either lost rapidly or reorganises into tiny vesicles beyond current imaging capabilities. In all cells, Delta was asymmetrically dispatched into pIIa.

Taken together, this *in vivo* analysis suggests existence of compartments that segregate symmetrically during SOP division despite the presence of a strong asymmetric spindle. Future work will now focus on narrowing the identity of these symmetric compartments, as well as their motor equipment (see discussion).

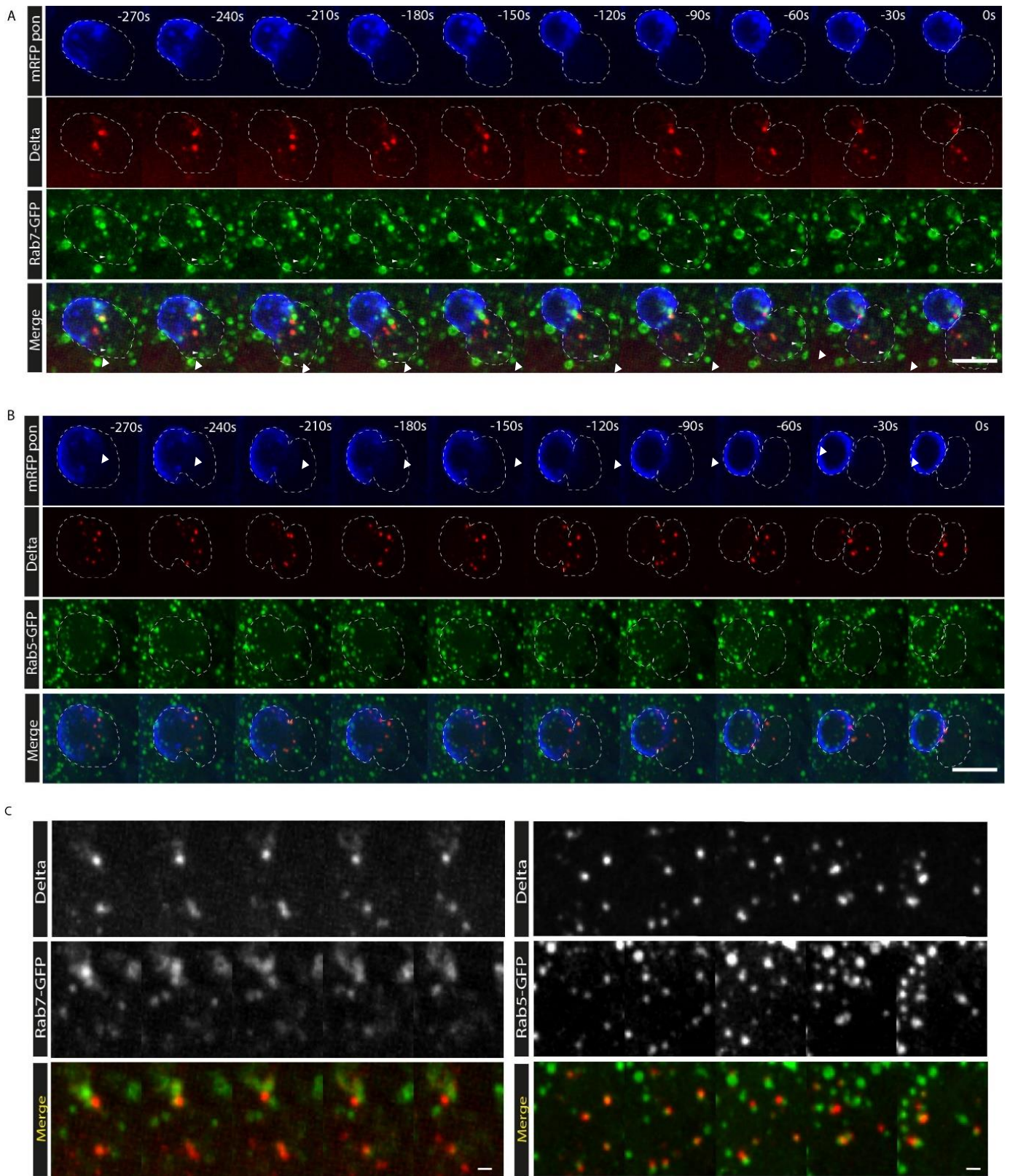
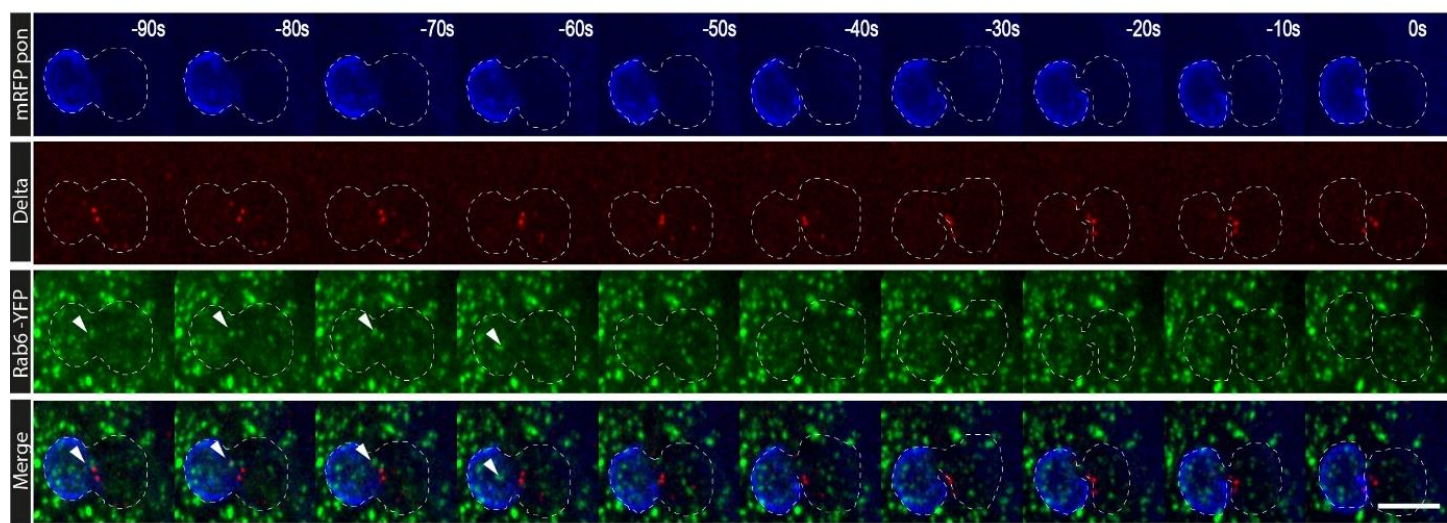


**Fig 7. Rab 7 co-localises and follows delta segregation.** (A) Rab7-GFP vesicles during SOP division. The distribution of Rab 7 is symmetric overall. Note a fraction of Rab7 vesicles is not targeted to the spindle (white arrowhead) (Images are representative of n=16 cells) B) Rab5-GFP vesicles during SOP division. Scale Bar 10  $\mu$ m. (C) Rab7 and Rab 5 co-localises with delta containing endosomes.(Images are representative of n=11 cells) Note that in both cases a fraction of Rab vesicles do not co-localise with delta. Scale bar 2 $\mu$ m.

A



B

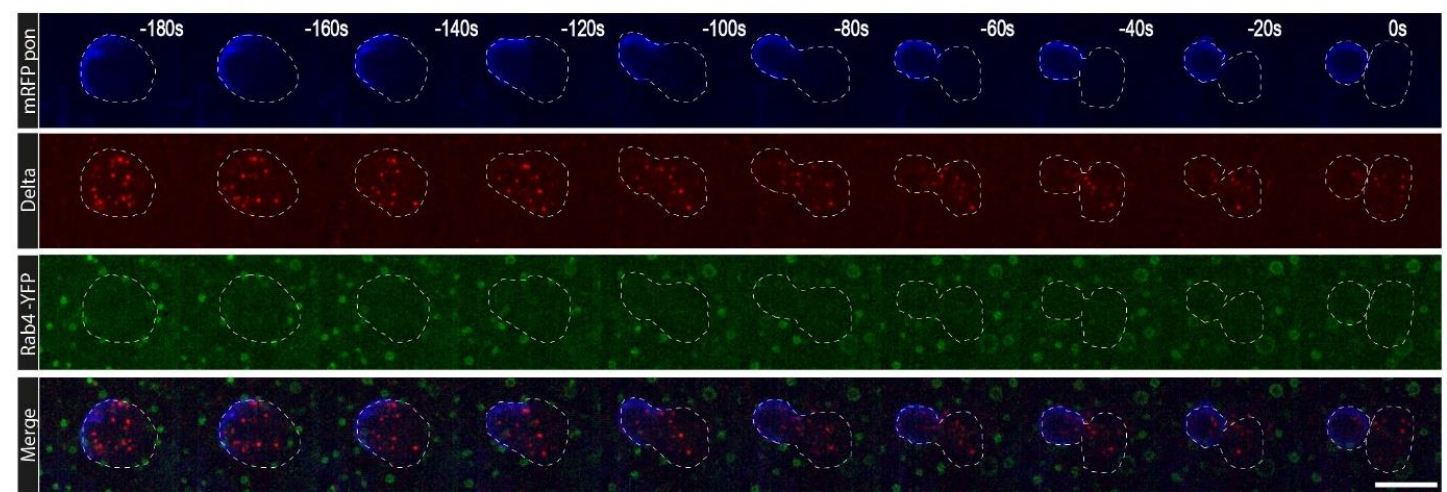


**Fig 8. Rab 6 and Rab 4 show distinct behaviour during division.** (A). Rab6-YFP is targeted to the equatorial region (white arrowhead) but does not co-localise with delta containing endosomes and moves towards pIIb. (Images are representative of n=12 cells) (B) Rab4 vesicles in dividing Sops. On the contrary to neighbouring epithelial cells (Pon-negative), Rab4 endosomes could not be detected during SOP division. (Images are representative of n=14 cells) Scale bar 10  $\mu$ m.

## **Summary**

During SOP division, the asymmetric central spindle directs asymmetric segregation of Sara endosomes (Derivery et al., 2015). Despite the presence of an asymmetric spindle, other cargoes might require symmetric partitioning.

Using anti-delta antibody, I made the remarkable observation that late (>50min chase period) delta containing endosomes segregate asymmetrically between the two daughter cells. This indicates that these endosomes contain a machinery to bypass the asymmetry of the track. How this occurs is presently unknown.

Despite my best efforts I could not detect any Rab protein colocalising exclusively with the late Delta endosomes, though some degree of colocalization was seen with both Rab5 and Rab7. The expression pattern of Rabs, throughout the notum precluded me from doing any intensive tracking analysis. Future work will focus on alleviating this problem (See global discussion)

# Chapter 4

The microtubule (MT) cytoskeleton plays a critical role in positioning and distribution of organelles and vesicles (van Bergeijk et al., 2016). Depending on nucleation sites, crosslinking and bundling, MTs can form networks spanning a wide variety of configurations from radial arrays to linear bundles depending on the cell type and conditions (Burute and Kapitein, 2019). Furthermore, during division, the various MT networks reorganise to form a single, orderly, bipolar spindle around chromosomes (Kapoor, 2017). The central spindle, formed in the wake of chromosome segregation during late anaphase, is a bipolar structure consisting of antiparallel bundled MTs and serves as a signalling platform for cytokinesis (Glotzer, 2009). In addition to its contribution in organising later events of mitosis, recent evidence suggests a distinct role of central spindle in polarised endosome trafficking during asymmetric cell division (Derivery et al., 2015).

A wide range of MT-associated proteins (MAPs) and molecular motors localise to and organise the central spindle (Glotzer, 2009). Although a wealth of information exists on their temporal regulation, contribution of any of these several hundreds of proteins individually to the network is difficult to determine. Furthermore, how the central spindle MTs contribute structurally as opposed to functioning as signalling hubs is a complex question to untangle.

One approach to answering this complexity lies in adopting a reductionist view of reconstituting a central spindle-like structure *in vitro* with minimum necessary components. With few components, reconstituted systems offer the advantage of directly testing the effect of individual proteins on the overall network. In the past, MT reconstitution systems with purified components have relied on either self-organisation of MT networks in solution or random surface attachments of MTs to study functions of individual MAPs and motors (Hannabuss et al., 2019; Kapitein et al., 2005). In these studies, rearrangement of MT networks in solution, under the influence of MAPs and motors, occur with unrestricted degrees of freedom which is unlikely to be recapitulated *in vivo* where MTs are often anchored and constrained by molecular crowding. In addition, a recent series of studies of MT organisation in fission yeast illustrates the importance of shape and geometrical confinements thereof in organising MT architecture (Chang and Martin, 2009). This vital realisation has led to an increasing number of reconstitution studies focusing on confinements *in vitro* with reconstituted networks that are often enveloped in a droplets or microwells imitating the cell

boundary (Miyazaki et al., 2015; Pinot et al., 2009; Suzuki et al., 2017). Furthermore, confinement imposed by MT nucleation has recently been recapitulated by micropatterning MT growth sites (Portran et al., 2013).

Micropatterning is the process of depositing molecules in a spatially controlled manner on a substrate (Blin, 2021). For biological applications, a common approach is to use subtractive micropatterning. Subtractive micropatterning offers a convenient approach to protein printing on a substrate coated with a repellent agent such as polyethylene glycol (PEG) or its modified versions. The repellent substrate is removed from the substrate by deep UV illumination (between 254 to 193 nm) through photomasks, creating regions amenable to protein adsorption (Azioune et al., 2010). This technology has been successfully applied in investigating properties of cytoskeletal polymers and MTs in particular (Aumeier et al., 2016; Portran et al., 2013; Triclin et al., 2021). Although convenient and applicable broadly, this method suffers from the limitation of manufacturing costly individual photomasks for every pattern. Further, producing protein gradients and multiplexing protein patterns are notoriously tedious.

Instead of photomasks, using a digital micromirror device (DMD), composed of an array of micromirrors, each permitted a finite degree of rotation, allows for a much greater flexibility in controlling the illumination pattern. Coupled with the use of DMD, photobleaching of chemically modified biotin has resulted in creating complex gradient patterns successfully and even multiplexing patterns with limited success (Bélisle et al., 2009). One limitation of this process is creating chemically modified (Flourescin conjugated) proteins for each unique pattern.

Replacing photobleaching by use of a photosensitiser and regular UV illumination culminated in development of a pioneering technique termed Light Induced Molecular Adsorption (LIMAP), offering vastly improved flexibility in pattern designing (Strale et al., 2016). This commercially available set-up uses a dedicated microscope with a photo-initiator and increases the ease and applicability of micropatterning.

The ability to print proteins in any geometry of choice opens the exciting possibility of reconstituting cytoskeleton landscapes of desired shape and size by printing cytoskeleton regulators without relying on self-organisation of these polymers (Blin, 2021). However, these prospects have been curtailed by large variances in micropatterning efficiencies of different proteins and problems in maintaining activity of patterned proteins.

In this chapter I describe improvements made to patterning efficiency by coupling an anchor that patterns with high homogeneity and selectivity to a given protein of interest. This markedly improves the efficiency and reproducibility of patterns. I show that these improved patterns can nucleate numerous MTs, making them ideal to recapitulate crowded, confined, MT networks. I further test the ability of Ase1p, a passive MT bundler, to bind and reorganise these networks with the goal of reconstituting a central spindle-like MT architecture.

## Results

### Fibrinogen anchors offer high efficiency of micropatterning

For the reconstitution assay, I required a convenient and reproducible way to micropattern MT seeds as nucleation sites and visualise the dynamics of MTs growing out from them by TIRF imaging. We (me along with Dr. Joeseph Watson and Dr. Emmanuel Derivery) combined DMD based micropatterning and TIRF microscopy into a single integrated custom-built setup (Fig 9A) where patterns produced on the DMD were projected through the backport of a commercial inverted microscope to the objective plane while simultaneously allowing for TIRF visualisation (See methods for details). Each mirror of the DMD array is capable of individually oscillating between +12° and -12°, generating a multitude of shapes of different sizes, as well as gradients. Using custom-codes (developed by Dr. Emmanuel Derivery) user-defined patterns can be displayed on the DMD through compatible image analysis platforms (ImageJ or Adobe Illustrator). This integrated streamlined system dramatically accelerates data acquisition by minimizing sample movement between micropatterning and subsequent imaging.

The central spindle is a bipolar structure with MT emanating from either side of the equatorial overlap. The fundamental advantage of using micropatterning to reconstitute MT networks lies in the control of MT attachment to the surface provided by the method, reducing chances of random MT nucleation. Such selective micropatterning requires using a strong anti-fouling agent to coat coverslips. I adopted a protocol developed in the lab of Manuel Thery to silanize clean-room grade cleaned glass coverslips with methoxy-PEG-silane (Portran et al., 2013). Silanisation rapidly improves the passivating quality of PEG moiety, severely limiting any stochastic MT attachment to the surface.

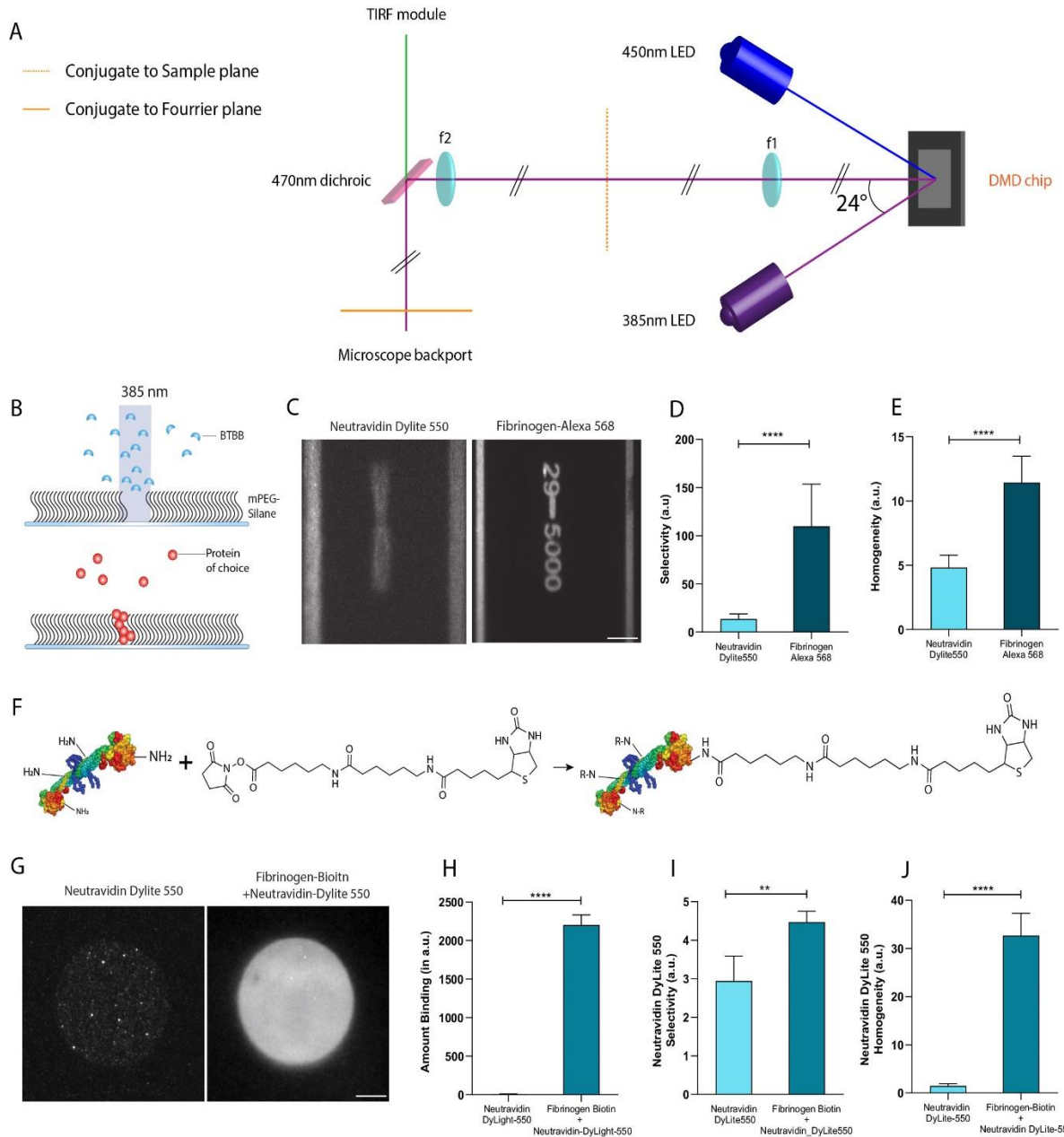


**Fig 9. Fibrinogen-Biotin anchor improves micropatterning efficiency of Neutravidin.**

(A) a 385nm LED was used to illuminate a DMD chip at 24° (corresponding to double the deflecting angle). The DMD was positioned in a 4f system ( $f_1=f_2=125\text{mm}$ ) with respect to the backport of the microscope (conjugate to DMD plane). A 470nm dichroic placed after  $f_2$  lens combines TIRF illumination with LED illumination. For optogenetic purposes a 450 nm LED is also incorporated in the set-up (B) mPEG-silane coated coverslips were UV illuminated in the presence of BBTB. This resulted in selective removal of the mPEG-silane layer, allowing protein adsorption. After washing out BBTB, the protein of choice was added to generate specified patterns. (C) Neutravidin Dylite 550 (50  $\mu\text{g/ml}$ ) or Fibrinogen-Alexa546 (50  $\mu\text{g/ml}$ ) was micropatterned by LIMAP and imaged by TIRF (D-E) Pattern selectivity and homogeneity

were compared for Neutravidin Dylite 550 (n=8) and Fibrinogen Alexa 546 (n=7) for the images shown in C. Statistics were performed by student t-test. p<0.001. (F). The free amino groups of Fibrinogen react with NHS-biotin yielding Fibrinogen-Biotin conjugate. (G) Neutravidin Dylite 550 (at 50 µg/ml) alone was micropatterned as in C. Alternatively, Fibrinogen-biotin (at 20 µg/ml) was used as an anchor followed by Neutravidin addition at identical conditions. (H-J) Amount of protein bound, selectivity and Homogeneity were measure for Neutravidin Dylite 550 alone (n=6) or Fibrinogen-Biotin conjugated Neutravidin Dylite 550 (n=7). Statistics were performed by Mann-Whitney test for H and J (p <0.001). Students t-test was used to analyse graphs in I (p<0.01). Scale bar 10 µm. Error bars represent SEM. Aside from (B) and (C) all other figures were adapted from (Watson et al., 2021)

---

To make this repellent surface amenable to MT attachment we (me along with Dr. Joeseph Watson and Dr. Emmanuel Derivery) used regular UV (390nm; compatible with microscope objectives lenses) in conjunction with a photo-initiator, 4-benzoylbenzyl-trimethylammonium bromide (BBTB), synthesized in-house (in collaboration with Benjami Oller-Salvia; see methods for detailed synthesis) (Fig 9B). UV patterns displayed on the DMD were projected onto the mPEG-silane coated coverslip using the custom-built optical set-up. UV illumination of the BBTB-filled coverslip results in selective removal of the passivating PEG layer. After removal of the remaining BBTB from the solution, a protein of interest is added for efficient patterning. To quantitatively describe the quality of micropatterns in my experiments, I measured two important parameters of generated patterns- a) Selectivity, which measures the pattern contrast (that is the amount of protein in the patterned region compared to a neighbouring non-patterned region in the same field of view) and b) Homogeneity, which is measure of variance within the patterned region. Along with these two standard parameters, I measured a third metric, the amount of protein patterned, where the same protein is used as a read-out for different patterning approaches. As a test for, I patterned Fibrinogen, a complex charged glycoprotein previously known to pattern efficiently (Azioune et al., 2010) (Fig 9C, right panel). As reported previously, Fibrinogen (conjugated to Alexa 546) patterned with satisfactory contrast and homogeneity, validating the patterning pipeline. I proceeded to pattern Neutravidin as an essential first step to pattern biotinylated MT seeds eventually. However, in contrast to Fibrinogen, Neutravidin (conjugated to DyLite550) patterns poorly (Fig 9C, left panel) with low selectivity and homogeneity (Fig 9D-E).

Since the assay relied heavily upon reproducible microtubule patterning to a sufficiently high density to mimic central spindle architecture, I investigated the possibility of dramatically improving protein micropatterning, focussing particularly on Neutravidin. As mentioned above, Fibrinogen patterns with high homogeneity and selectivity. We (this idea was developed in conjunction with Dr. Joeseph Watson and Dr. Emmanuel Derivery) thus explored the possibility of conjugating biotin to Fibrinogen to create an “anchor” that efficiently captures Neutravidin. Fibrinogen is a large complex glycoprotein with exposed amine groups that make it suitable for chemical conjugation. I reacted molar excess of commercially available NHS (N-HydroxySuccinamide) modified biotin with Fibrinogen in alkaline buffer condition to yield Fibrinogen-biotin (Fig 9F), separated from excess NHS-biotin by desalting (Zebaspin, ThermoFisher). I tested the ability of fresh Fibrinogen-biotin to micropattern and recruit Neutravidin (Fig 9G). As compared to Neutravidin Dilyte550 alone, Fibrinogen-biotin recruited almost 20-fold more Neutravidin to the pattern (Fig 9H). This was accompanied by a concomitant increase in selectivity (Fig 9I) and homogeneity (Fig 9J). Together these results indicate a remarkable improvement in the ability to pattern Neutravidin by use of a Fibrinogen anchor.

Since Neutravidin is a tetrameric molecule capable of simultaneously binding to four biotin entities, I examined the ability of Neutravidin, patterned either directly or indirectly through Fibrinogen-biotin, to bind biotinylated substrates. I used biotinylated bovine serum albumin (BSA-Biotin) conjugated to Alexa647 (developed by Dr. Joeseph Watson) as an indicator for biotin binding by patterned Neutravidin. As seen in Fig 10A, Neutravidin patterned through Fibrinogen-biotin binds BSA-Bioitn-Alexa647 (Fig 10A, right panel) with improved efficiency compared to directly patterned Neutravidin (Fig 10A, left panel). The amount of BSA-biotin recruited to the Neutravidin patterned through Fibrinogen-Biotin increases almost 50-fold as compared to the same by Neutravidin alone (Fig 10B). In addition, Fibrinogen-Biotin anchor improves both selectivity (Fig 10C) and homogeneity (Fig 10D) of the micropattern by almost 3-fold. I ensured that BSA-biotin binding is through specific interaction with Neutravidin as opposed to non-specific binding to the patterned region. Consequently, patterned Fibrinogen-biotin alone, without addition of Neutravidin, does not appreciably recruit the biotinylated target (Fig. 10A, middle panel). When I compared the patterning efficiency of labelled Neutravidin, Neutravidin-Dylite 550, only a modest improvement was seen (Fig 10B-D). By all parameters- amount of target BSA-biotin recruited, pattern selectivity and homogeneity, Neutravidin-Dylite550 patterned through the Fibrinogen-biotin anchor does not appreciably

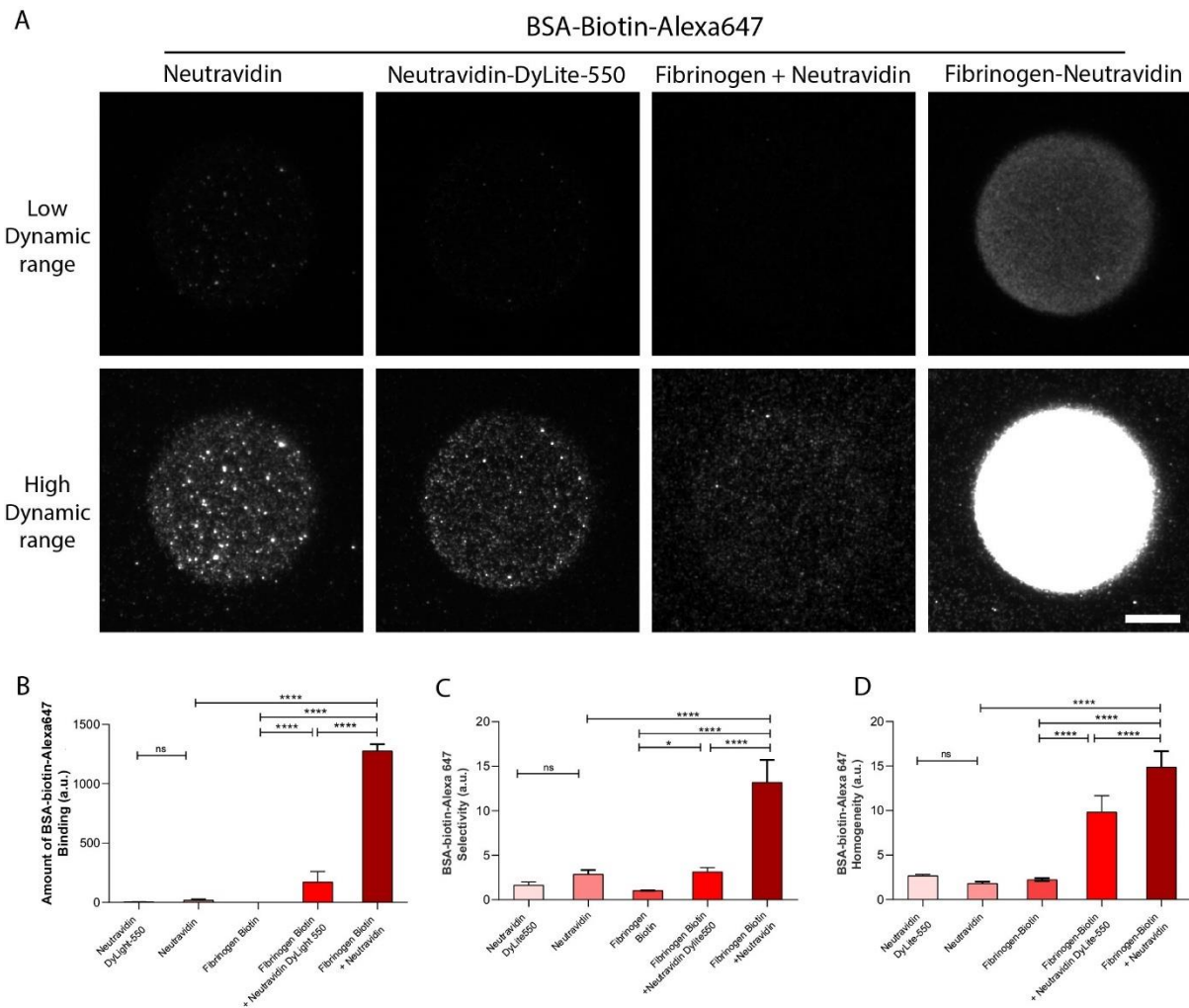


**Fig 10. Biotin binding of patterned Neutravidin is improved by Fibrinogen Anchors**

(A) Micropatterned Neutravidin, Neutravidin Dylite 550 ( $50 \mu\text{g/ml}$ ) either alone or patterned through Fibrinogen-biotin ( $20 \mu\text{g/ml}$ ) at the same concentration under identical conditions were tested for their ability to bind BSA-biotin-Alexa647 ( $5 \mu\text{g/ml}$ ). As a control, Fibrinogen-biotin alone was also tested for the same. Images were acquired by TIRF under two separate exposures so that all images in a lane could be represented with the same dynamic range. (B-D) Quantification of the amount of BSA-biotin-Alexa647 bound (B), Selectivity of BSA-biotin-Alexa647 binding (C) and Homogeneity (D) for Neutravidin alone ( $n=8$ ), Neutravidin-Dylite550 alone ( $n=7$ ), Fibrinogen-biotin alone ( $n=5$ ), Neutravidin patterned through Fibrinogen-biotin ( $n=5$ ) and Neutravidin Dylite 550 patterned through Fibrinogen-biotin ( $n=5$ ). Log<sub>10</sub> transformed data were analysed by One way ANOVA followed by a Turkey post hoc test ( $p < 0.001$ ). Error bars represent SEM. Figures were adapted from (Watson et al., 2021).

improve its ability to bind biotinylated targets in contrast to unlabelled Neutravidin. This likely represents a partial loss of biotin binding capability of the Neutravidin tetramer upon labelling. Together this data represents a remarkable improvement in micropatterning efficiency of active, “biotin-binding” Neutravidin by using compatible Fibrinogen anchors.

### **Improved micropatterning of MTs**

I used the improved micropatterning approach to print short stable MTs in reproducible shapes, forming the required nucleation zone for reconstitution of a central spindle (Fig 11A). I used mPEG-Silane, previously described to act as a strong passivating agent for MTs, coated coverslips and used the previously described improved LIMAP approach for micropatterning (Watson et al., 2021). I bound short, double stabilised GMPCPP-taxol MTs to the patterned region by using Neutravidin, patterned through Fibrinogen-Biotin as described above. To reduce non-specific binding of MTs, mPEG-silane layer was further passivated with PLL-PEG (poly-L-lysine fused to PEG). Finally, tubulin polymerisation was initiated by introducing soluble tubulin at 12  $\mu$ M to the chamber at 37°C. As shown in Fig 11B, this approach results in strong, specific deposition of GMPCPP-MT seeds to the patterned region with high contrast (Fig 12B, left panel). When tubulin polymerisation is ensued, numerous MTs grow out specifically from the patterned region (Fig 11B, right panel). I measured the polymerisation speed of MTs from patterned seeds (Fig 11C). Speeds typically clustered around two central values, with a 4-fold difference between them. Comparatively fast-growing ends of MTs were denoted plus ends and slower growing ends were denoted minus ends.

As the central spindle is a bipolar structure, with plus ends from either side forming rigid antiparallel overlaps, I asked whether MTs grew from the patterns with their plus ends outward. I measured the polymerisation speed of all growing MTs from a fixed pattern and ascribed them to be plus or minus ends by comparing their velocities. On average, 79% of the MTs growing out from the pattern had their plus end pointed outwards, consistent with previous observations (Fig 11D). MTs which had their plus ends emerging outward from the pattern were much longer due to their higher polymerisation speeds and would presumably constitute the bulk of overlaps formed from MTs from opposing patterns.

An advantage of MT patterning using the LIMAP approach is the ability to control the density of MT seeds. This is achieved by controlling the intensity of UV illumination though the DMD device. Lower the intensity of the UV illumination, lower the amount of protein bound to the pattern.

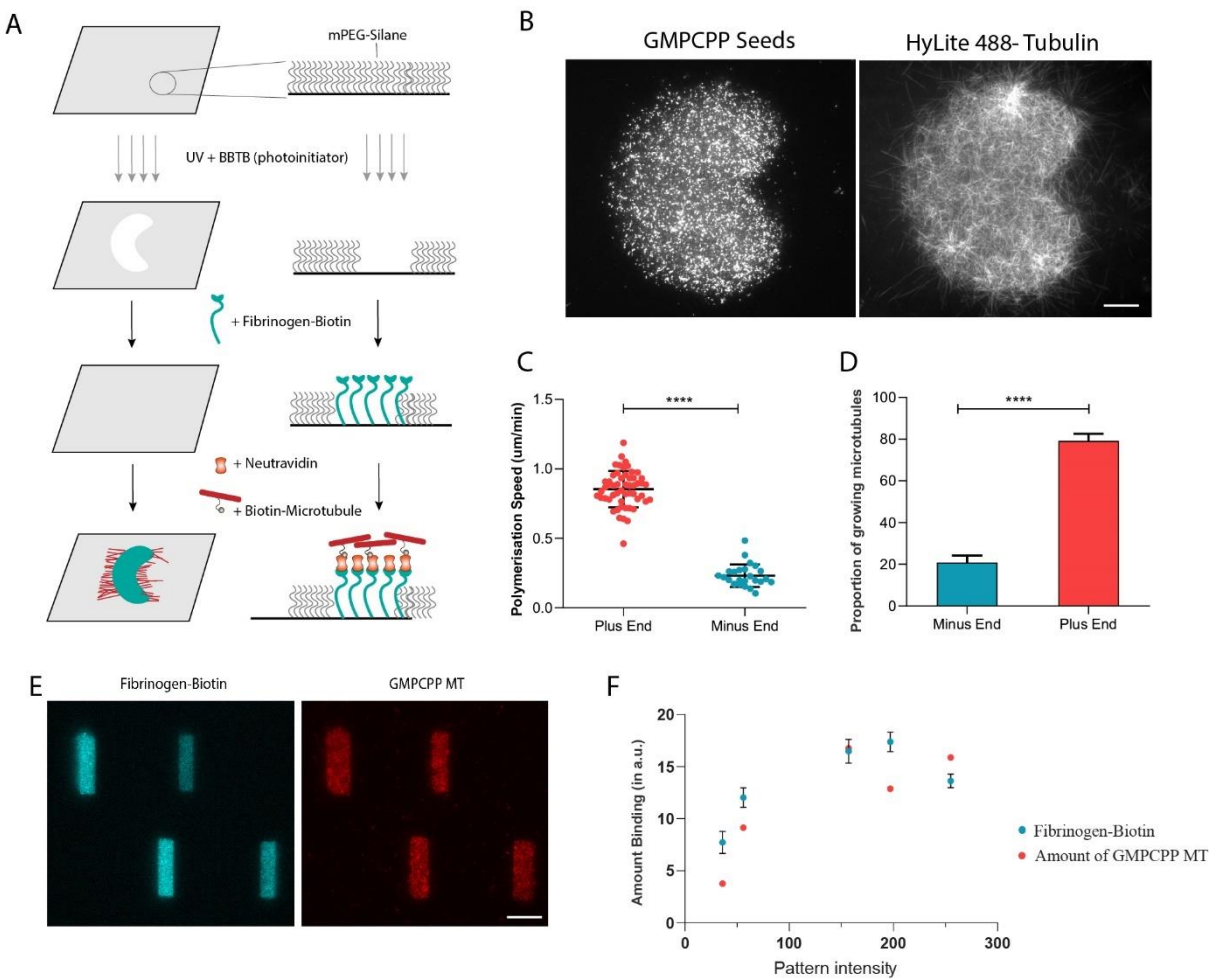


**Fig 11. Fibrinogen anchors lead to robust micropatterning of MTs**

(A) Passivated coverslips were micropatterned with UV and BBTB as photo-initiator. Following selective depletion of the passivating layer, Fibrinogen-biotin (20  $\mu$ g/ml) was allowed to bind. After washing off excess Fibrinogen-biotin, Neutravidin was added at 100  $\mu$ g/ml. Coverslips were quenched further and short GMPCPP stabilised MTs were added to bind to the Neutravidin. (B) Rhodamine labelled GMPCPP seeds were seen to selectively bind to micropatterned region at high density (Left). MTs grew from these regions after addition of HyLite488-tubulin at 12  $\mu$ M at 37°C. (C) Quantification of polymerisation speed of MTs growing out of the patterns. Speeds higher than 0.45um/sec were designated as Plus ends ( $n=54$ ) with mean speed  $0.854 \pm 0.12$  um/min. Minus ends ( $n=25$ ) grew at a mean speed of  $0.2313 \pm 0.08$  um/min. Students t-test.  $p<0.0001$ (D) Quantification of the proportion of MT ends growing outward from each pattern. All MTs growing from ten micropatterns were analysed to determine the proportion of plus and minus ends ( $n=10$ ).  $79.17 \pm 2.1$  % of all MTs were plus ends. Students t-test.  $p<0.0001$ . Error bars represent SD. (E) Gradients of patterned Fibrinogen -Biotin and MT seeds. Gradients were created by varying the intensity of DMD illumination (F) Quantification of gradients showing that amount of Fibrinogen-biotin ( $n=3$ ) and attached MT seeds ( $n=1$ ) could be varied by changing the intensity of the DMD pattern ( $n=3$ ). Scale bar 10  $\mu$ m.

As shown in Fig 11E, the Fibrinogen-Biotin anchor can be deposited in differing amounts and is able recruit similarly differing amounts of MT seeds (quantified in Fig 11F). The ability to micropattern different amount of MT seeds would allow for reconstituting asymmetric MT density of the central spindle (Derivery et al., 2015).

### **Ase1 forms long bundles MT networks**

Next, I asked how the nature of the emerging MT network changed under the influence of MAPs. PRC1 is the principle organiser of central spindle architecture, specifically the distinguishing antiparallel bundle of MTs in late anaphase (Molinari et al., 2002; Subramanian et al., 2010). Previously, the fission yeast homolog of PRC1, Ase1p, was used to reconstitute a spindle-like MT network (Portran et al., 2013). Ase1p contains a C-terminal MT binding domain and a short N-terminal dimerization domain (Fig 12A). I purified recombinant GFP-Ase1p (~100 KDa) (Fig 12B) that migrated as a single entity during gel filtration (Fig 12B). I tested whether the purified protein could efficiently bind and bundle MTs. For this purpose, I used stable GMPCPP MTs. At 10 nM, GFP-Ase1p could efficiently bind MTs with a six-fold higher affinity for regions of MT overlaps (Fig 12D). Ase1p was indeed able to bind to MT overlaps. Two MTs formed an initial short overlap marked by GFP-Ase1p (Fig 12F, upper panel, 0sec). Eventually, these contacts became increasingly aligned and Ase1p marked the increasing overlaps (Fig 12F, white line). This suggests that purified GFP-Ase1p binds MTs and marks regions of MT overlaps.

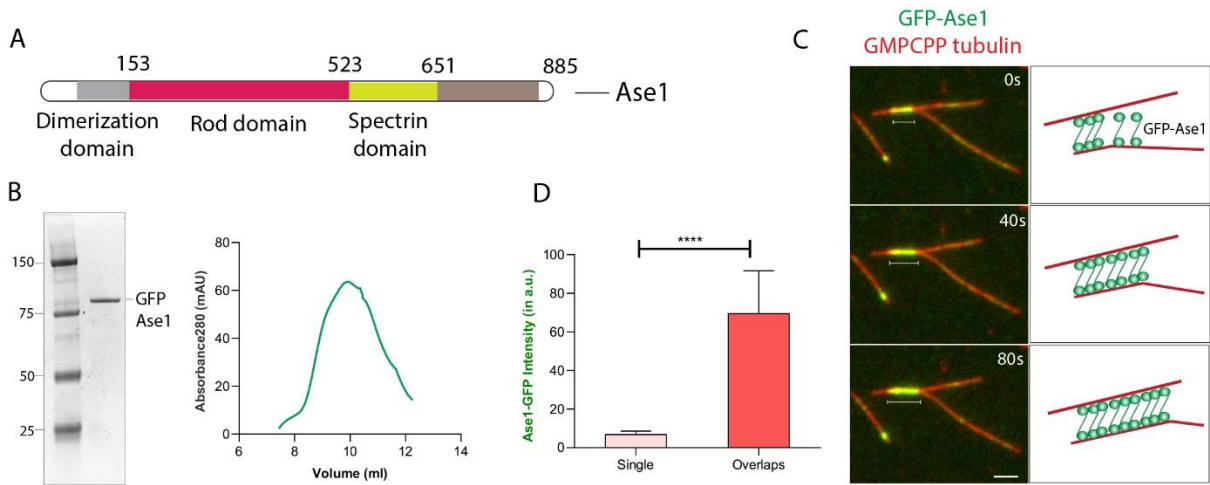


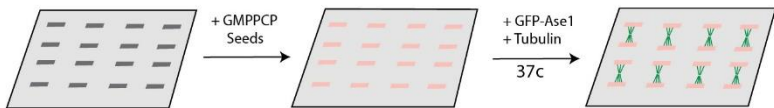
**Fig 12. Recombinant Ase1 bundles and aligns MTs.** (A) Domain organisation of Fission yeast Ase1. The spectrin domain (524-651) and C-terminal regions domain (652-885) mediate MT binding (She et al., 2019). (B-C) Purification of GFP-Ase1 (~100kDa) (C) Left, GFP-Ase1p bound and bundled MTs. Two MTs bundled by Ase1p aligned with each other over time (~80s), increasing the overlap length (white line). The green intensity at the bottom left corner is likely an artifact and probably does not represent a true binding event. Right, schematic of the bundling event with increasing overlap length and alignment. (D) Ase1 intensity was quantified for single ( $n=31$ ) and overlap MTs ( $n=47$ ). Students t-test with Welch correction.  $p<0.001$ . Error bars represent SD. Scale bar 2  $\mu$ m

Given Ase1's role in central spindle organisation I wondered if I could reconstitute a central spindle-like MT network using the improved micropatterning assay. I micropatterned Neutravidin, using Fibrinogen-Biotin as mentioned before, in short separate bars and attached short biotinylated GMPCPP seeds at 1  $\mu$ M. Tubulin polymerisation was triggered by 12  $\mu$ M rhodamine tubulin along with 10 nM GFP-Ase1p (Fig 13A). Initially, GFP-Ase1p localised to the seeds as MTs began to grow out of these seeds (Fig 13B, upper panel, 0sec). MTs soon encountered each other from opposing patterns and were efficiently bundled by Ase1p as marked by a strong accumulation of GFP (Fig 13B, middle panel, 500 sec). After MTs encounter each other, they continued growing along each other's lattice and the overlap spanned the entire distance between the nucleation zones. Concomitantly, I observed strong accumulation of GFP-Ase1p, along the entire lattice of the bundle (Fig 13B, middle panel, 1000sec). Surprisingly I also observed similar accumulation of GFP-Ase1p on bundles formed by MTs emerging from the same pattern, rather than patterned bars on the opposite side. These

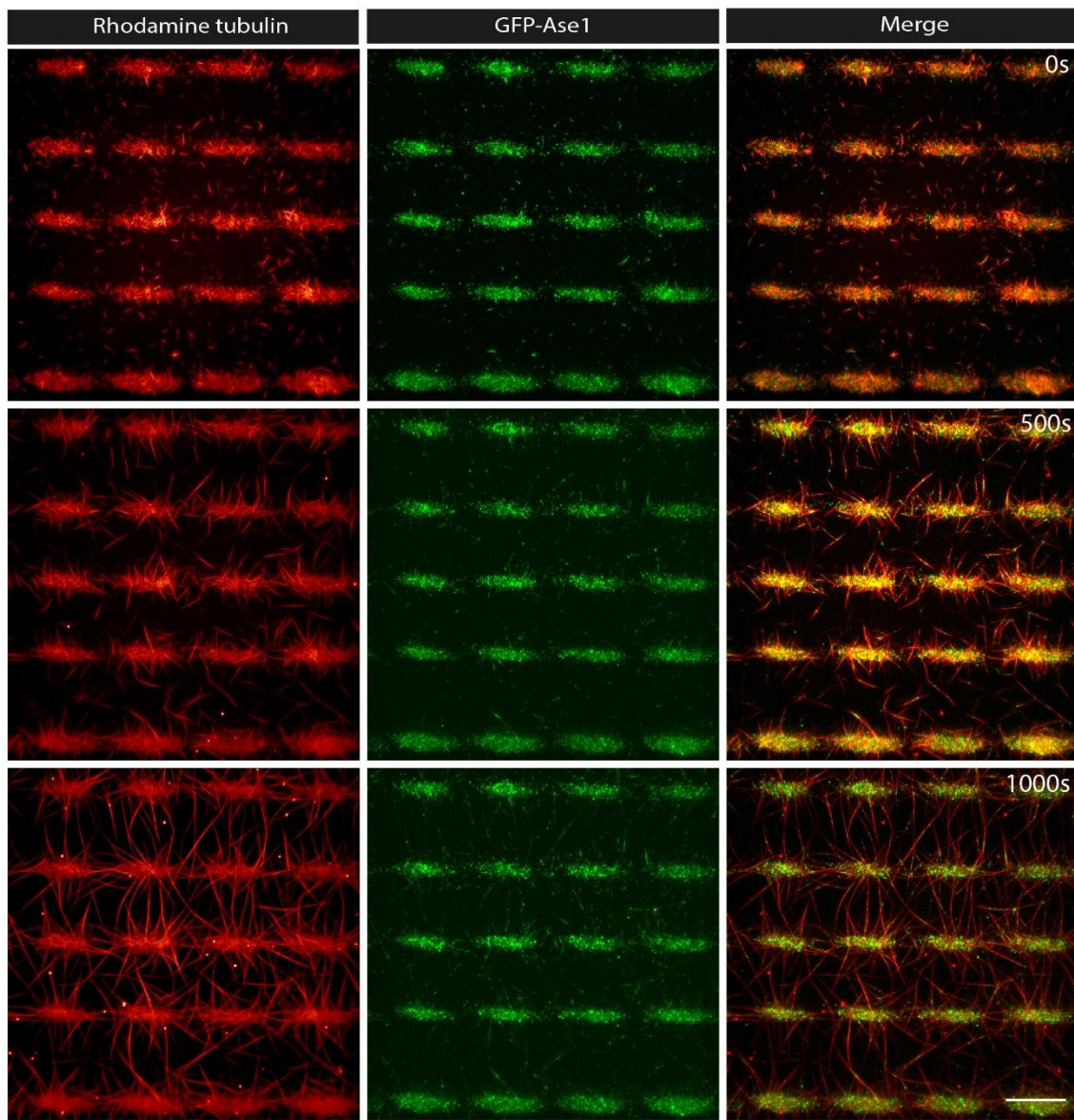
presumably represented parallel MTs. Together binding of Ase1p to both parallel and antiparallel overlaps of MTs resulted in a MT network composed of separate, large MT bundles bridging the entire length between MT seed micropatterns.

The PRC1 family of MT bundlers were reported to be specific to antiparallel overlaps. I was therefore surprised by the presence of Ase1p in all MT bundles during the assay, some of them presumably parallel contacts. I therefore asked whether Ase1p can effectively distinguish between parallel and antiparallel contacts. Since the crowded nature of the micropatterning assay makes it difficult to interpret polarity of overlaps, particularly near the nucleation region, I used random, sparsely surface attached seeds for this assay. When grown in presence of Ase1p, stochastic contacts between growing MTs were always marked by the presence of GFP-Ase1p (Fig 13C), regardless of their orientation (data not shown for parallel contacts). Kymograph analysis revealed that similar to patterning assay, MTs continued growing after their contact (Fig 13D) with concomitant recruitment of GFP-Ase1p. I observed only a modest, though significant, selectivity of Ase1p binding to antiparallel contacts. The lack of any marked selectivity between parallel and antiparallel contacts likely explains the appearance of large bundles in the micropatterning assay and a lack of polarity sorting in the final MT network. Therefore, while micropatterning works to get to the right polarity and the right density, a passive antiparallel bundler like Ase1 is not suited to reach the goal of reconstituting a central spindle-like structure.

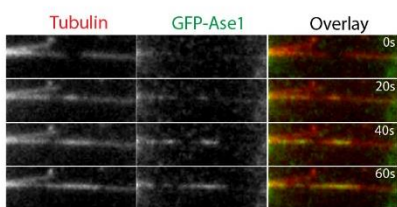
A



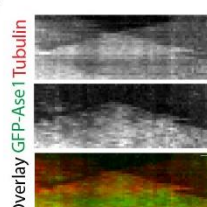
B



C



D



E

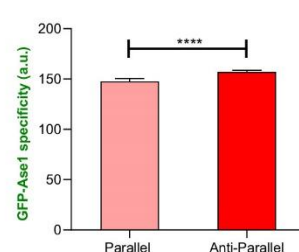


**Fig 13. Ase1 forms bundled MT network of mixed polarity** (A) Schematic of the micropatterning assay. GMPCPP stabilised short seeds were attached to short micropatterned bars through Neutravidin (anchored via Fibrinogen-biotin) at 1 $\mu$ M. Micropatterned seeds were elongated by addition of tubulin at 12  $\mu$ M in BRB80 (For exact formulation of the buffer used, see methods). (B) Montage of MT network formation by GFP-Ase1p bundling of elongating MTs, visualised by TIRFM. Time interval 500 sec. Scale bar 10  $\mu$ m. Note that, at 1000s time point (bottom row), GFP-Ase1p is detected along all MT bundles. (C) GFP-Ase1p binding to antiparallel overlaps, growing from randomly surface attached seeds, were imaged at 20sec interval. Scale bar 1  $\mu$ m (D) Kymograph of growing overlaps indicate no significant change in growth velocity after overlap formation. Scale bar 5 sec vertical, 1  $\mu$ m horizontal (E) GFP-Ase1p specificity was measured by the amount of GFP-Ase1p bound to either for parallel (n=21) and antiparallel overlaps (n=18). Students t-test, p <0.0001. Errors bars represent SEM.

---

## Summary

Micropatterning is a powerful approach to study the effect of geometry on reconstituted systems. However, its application has been limited due to variability of protein patterning and loss of activity during the process. This is compounded by the fact that some proteins, like Neutravidin, inherently pattern poorly (Fig 9). Here I describe a general method of improving patterning efficiency by first patterning a compatible Fibrinogen anchor that patterns with remarkable selectivity, homogeneity and reproducibility. By using Fibrinogen as an anchor, this process bypasses the requirement of proteins to be patterned directly onto the coverslip, thereby ensuring their complete functionality. Although the results presented here is limited to improving biotin binding (Fig 10), the same approach has been adopted to improving a vast array of proteins, including GFP and concavalin A, in the lab (Watson et al., 2021). I expect that the technology presented here would find wide ranging applications in micropatterning.

With improved micropatterning strategy, I aimed to reconstitute a central spindle-like MT architecture. Using this approach, I could faithfully nucleate numerous MTs from a defined geometry of choice. The micropatterning method improves the density of MTs available for reconstitution. Importantly, this micropatterning approach allows me to have unprecedented

control over the density of MTs nucleated from the pattern (Fig 12). This is important in reconstituting asymmetric MT architectures, such as the asymmetric central spindle. The control over MT density allows me to test various conditions of differing levels of asymmetry.

MT network reconstitution attempts have so far been limited to self-organisation of MTs in solution (Hannabuss et al., 2019). While this approach is instructive in exploring roles of different MAPs and motors, either individually or in combination, in reorganising MT networks, effect of geometrical constraints on such networks remains unanswered. In particular, central spindle MTs are believed to branch out from existing kinetochore bound MTs, therefore limiting their degrees of movement. Recent encouraging advancements in this regard highlights the importance of geometry and MAPs in organising bipolar spindle like MT networks (Portran et al., 2013).

I used MT micropatterning assay to understand effect of MAPs in organising confined MT networks. Ase1p, acts as a principle central spindle organiser by virtue of its bundling activity. In my assay, I found that Ase1p alone is unable to distinguish between parallel and antiparallel overlaps, thereby generating large bundles of MTs. These bundles also grew unhindered, in contrast to the *in vivo* situation, where antiparallel overlaps have a defined, fixed overlap length (Glotzer, 2009). Overlaps of a particular length could be maintained by the action of molecular motors, sliding overlapping MTs apart (Vukušić and Tolić, 2021; Vukušić et al., 2021) (also reviewed in Introduction page 39). To achieve a polarity sorted, stable antiparallel overlap akin to the central spindle, I planned to use an active plus-end directed motor that localises to the late anaphase spindle and slides MTs apart. Going forward, I therefore used Pavarotti, a kinesin-6 motor that is crucial for central spindle assembly *in vivo* (Nislow et al., 1992).

# Chapter 5

Central spindle consists of robustly bundled, interdigitating MTs with defined sections of antiparallel overlaps (Glotzer, 2009). Although Ase1 alone bundles MTs in vitro (Janson et al., 2007), it does not offer substantial selectivity of either polarity (parallel vs antiparallel) or control of overlap length as seen previously (Chapter 4). MT sorting based on their polarity is a conserved property of directional motor proteins (Surrey et al., 2001). It is therefore tempting to speculate that an anaphase specific motor protein could be tasked with this critical function in cells. Although multiple motors with overlapping functions organise the spindle, spindle elongation during anaphase B is specifically orchestrated by plus end directed Kinesin-6 Klp9, in conjunction with Ase1 in fission yeast (Fu et al., 2009). In higher eukaryotes, Kinesin-6 exists as part of the Centralspindlin complex (Mishima et al., 2002). I therefore attempted to reconstitute a central spindle-like antiparallel bundled MT architecture by using *Drosophila* Centralspindlin complex in my micropatterning assay (described in Chapter 2)

## Results

### Preparation of active Centralspindlin complex

Centralspindlin exists as a stable, phospho-regulated hetero-tetrameric complex of a dimer of the kinesin-6, Pavarotti, and a dimer of Tumbleweed, a RacGAP, in flies (Adams et al., 1998; Mishima et al., 2004; Tao et al., 2016). In the absence of either subunit of the Centralspindlin complex, cells fail to form a bipolar central spindle and undergo cytokinesis. In *C.elegans*, the RacGAP component (CYK-4) is pivotal for correct localisation of its kinesin-6 counterpart, Zen-4 (Jantsch-Plunger et al., 2000). The Pavarotti subunit of *Drosophila* Centralspindlin complex consists of an amino-terminal motor domain of ~ 360 amino acids containing a nuclear localisation signal, followed by a short linker and coiled coil regions and a C-terminal globular domain (Figure 14A, upper panel). The RacGAP counterpart, Tumbleweed, is composed of an amino terminal coiled-coil region, a putative C1 domain and a C-terminal Rac GAP domain (Figure 14A, lower panel). The Rac GAP domain is critical for formation of an equatorial contractile ring by recruiting Rho GTPase Pebble (Nishimura and Yonemura, 2006). The C1 domain reportedly binds the ingressing plasma membrane during cytokinesis and maintains association between the membrane and the maturing midbody (Lekomtsev et al., 2012). Both these domains are dispensable for MT binding and organisation (Mishima et al., 2002). I therefore expressed a truncated version of Tumbleweed (Tum) of the first 120 amino acids

capable of binding to the motor, along with the full-length kinesin subunit, Pavarotti, tagged to GFP (Pav-GFP), from a single bicistronic vector in bacterial cells (Mishima, 2017) (see methods). Sequential two-step affinity purification, first by GST (on Tumbleweed) and the by PC tag (on Pav-GFP), yielded pure recombinant Tumbleweed and Pavarotti (Fig 14B, right panel) that co-migrated as a single complex during gel filtration (Fig 14B, left panel).

To investigate whether purified Centalspindlin complex was active, that is whether it could bind and move MTs, I performed an in vitro gliding assay. Pav-GFP was tethered to passivated glass surface by anti-GFP nanobody (GBP), followed by addition of stabilised GMPPCP MTs (Fig 14C, upper panel). MTs started moving immediately, albeit slowly. By kymograph analysis, the average speed of MT translocation was determined at 72 nm/sec (n=46). Although modest compared to other cargo-carrying motors of kinesin-1 or kinesin-3 families that move in excess of ~600nm/sec, this is in agreement with similar reports of Kinesin-6 movement in fission yeast and *C.elegans* (Davies et al., 2015; Fu et al., 2009). I observed only a negligible effect of the Centalspindlin complex on tubulin polymerisation dynamics (Fig 14D). The ability to bind and move MTs suggests that purified recombinant Centalspindlin complex is indeed active in vitro.

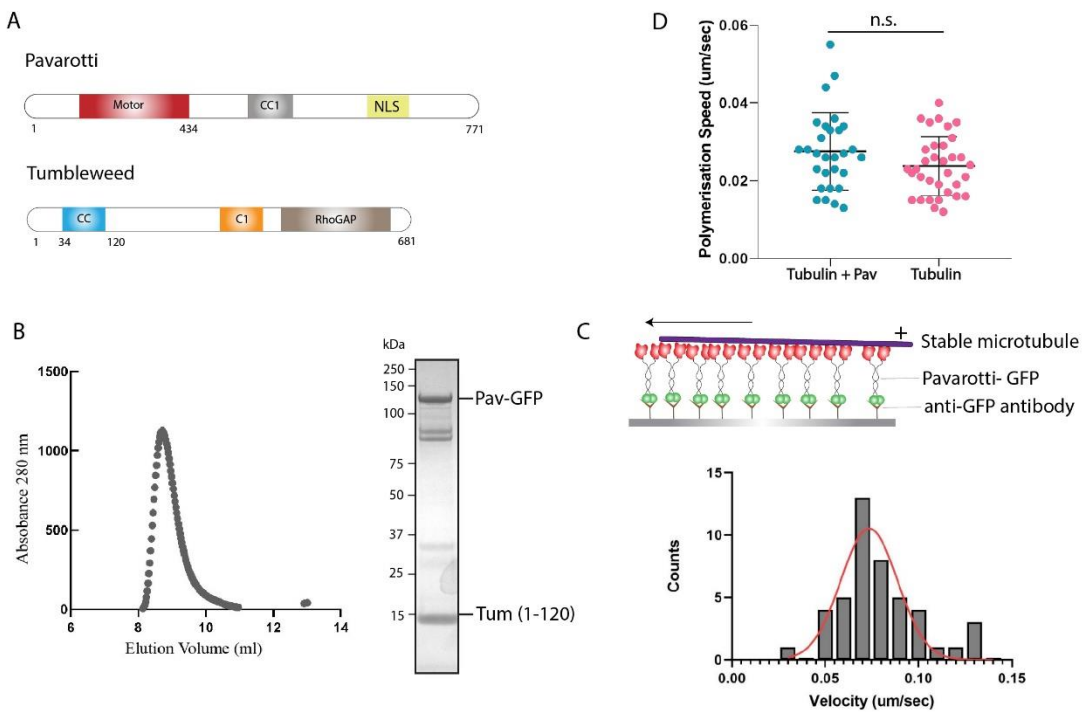


**Fig 14. Preparation of active Centalspindlin complex** (A) Domain organisation of Pavarotti (Pav) and Tumbleweed. Note, the first 120 amino acids of Tumbleweed is capable of binding to Pav. (B) Purification of the Centalspindlin complex. Pav-GFP (~127 KDa) and Tum (~15 KDa) comigrates as one peak during gel filtration. (C) upper panel, schematic showing gliding assay used to determine Centalspindlin activity. Pav-GFP (at 100 nM) was attached to a passivated coverslip by anti-GFP antibody and GMPCPP stabilised MTs were added at 0.03  $\mu$ M in motility buffer containing 75mM KCl and 50mM Glutamate. Lower panel, gliding velocities were measured for continuous directional movements of MTs. Mean speed  $72 \pm 15$  nm/sec (n=43). (D) Polymerisation speeds were measured for MTs growing from stable seeds with 12  $\mu$ M tubulin either in presence or absence of 20 nM Pav-GFP. Students t-test, n.s. indicates non-significant. Error bars represent SD.

### Pavarotti accumulates as clusters at MT tip

During these gliding assays, I occasionally observed clusters of GFP that accumulated at the end of moving MTs forming a cap. Previously, it was suggested that clusters of Centralspindlin could accumulate on long astral MTs and could represent an important mode of Centralspindlin accumulation at the equatorial zone (Hutterer et al., 2009). I investigated whether in vitro, Centralspindlin indeed clustered at the plus end of MTs forming “end caps”. To investigate this, I immobilised stable MTs on passivated surface on the coverslip and added 10 nM of Pav-GFP. To establish whether formation of plus end caps were a conserved property of directional motor movement, I also performed the same assay with 10 nM of purified mammalian kinesin-1 (KIF5B) and *Drosophila* Klp3A, a KIF4A orthologue, that was previously reported to form similar end caps on MTs (Subramanian et al., 2013). In agreement with previous observations, I did not observe any substantial KIF5B-GFP accumulation along the lattice of MTs (Fig3A, upper panel). In contrast, Pav-GFP accumulated as bright clusters at the end of all MTs (Fig 15A, lower panel) similar to Klp3A (Fig 15A, middle panel).

How are end caps formed? One possibility is that end caps are a result of motile properties of Pavarotti and Klp3A motors. Upon landing on a MT, these motors could run till the plus end of the MT. At this point, instead of detaching, these motors remain attached, unable to take a step further causing a “traffic jam”. If true then longer MTs, by virtue of offering more landing sites for motors, would lead to more motors crowding at the MT termini. Consequently, longer MTs would be expected to have higher end cap intensity. Alternatively, if Pavarotti and Klp3A specifically recognise MT ends, then such length dependence would not be expected.

I systematically quantified the intensity of end caps (GFP accumulation at the end of MTs) as a function of MT length using a custom semi-automated script (see methods). As observed previously for mammalian KIF4A, *Drosophila* Klp3A, showed a linear relationship ( $R^2=0.603$ ) between end cap intensity and MT length (Fig 15C). This was matched by Pav-GFP (Fig 15C). Longer MTs (~15  $\mu\text{m}$ ) accumulated almost 3-fold more Pavarotti at its end than shorter MTs (~3  $\mu\text{m}$ ). I then compared the slope of linear trend between Klp3A and Pavarotti. Pavarotti appeared to have a significantly higher propensity for accumulation per unit length change of MT lattice than Klp3A (Fig 15D). These results suggest that Pavarotti can accumulate as clusters at the end of MTs and its intensity is proportionate to MT length.

End caps are formed by motors (Pavarotti and Klp3A) remaining attached at MT plus ends. Presumably, motor persistence at MT plus ends would lead to increasing end cap intensity over time. Do both these motors persist at the MT end to a similar extent?

To answer this, I automatically tracked each end-cluster over time (see Methods). A motor with reduced persistence at MT end would result in a slower increase in end cap intensity over time as motors would be more likely to leave from the MT end. For KIF5B, even after 50 sec I did not observe any significant accumulation along the MT lattice (Fig 16A). For Klp3A, within the same interval there was only a marginal increase in Klp3A-GFP intensity (Fig 16B). In contrast with Pavarotti-GFP, after 50sec there was a sharp and significant increase in GFP intensity at the tip (Fig 16C). Careful examination of this increase revealed a sharp linear increase ( $R^2=0.9734$ ) for Pavarotti-GFP compared to Klp3A-GFP ( $R^2=0.8696$ ). Comparison of the rate of accumulation confirmed that Pavarotti indeed accumulated rapidly compared to Klp3A (Fig 16E). For Pavarotti-GFP, I also observed a remarkable length dependent rate of accumulation. Per unit time, Pavarotti-GFP accumulated much faster on longer microtubules than on shorter MTs (Fig 16F). Because longer MTs also contain proportionately more intense end tags (Fig 16D), together they hint towards a cooperative binding model (see Discussion).

I have now established that Centralspindlin complex alone can form clusters at the plus end. These clusters possibly represent the propensity of motile tetrameric Centralspindlin to form higher order oligomers through C-terminal tail of Pavarotti, as reported for *C.elegans* Centralspindlin complex previously (Hutterer et al., 2009). Importantly, clustering also renders the motor subunit of the complex capable of engaging and sliding multiple MTs. Both formation of stable oligomers and sliding of MTs is crucial for polarity sorting and organisation of MT networks (Surrey et al., 2001). I therefore tested whether Centralspindlin complex can organise growing patterned MTs into polarity sorted antiparallel overlapped structure akin to the central spindle.

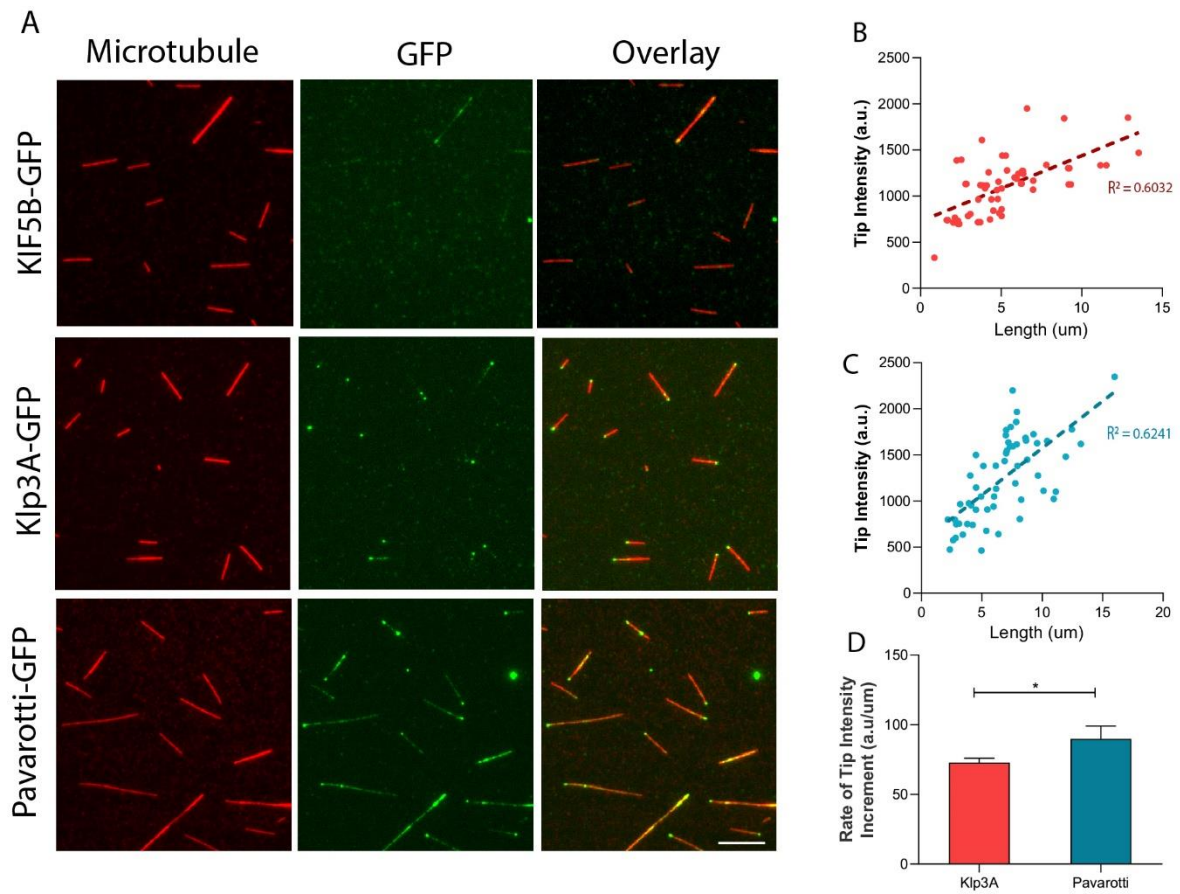


**Fig 15. Pav-GFP forms clusters at MT tips** (A) Kinesin enrichment on MTs were examined by TIRF microscopy. KIF5B-GFP, Klp3A -GFP and Pav-GFP at 10 nM were allowed to bind surface immobilised biotinylated GMPCPP stabilised rhodamine MTs for 5min. In contrast to KIF5B, Klp3A and Pav-GFP both form a cluster at MT end. For KIF5B, marginal GFP intensity on MTs indicates functional binding to MTs. (B-C) Tip intensity was analysed by 2-D gaussian fitting each GFP spot and along with corresponding MT lengths measured manually. n= 51 for Klp3A (B), n=57 for Pav-GFP (C). (D) Slope of graphs from (B and C) plotted for three separate each field view (n=3). Students t-test, p < 0.05. Error bars indicate SD.

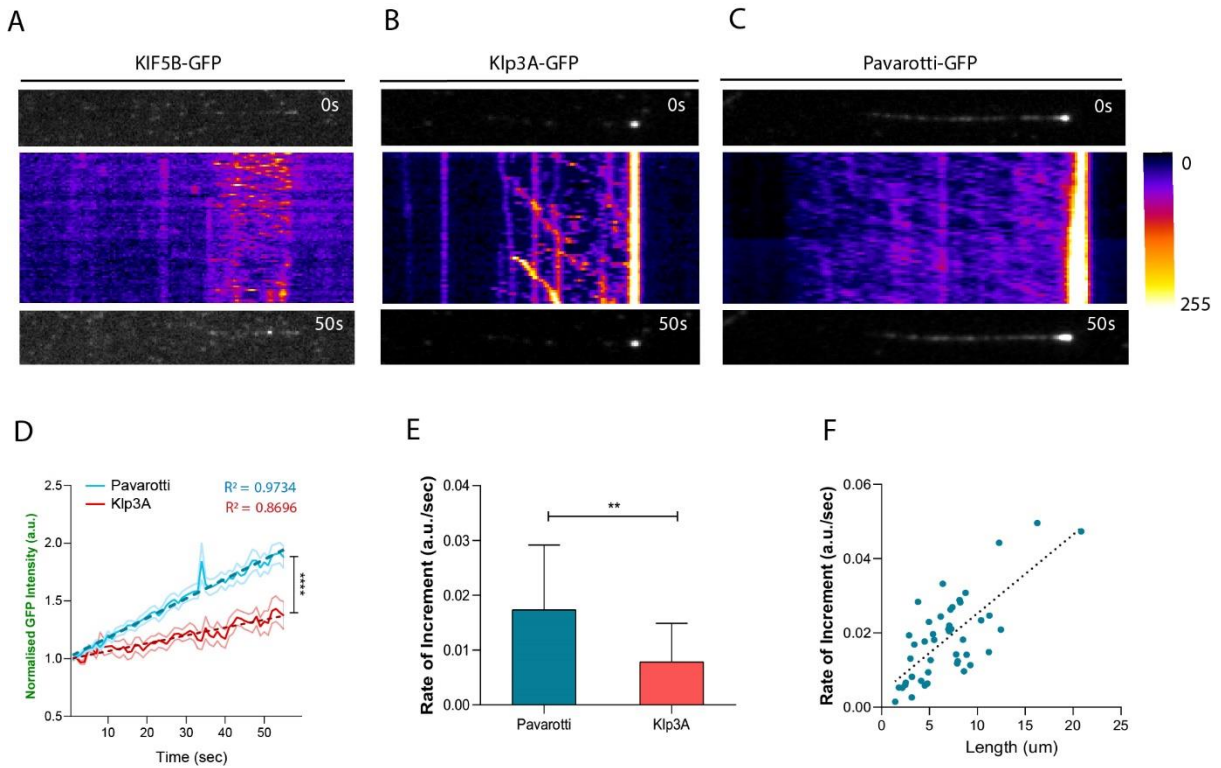


**Fig 16. Accumulation of tip intensity over time** (A-C) Kymograph of tip intensity for KIF5B (A), Klp3A-GFP (B) and Pav-GFP (C) on GMPCPP MTs. For each protein, single GFP channels were acquired by TIRF microscopy for 50 secs with 1sec frame interval to limit photobleaching. Tip intensity increases for Klp3A and Pav-GFP with no detectable KIF5B-GFP at MT tips. Blue to white represents progressively higher intensities. All images are displayed with the same dynamic range. (D) Quantification of tip intensity normalised to its value at time 0 sec. n= 83 for Klp3A, n=97 for Pav-GFP. Average profile of accumulating intensity was fitted to a linear regression line for both. At 10 nM motor concentration, tip intensity at the end of 50 sec was significantly higher for Pav-GFP (Students t-test with Welch correction,  $p < 0.001$ ). (E) Quantification of slopes of each linear fitted curve as in D, for four separate field of views (n=4). Students t-test.  $p < 0.01$ . Error bars indicate SD. (F) Quantification of slope from D with corresponding MT lengths measured manually for Pav-GFP (n= 39).

## Pavarotti induced changes in MT networks

To test whether Centralspindlin complex can organise growing MTs into antiparallel overlaps, I patterned short stabilised biotinylated MT seeds as described previously (see Methods; also, Chapter 4) on a mPEG-silane coated coverslip by a biotin-neutravidin sandwich. Tubulin polymerisation from these micropatterned MT seeds was initiated by introducing 13.5  $\mu$ M rhodamine tubulin along with 50 nM of Pavarotti-GFP in presence of 125 mM KCl at 37°C (Fig 17A). In agreement with previous results, I observed Pavarotti-GFP caps immediately at the plus tips of all polymerising MTs (Fig 17B, middle panel).

Growing MTs encountered each other outside the pattern and formed antiparallel overlaps (Fig 17B). Since the growing MTs are anchored at the pattern, sliding by Pavarotti-GFP in these overlaps would expectedly result in large scale filament buckling. Indeed, as illustrated in Fig 17C, growing MTs with Pavarotti-GFP at its plus tip encountered each other and first formed antiparallel contacts (Fig 17C, 30sec, white arrowhead). Soon after their initial encounter, these filaments began to slide against one another. Due to geometric constraints, this led to intense buckling of the pair (Figure 17C, 100sec, white arrow). As a result, MT pairs assumed strained, distorted conformations that continued to expand. Eventually, the strain was released by disengagement of the two MTs (Figure 17C, 120sec, white asterisks). Given the crowded nature of the network, freed MTs almost immediately formed antiparallel contacts with other neighbouring filaments (Figure 17C, 140sec) and underwent similar cycles of buckling, disengagement and filament switching (Figure 17C, 200 - 240sec, bottom row). As a measure of buckling, I measured the deflection of the MT pair ( $h$ ) from their initial position in presence of Pavarotti (Fig 17D, upper panel). Compared to control situations (images not shown) where bundles rarely underwent any major deflection after their encounter, addition of Pavarotti caused major deflections of MT bundles (Fig 17D, lower panel) till they eventually disengaged. Inevitably, this led to constantly evolving, unstable MT interactions within the network.

What happens to the Pavarotti end caps during the rapid and dynamic switching of MTs within the network? Do these end caps represent motile oligomeric entities? And if so, do they also undergo similar switching dynamics? I followed polymerising MTs along with their cognate Pavarotti-GFP tip cluster. I clearly observed two distinct modes of behaviour. Firstly, as MTs encountered each other, often at an angle along the lattice, entire Pavarotti clusters switched MTs and reached the plus tip of the new MT. In Fig 17E, a tip cluster of Pavarotti (yellow arrowhead), encounters a second MT and switches track.

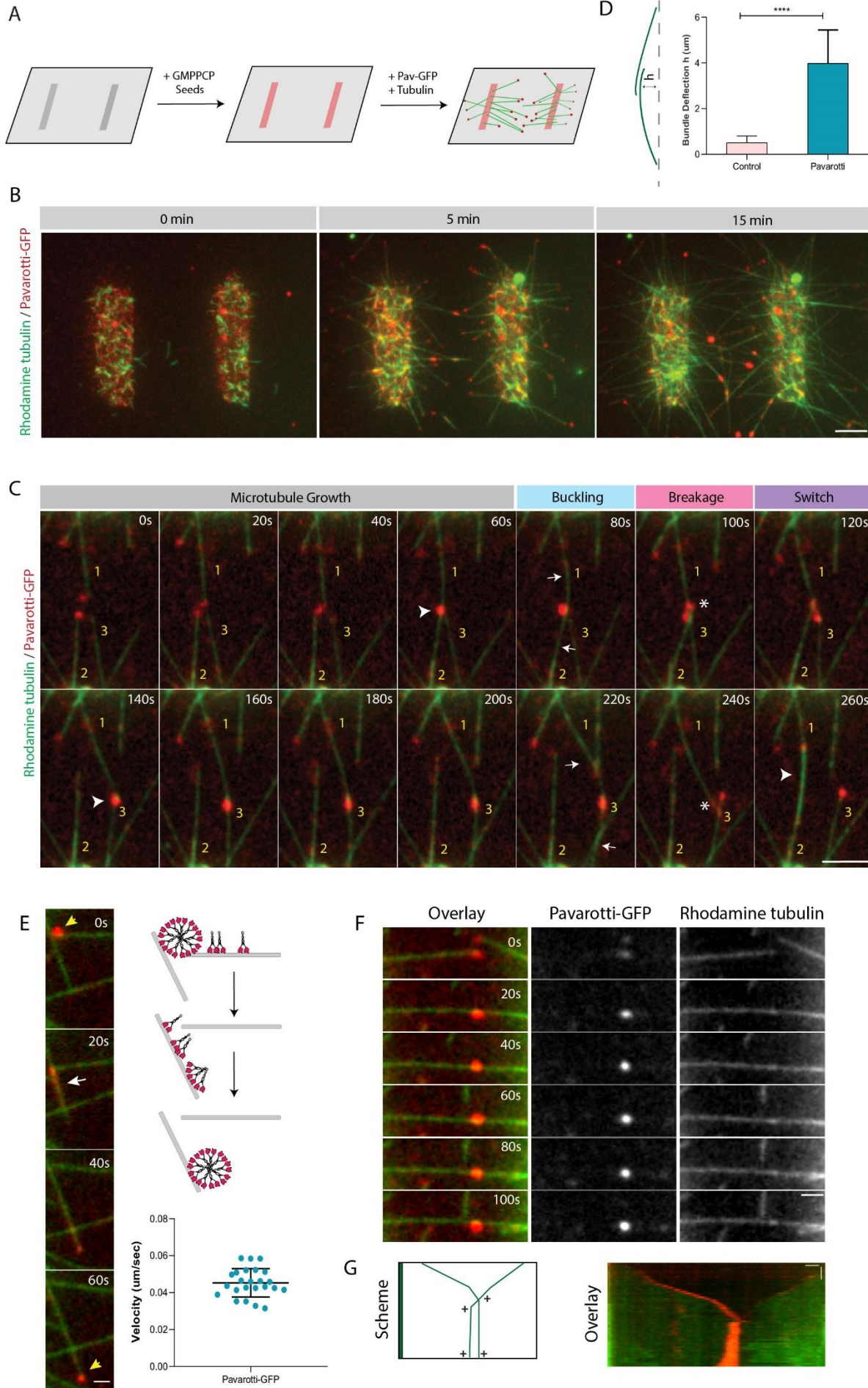


### **Fig 17. Pavarotti induced changes in MT network**

(A) Short GMPCPP seeds were micropatterned in short bars separated by 10  $\mu\text{m}$ . Pav-GFP was added at final concentration of 50 nM along with rhodamine tubulin at 13.5  $\mu\text{M}$ . (B) Snapshots of MT networks organised by Pav-GFP. Immediately following tubulin polymerisation (middle panel , 5min), almost all growing MT ends contained a bright Pav-GFP cluster. Growing MTs from either side form antiparallel contacts with occasional Pav-GFP enrichment (third panel, 15min). Scale bar 4  $\mu\text{m}$  (C) Time lapse images of MT behaviour in the network. MTs are numbered (in yellow) for descriptive purposes. Contacts/overlaps made between MTs is indicated by white arrowhead (t= 60 s and 120 s and 260s). MT buckling following contact is indicated with white arrows (t= 80 s and 220 s). Bundle disengagement is marked by white asterisks (t= 100 s and 240 s). Scale bar 5  $\mu\text{m}$ . (D) left, schematic representing MT bundle (in green) deflection from its initial position (dashed line). h, the distance between the maximum deflected point along the bundle with its initial position acts as a measure of bundle deflection. Right, quantification of bundle deflection for MT networks with (n=21) or without (n=26) Pavarotti. (E) Left, time lapse images showing Pav-GFP transfer at MT contacts. Initial and final position of the cluster is indicated by yellow arrows ( t=0 s and 60 s). White arrow (t= 20 s) indicates Pav-GFP flow along the newly contacted MT. Note appearance of Pav-GFP as a smear rather than a discrete spot. Scale bar 1  $\mu\text{m}$ . right upper panel, schematic of Pav-GFP (red motor heads) transport as clusters. Lower panel, velocity of Pav-GFP clusters (mean  $0.046 \pm 0.006 \mu\text{m/sec}$ . n=23). Error bars indicate SD (F) Stable contact between Pav-GFP tips. Time lapse images showing unchanging MT overlap length (right column) and Pav-GFP position (middle column). Scale bar 3  $\mu\text{m}$ . (G) left, scheme explaining the MT orientation as seen in the kymograph (right) generated from time lase images in (F). Scale bar horizontal 1  $\mu\text{m}$ , vertical 25 sec.

---

Thereafter, Pavarotti flows as a stream of motile entities (white arrowheads) towards the plus end (mean velocity  $0.045 \mu\text{m/sec}$ ) and accumulates as a cluster. Second, and far less frequent, were Pavarotti-clusters colliding against each other head-on. Such collisions lead to a persistent stand-off between the growing MTs without any detectable sliding or Pavarotti “hand-off” (Fig 17F). During this period, Pavarotti-clusters remained stationary and became more intense as more and more motile kinesins from either side joined the cluster. Kymograph analysis of this

interaction (Fig 17G) revealed that during such collisions, tubulin polymerisation paused without undergoing catastrophe, suggesting geometric constraints could affect rate of tubulin polymerisation and lead to stable overlap formation.

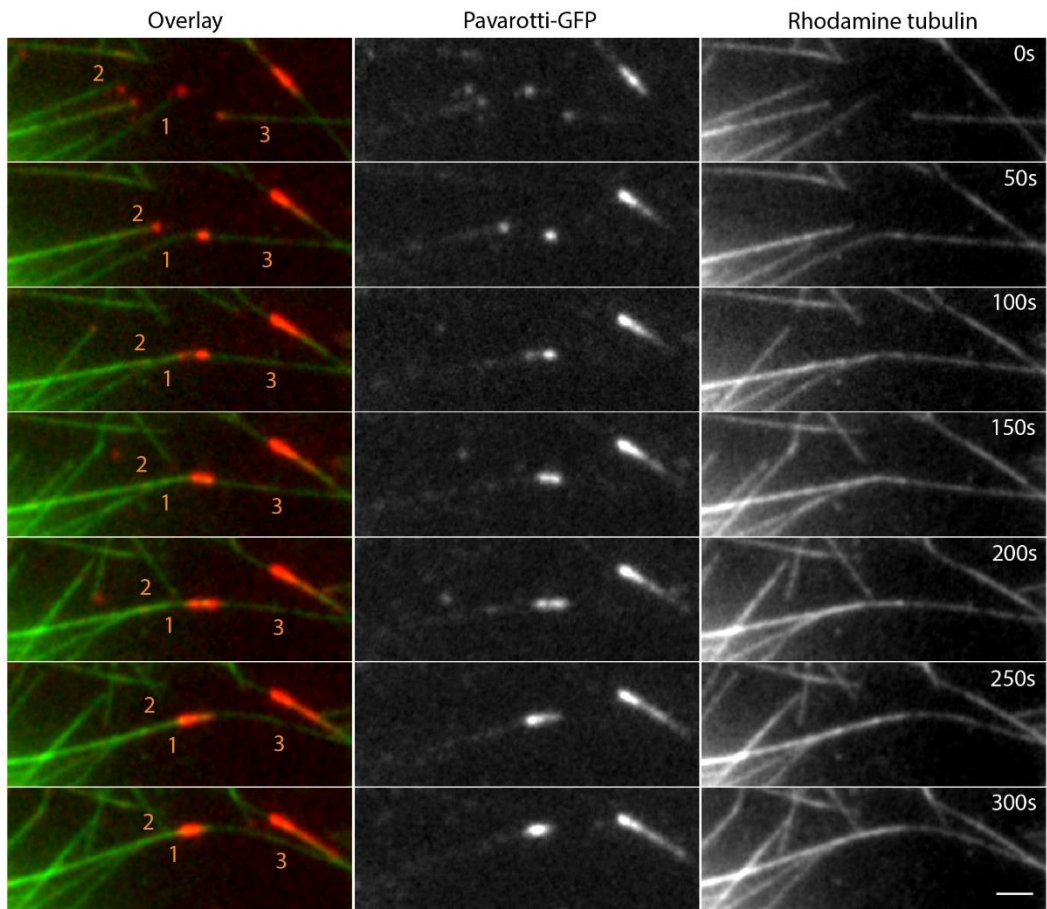
### Symmetric and Asymmetric overlaps organised by Pavarotti

Occasionally, MT pairs were also stabilised by contacting other MTs in the network, forming a bundle either symmetric or asymmetric. Fig 18A shows an example of an asymmetric bundle. Two polymerising MTs (1 and 3), emanating from patterns on either side, encounter each other with their opposing Pavarotti-GFP tip. This pair is soon joined by another MT (number 2) forming a three-filament asymmetric bundle ( $t=100\text{s}$ ). Over time, Pavarotti-GFP concentrates into a single cluster and induces small curvature in the bundle ( $t=300\text{s}$ ). Importantly, this bundle is remarkably stable and does not undergo further sliding or buckling.

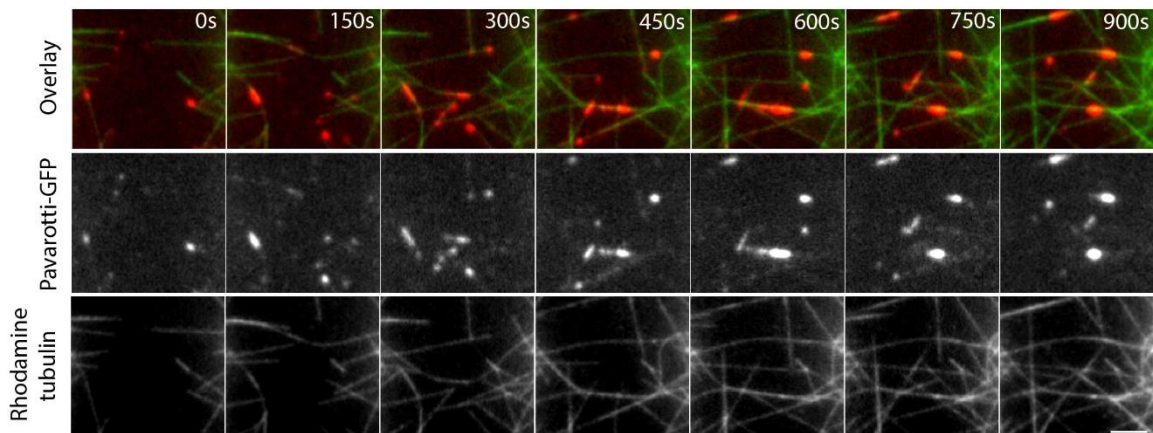
Similarly, symmetric bundles are formed by incorporation of MTs into an initial antiparallel microtubule pair. In the example showed in Fig 18B, MTs from either side meet each other and predictably undergo major deflections. However, other neighbouring MTs, joining the initial bundle from other side in antiparallel fashion, stabilises the bundle. As before, this four-filament symmetric antiparallel bundle remains stable during the course of the experiment with a tight cluster of Pavarotti-GFP. To estimate MT intensities on either side I measured both Rhodamine-tubulin and Pavarotti-GFP intensities across a three-pixel wide line along the overlap. For the asymmetric overlap I clearly detected a significant difference in tubulin intensities on either side of the Pavarotti cluster marking the overlap (Fig 18C). In contrast, for symmetric overlaps there was no marked difference in intensities (Fig 18D).

Together the data suggests MT bundles formed by more than two MTs could be occasionally stabilised as a bundle in contrast to previous examples of MT pairs buckling and breaking. Although the vast majority of MT encounters result in unstable cycles (Fig 17C), there are rare examples of stable overlaps, which can be either symmetric or asymmetric (Fig 18). To my knowledge this is the first instance of reconstituted asymmetric MT overlaps.

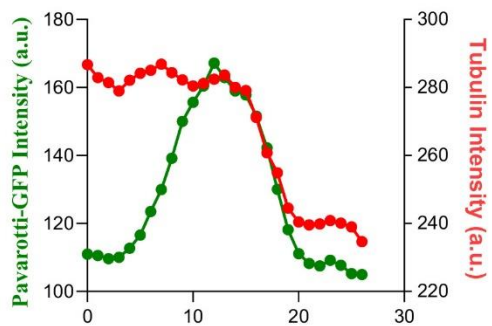
A Asymmetric overlap



B Symmetric overlap



C



D

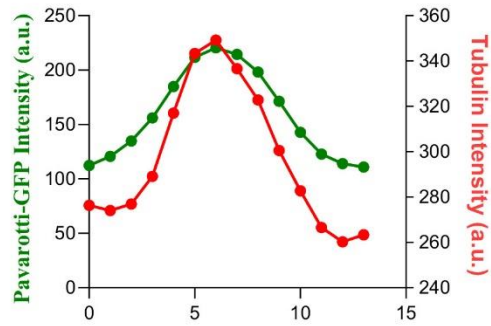


**Fig 18. Symmetric and Asymmetric overlaps organised by Pavarotti.** (A) Time lapse images of MTs forming asymmetric overlaps. MTs are numbered in yellow. Two MTs (number 1 and 2) from one side overlaps with a MT (number 3) from the opposing side in antiparallel manner. (B) MTs forming stable symmetric overlaps. (C-D) Quantification of average Pav-GFP intensity (left axis) measured at the junction of MTs for asymmetric (C) and symmetric (D) overlaps. MT intensity is measured (Right Y axis) by line scan across the junction. X-axis measures the length of line scan.

---

## Discussion

Centralspindlin is an important constituent of the anaphase central spindle. This chapter demonstrates the ability of the Centralspindlin complex to organise micropatterned MTs into antiparallel overlaps in vitro. I showed that the *Drosophila* Centralspindlin complex undergoes clustering as previously reported for its *C.elegans* homologue (Hutterer et al., 2009). Although clusters could potentially represent protein aggregates, Pav-GFP clusters are spatially restricted to plus ends of MTs, accumulate over time and transfer between MTs suggesting that they represent physiologically relevant oligomeric structures. The presence of end caps implies that upon reaching the end of the MT, Centralspindlin complex does not simply fall off. Instead, the complex exhibits a relatively low unbinding constant ( $K_{off}$ ) from plus ends and consequently a high dwell time. High dwell time allows for more particles to reach the MT end during this period and form oligomers. Oligomerisation would endow the cluster with more MT binding sites and consequently higher dwell times to form a positive feedback loop. Assuming Centralspindlin binds uniformly along the length of the MT, the number of motile particles reaching the MT end in any period of time would depend on the speed and processivity of the motor and the length of the MT. A processive motor with a low  $K_{off}$  from the plus end, would be able to establish a linear relationship between the number of motors clustered at the end and MT length. This has previously been observed for motors affecting plus end dynamics such as KIF4A (Subramanian et al., 2013; Wijeratne and Subramanian, 2018) and depolymerising kinesins, Kip3p and MCAK (Helenius et al., 2006; Varga et al., 2006). Analysis of Pavarotti intensities at plus ends of stabilised MTs confirm this linear scaling hypothesis. In cells, Centralspindlin clustering is pivotal to central spindle formation and is

tightly regulated (Basant et al., 2015). As described here an important outcome of clustering is linear scaling though how it affects central spindle organisation mechanistically remains unclear. Given Centralspindlin clusters are also sliding competent, one possible outcome could be a scaled sliding force. In this view, a short MT with less number of Centralspindlin clusters would result in decreased sliding forces compared to longer MTs with more sliding competent motors present at its plus ends. As a result, longer overlaps would be resolved rapidly. Future experiments with altered motor processivity without affecting its oligomerisation would be critical in answering this.

Experiments with polymerising MTs also revealed that these large clusters represent mobile entities capable of switching MT tracks. When MTs encounter each other at an angle these clusters were transferred and flowed to the neighbouring plus ends. What determines when Pav-GFP clusters would engage in sliding versus undergo track switching? In my experiments, I never detected transfer of Pav-GFP clusters when the contact angle between MTs was close to 180-degree; in other words when MTs contacted each other along their axis I did not observe transfer of Pav-GFP clusters. Therefore, although motile, track switching is constrained by geometric considerations. How does this affect spindle organisation? Central spindle is a bipolar structure with parallel microtubules from either side bundled in an antiparallel fashion. Presumably, in this geometry, plus ends of most of the antiparallel contacts are in an approximately 180-degree orientation. If Pav-GFP clusters could switch tracks in this orientation stable Pav-GFP clusters would not be expected to form at the centre of these overlaps. Thus, geometric constraints enable Centralspindlin complex to be focused from either side and generate stable sliding forces in the antiparallel region without changing tracks.

Sliding forces generated by Pavarotti leads to intense buckling of the MT network. Results from patterned MT networks revealed that although such forced are usually disruptive when involving a two MTs, they could be balanced if joined by other MTs as in a bundle. Crowded networks of defined geometry thus behave as entirely different system than an isolated MT pair. Importantly, these networks, with geometric constraints could be arranged in either symmetric or asymmetric manner, illustrating surprising plasticity of MT arrangements. To my knowledge this is the first instance of Pavarotti arranging MT networks and forming symmetric or asymmetric overlaps.

However, one major limitation of this system is the rarity of such overlaps. Most overlaps were between MT pairs and unstable due to constant buckling under sliding forces exerted by Pav-

GFP. Therefore, to increase the possibility of achieving stable overlaps I can either increase the number of antiparallel MT contacts or decrease the magnitude of buckling, which is the purpose of the following chapter.

The magnitude of buckling in a MT network is both a function of sliding forces and length of overlaps between participating MTs. Hence, one possible way of reducing buckling is by controlling the length of MTs and overlaps. For antiparallel MTs, the overlap length could be controlled in vitro by a two-component system of PRC1 and KIF4A as shown before (Bieling et al., 2010) (also see Introduction page 38 for detailed mechanism of length control of MT overlaps). In the following chapter, I attempt to reconstitute stable antiparallel overlaps by using *Drosophila* version of both PRC1 and KIF4A.

# Chapter 6

During anaphase, between segregating chromosomes, parallel arrays of MTs from either side interdigitate in an antiparallel manner to form the central spindle (Glotzer, 2009). How this bipolar structure with defined sections of parallel and antiparallel contacts between MTs is formed and maintained is poorly understood. Although I showed that the kinesin-6, Pavarotti, could organise MTs to form overlaps (see Chapter 3), these overlaps were often unstable. Further Pavarotti organised MTs lacked discrete sections of antiparallel overlaps. MTs from either side grew unabated, leading to buckling, and formed bundles along their entire length. To recapitulate a topology more akin to the central spindle, more specifically to restrict antiparallel overlaps to a stable invariant length, I sought to employ a two-component system of PRC1/KIF4A, that has previously been shown to specifically control antiparallel overlap length in vitro.

KIF4A, a chromo-kinesin (kinesins involved in chromosome movement) essential for central spindle organisation, robustly suppresses plus-end MT dynamics in vitro (Bringmann et al., 2004; Kurasawa et al., 2004). Together with XPRC1 (Xenopus homologue of PRC1), XKlp1 (Xenopus homologue of KIF4A) forms a minimal set of proteins capable of controlling the length of antiparallel MT overlaps while simultaneously allowing for unaltered plus end dynamics of single or parallel MTs in vitro (Bieling et al., 2010). However, the mammalian counterparts of these proteins, PRC1 and KIF4A, appeared unable to support such polarity specific behaviour (Hannabuss et al., 2019). I therefore tested whether their *Drosophila* homologues-Fascetto (Feo) and Klp3A, could support the polymerisation of single MT while simultaneously restricting growth of antiparallel overlaps.

## Results

### Fascetto selectively recognises antiparallel overlaps

Fascetto (Feo), the *Drosophila* homologue of PRC1, despite being essential for central spindle formation, remains poorly characterised (Verni et al., 2004). Although the domain features of Feo are similar to PRC1, which is comparatively well characterised, unlike PRC1 it lacks any identifiable nuclear localisation signal (Fig 19A). I purified Feo-GFP (~106KDa) from insect cells by affinity purification with a C-terminal PC tag followed by gel filtration (Fig 19B, see methods). To my knowledge, this is the first report of full-length Feo purification. I then tested

whether purified Feo-GFP is active in vitro and can selectively bind MTs, particularly antiparallel overlaps. I first attached short biotinylated GMPCPP stabilised MT seeds to a passivated glass surface using Fibrinogen biotin-Neutravidin sandwich (see Methods) and added free GTP Rhodamine tubulin (12  $\mu$ M) along with 5 nM of Feo-GFP (Fig 19C). MT plus and minus ends were identified by their distinctly different growth speeds. Sufficient density of seeds allowed growing MTs to occasionally encounter each other in either parallel or antiparallel orientation. This allowed me to visualise Feo-GFP binding to the MT lattice as polymerisation progressed by TIRF imaging. Under these conditions, strong Feo-GFP accumulation was observed specifically in regions of antiparallel overlaps between growing plus ends but not on either individual MTs or parallel contacts (Fig 19D and E for quantification). This suggests Feo-GFP alone can selectively target antiparallel contacts similar to PRC1 from Xenopus (Bieling et al., 2010).

### **Klp3A is an active motor that accumulates as a cluster on microtubule tips**

I next tested the effect of Klp3A on single stabilised MTs. Klp3A is a chromo-kinesin with a N-terminal motor domain followed by nine short, coiled coil domains (Williams et al., 1995) (Fig 20A). I purified full-length Klp3A motor with a GFP tag for visualisation and a PC tag for affinity purification from insect cells (~166kDa) (Fig 20B, also see Methods for detailed purification strategy). Purified full-length Klp3A motor was able to bind stable GMPCPP MTs and localised as an intense GFP cluster at MT plus ends (Fig 20C and D for quantification). In addition, I also performed a gliding assay to test the activity of full-length motor. Full-length Klp3A robustly supported gliding motion of MTs with an average velocity of 0.25  $\mu$ m/sec (Fig 20E), marginally slower than reported velocities of its Xenopus homologue (Bringmann et al., 2004). This suggests that purified full-length Klp3A is an active motor.

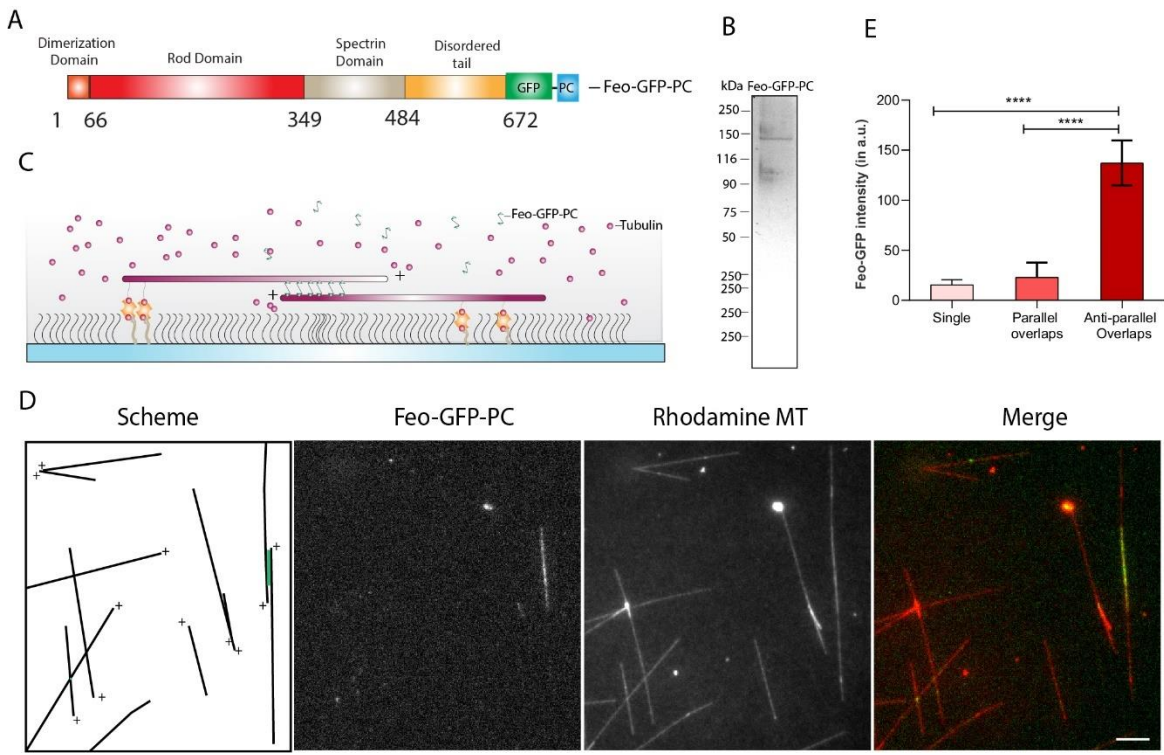


**Fig 19. Fascetto specifically binds antiparallel overlaps.** (A) Domain organisation of Fascetto (Feo). The C-terminal spectrin and disordered tail mediates MT binding. (B) Coomassie staining of recombinant Feo-GFP-PC, purified from insect cells. (C) Schematic of in vitro MT polymerisation assay to test Feo specificity. MTs (in purple) were grown in presence of soluble tubulin from stable biotinylated seeds bound to a passivated glass surface by Fibrinogen-biotin (brown curved rods red spheres) - Neutravidin (in orange) sandwich. (D) Left, Schematic depicting orientation of MTs. Orientation of MTs were determined by measuring the polymerisation speed of growing MTs. Faster growing ends were denoted as plus ends and slower growing ends were denoted as minus ends. Right, Feo-GEP-PC only binds to antiparallel crosslinks. (E) Background subtracted Feo-GFP intensity was measured for single MTs ( $n=17$ ) and MTs crosslinked in a parallel ( $n=21$ ) or antiparallel manner ( $n=18$ ). One way ANOVA was performed.  $p<0.0001$ , Error bars represent SD. Scale bar 1 $\mu$ m

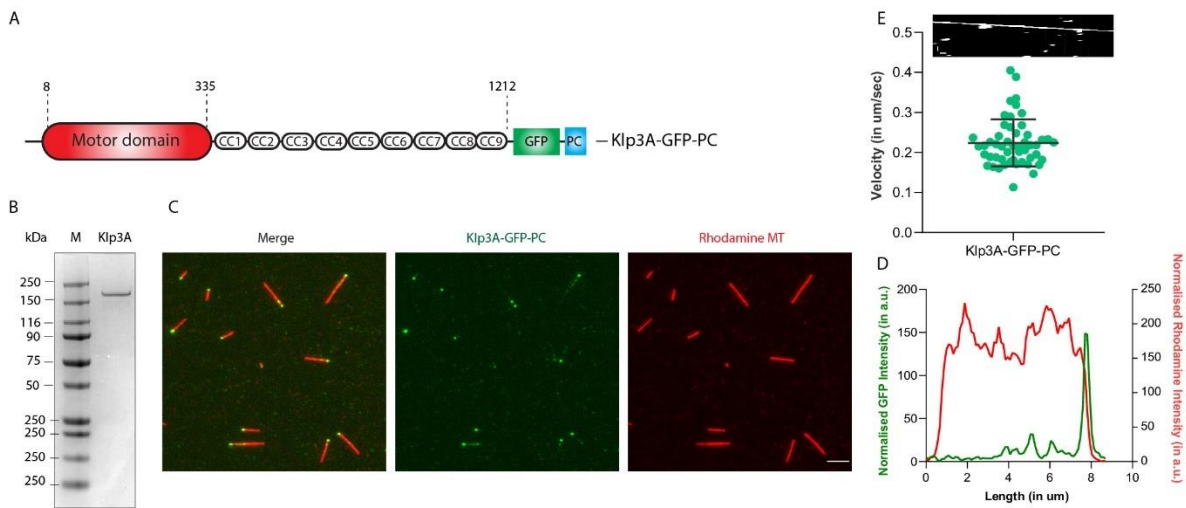


**Fig 20. Klp3A is an active tip-clustering motor.** (A). Domain organisation of Klp3A. Note the long stretch of short coiled coils (CC) in the stalk and tail domain. (B) Coomassie staining of recombinant Klp3A-GFP-PC (~167 kDa), purified from insect cells. (C) Klp3A binds to MTs and accumulates at its tip. (D) GFP line profile (left Y-axis) along with MT intensity (Right Y axis), shows Klp3A accumulation. (E) Gliding velocity of Klp3A ( Mean speed 0.25  $\pm$  0.04  $\mu\text{m/sec}$ ) determined by Kymograph (in inset) analysis.

### Feo and Klp3A form a sliding competent complex in vitro

In vivo, Feo and Klp3A forms a stable complex (D'Avino et al., 2007). Previous reports of their homologs, PRC1 and KIF4A, indicate this MAP-motor complex could in fact support MT sliding and is important for anaphase elongation in vivo (Vukušić et al., 2021; Wijeratne and Subramanian, 2018). Since KIF4A is a dimeric motor, sliding of MT pairs would require oligomerisation. This is achieved by complex formation with an oligomeric PRC1 (Wijeratne and Subramanian, 2018). Therefore, MT sliding could serve as a proxy for functional complex formation between Feo and Klp3A proteins. To investigate such a possibility, I anchored a biotinylated MT to the surface and added 5 nM Feo and 20 nM Klp3A along with free GMPPCP stabilised MTs (Fig 21A). If Feo and Klp3A form a complex in vitro, the free (unanchored) MT would be expected to first bind the surface attached MT and then move across it with a steadily shrinking overlap length. Time-lapse imaging revealed that MT pairs indeed slide relative to each other (Fig 21B) and the length of MT overlap decreases steadily

over time. As the overlap shrinks, fewer binding sites are available for Feo-Klp3A complex to occupy. I therefore measured the intensity of GFP over time. As overlap length shrank, total GFP intensity also decreased concurrently (Fig 21C). In contrast, average GFP intensity across the overlap rose dramatically (Fig 21D) and concentrated to a sharp peak over time (Fig 21E). Therefore, although some of the complex was presumably lost as the overlap shrunk, overall, the density of the complex in the overlap increased over time. This contrasts with yeast Ase1p, which is bound stably during similar overlap shrinkage (such that its total intensity remains moderately stable) and concentrates over time to provide an entropic barrier that resists further sliding (Lansky et al., 2015) (See also Introduction, page 37). Feo-Klp3A complex appears to be “leaky” and leaves the overlap considerably faster.

### **Feo and Klp3A inhibit plus end growth and regulate sliding**

Having established both Feo and Klp3A as active proteins capable of forming a complex, I then investigated whether these two proteins can give rise to stable antiparallel overlaps. While such stable overlaps have been reported for Xenopus proteins (Bieling et al., 2010), their mammalian homologues were suggested to be unable to replicate the same (Hannabuss et al., 2019; Subramanian et al., 2013). This could either be due to an intrinsic species specificity or the specific conditions used in different assays, particularly ionic strength of buffer. I therefore systematically investigated MT dynamics under an extensive set of varying concentrations of Tubulin, Feo and Klp3A, as well as salt concentration.

In low ionic strength buffer, Feo-Klp3A complex strongly binds to MTs. Indeed, when 12  $\mu$ M tubulin was polymerised with Feo and Klp3A, all MTs were immediately decorated by a GFP cap that remained stable throughout the course of the experiment (Fig 22A, left). Occasionally these caps fused with each other to form aster like structures (Fig 22A, right). Time lapse imaging and kymographs revealed that almost all MTs were growing only from their minus end with a stable GFP cap restricting all plus end dynamics (Fig 22B). In control conditions with only Klp3A, MTs often grew from their plus ends and underwent catastrophe, albeit briefly (Fig 22B, left). In contrast, with the addition of Feo along with Klp3A, plus ends of MTs were tightly capped and no MT dynamics were observed. This indicates that compared to Klp3A alone, Feo-Klp3A binds MTs more stably. Under such conditions growing minus ends of MTs had a significantly higher polymerisation speed (mean speed 0.45  $\mu$ m/min) than Klp3A alone (mean speed 0.28  $\mu$ m/min) (Fig 22C). I also observed MTs sliding along each other, as in Fig 21, under such conditions indicating that the Feo and Klp3A could still form a complex

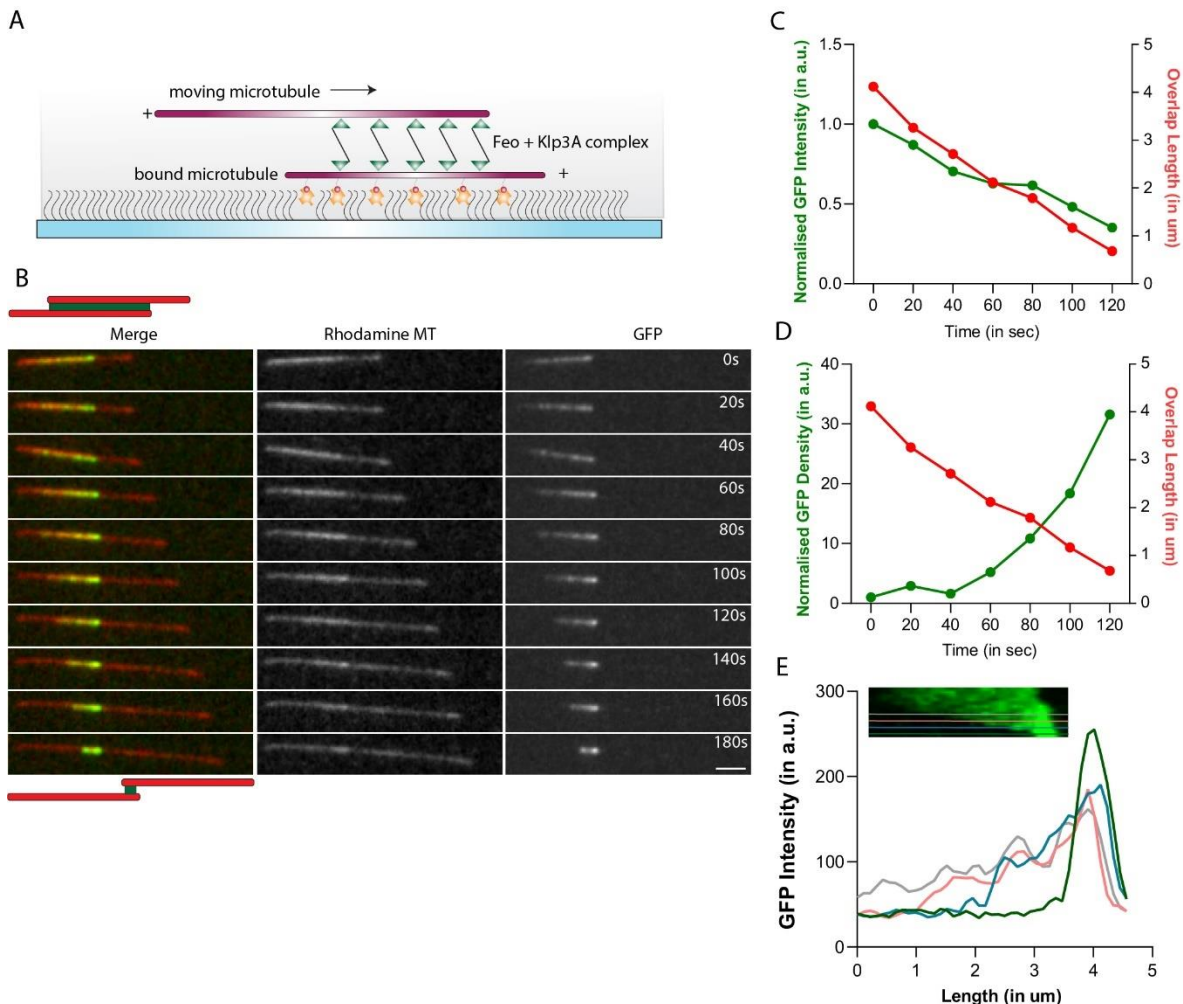


**Fig 21. Feo-Klp3A complex slides antiparallel MTs** (A) Schematic showing a free GMPCPP stabilised MT moving across a surface bound MT (anchored through Fibrinogen-Biotin-Neutravidin sandwich). Since both Feo and Klp3A are tagged with GFP, here it is represented as a single complex (in green). (B) Time lapse images showing sliding activity of Feo-Klp3A complex. As the MTs slide apart (middle column, rhodamine MT) in the green channel (third column), the overlap length marked by the complex decreases consistently. Schematic on the right indicating the initial and final state of the MT pair. Scale bar 2μm. (C-D) Total GFP intensity (C), Mean GFP intensity (D) and Overlap length (marked by increased rhodamine intensity) was measured at each time point as the overlap decreased. Each point is an average of 6 sliding MT pair. For (C), a decrease in total GFP intensity (left Y axis) indicates complex removal from the overlap as it shrinks. In (D) Increase in Mean GFP intensity indicates the residual complexes in the overlap are becoming increasingly densely packed. (E) GFP intensity was measured as line profiles at indicated points (in inset) of sliding. GFP intensity became progressively brighter and concentrated to a spot.

(Fig 22D). These sliding events happened whilst MT polymerisation is ongoing. Like before, I measured the intensity of GFP during the course of such sliding movements. Similar to sliding between stable MTs, as overlap length shrunk, the amount of GFP also decreased concomitantly (Fig 22E). However, interestingly the mean intensity across the overlap length increased and plateaued even while the overlap length kept decreasing (Fig 22F). This suggests that under such conditions, the off rate of the Feo-Klp3A complex from the MT approaches the sliding rate of the MT pair. Therefore, in the presence of soluble tubulin, MTs can undergo relative sliding reminiscent of anaphase B but do not allow for any plus end dynamics in low salt conditions.

### **Feo and Klp3A regulate formation of stable overlap**

Antiparallel overlaps of MTs at the central spindle are formed by growing plus ends bundled by PRC1, KIF4A and other central spindle proteins. I wondered whether increasing the salt concentration could weaken the initial Feo-Klp3A interaction to an extent that allows for plus end growth but is restrictive to antiparallel overlap growth. To specifically reveal the localisation of individual proteins, as both are labelled with GFP, I incubated Klp3A-GFP with GBP-Alexa 647 for 10mins prior to its introduction in the reaction chamber. I diluted Klp3A-GFP/GBP- Alexa 647 to a final concentration of 15 nM and added it along with 5 nM of Feo-GFP and 13.5  $\mu$ M Tubulin in mid salt buffer (75 mM Potassium chloride and 85 mM Potassium acetate) to surface immobilised seeds (Fig 23A). MTs grew from their plus ends (indicated by higher polymerisation speed) and encountered each other. Feo-Klp3A complex marked all antiparallel plus end contacts immediately after their encounter. Plus ends continued to grow only for a brief period after such encounters and eventually stopped all dynamics with a strong, specific accumulation of Feo-GFP and Klp3A-GFP/GBP- Alexa 647 in the intervening overlap (Fig 23B). Kymographs of such pairs of MTs showed a sharp change in plus end growth speed concomitant with Feo-Klp3A arrival at the overlap and eventual cessation of plus end dynamics on both sides (Fig 23C). These final overlaps were stably maintained during the course of the experiment (at least for 20-30 mins). I found significant reduction in polymerisation speed of pairs of MTs immediately before and after each encounter till they stopped growing (Fig 23D). Hence, stable antiparallel contacts of a defined length between two isolated MTs can be established by two central spindle proteins, Feo and Klp3A. While stable, these overlaps are not the central spindle, as they are symmetric, non-bundled MT pairs linked one to one.

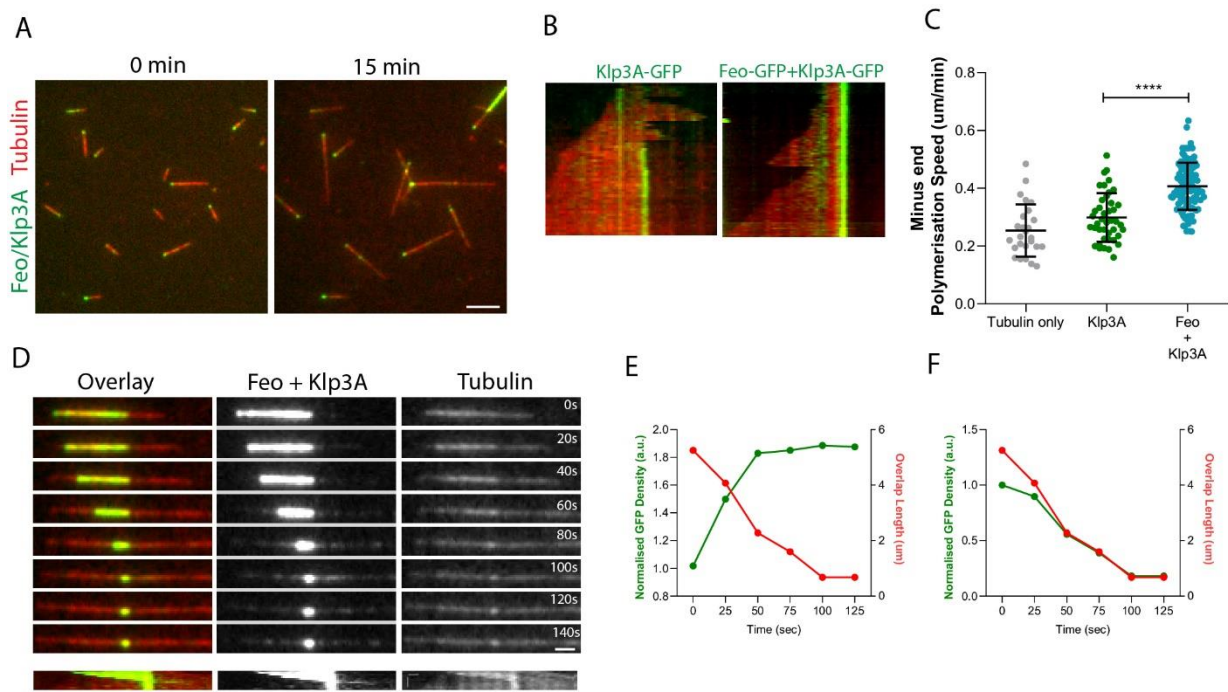


**Fig 22. Feo-Klp3A complex results Minus end growth and sliding**

(A) Snapshot of the field of view at two different time points after tubulin addition. A stable green cap, indicative of Feo-Klp3A complex was present in all MTs. Growth in this case occurred exclusively from minus ends. Scale bar 5  $\mu\text{m}$  (B) Kymographs of MT growth in presence of Klp3A alone (left) or Klp3A and Feo (right). Note, in left, MT plus ends initially grew and underwent catastrophe before Klp3A stably capped that end. In Feo-Klp3A complex, such transient plus end dynamics was not observed and MT grew solely from its minus end. (C) Minus end polymerisation speeds were measured in presence of either 13.5  $\mu\text{M}$  tubulin only (n=27) or with Klp3A (n=45) or with Feo and Klp3A (n=78). Students t-test,  $p < 0.0001$ . Error bars represent SD. (D) upper panel Time lapse images of shrinking overlaps formed between growing minus ends (pointed outwards) Scale bar 2  $\mu\text{m}$  .Lower panel, Kymograph of the same overlap. Scale bar horizontal 1  $\mu\text{m}$ , vertical 10 sec. (E-F) Total GFP intensity (E), Mean GFP intensity (F) and Overlap length of MTs (was measured at each time point as the overlap decreased. Each point is an average of 8 sliding MT pair. In (E) Increase in Mean GFP intensity plateaued after 50sec as the overlap length continued decreasing.

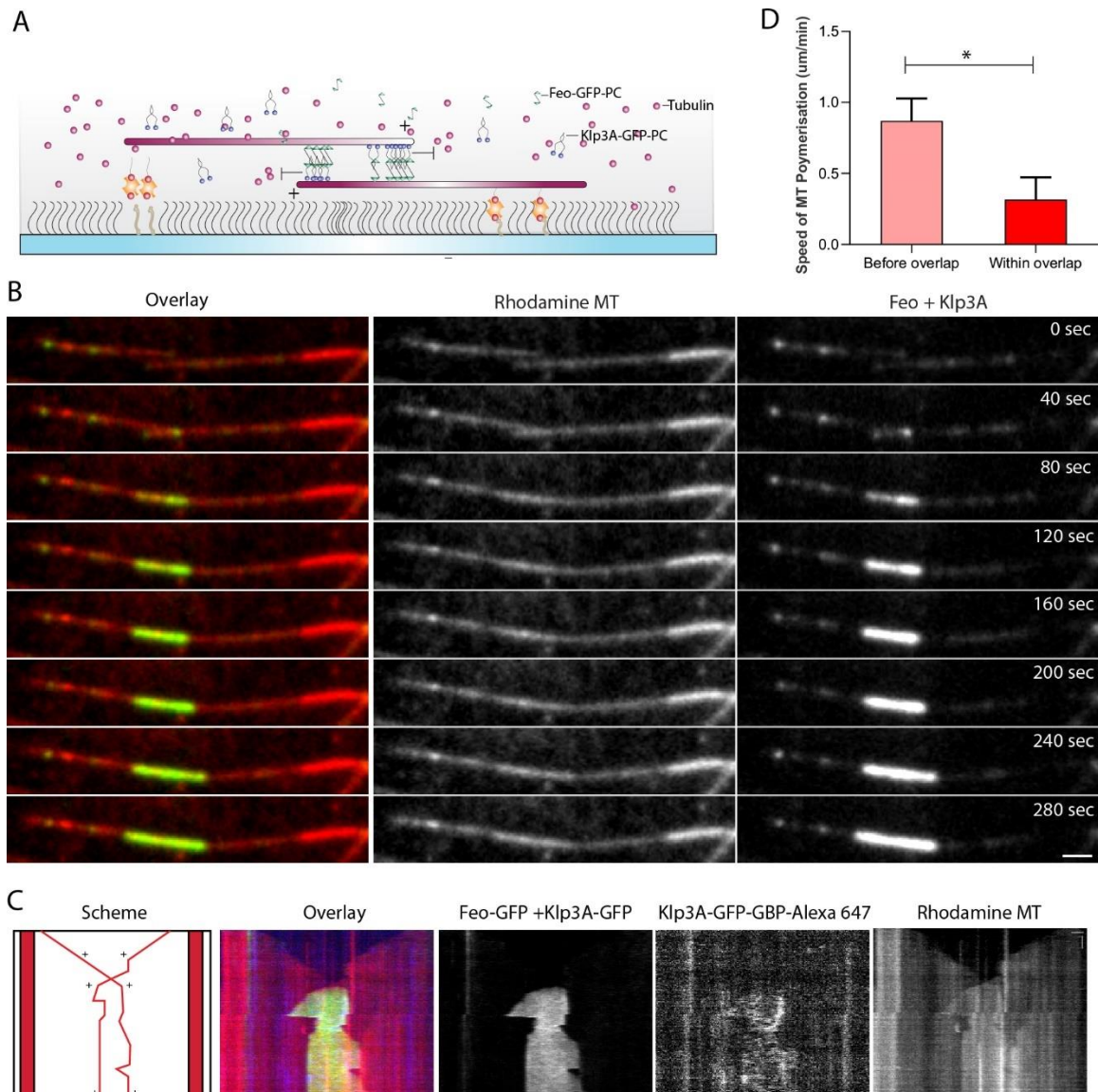


**Fig 23. Stable antiparallel overlaps achieved by Feo and Klp3A.** (A) Schematic of the assay. Random surface attached MT seeds were grown with 13.5  $\mu$ M tubulin in presence of 15 nM Klp3A-GFP (in blue) (bound to GBP-Alexa647 for visualisation) and 5nM Feo-GFP (in green). (B) Time lapse images of stable antiparallel overlap formation. MTs growing from opposite sides contacted each other (t=80sec) and soon stopped growing (t=240sec). Forming a stable overlap. Scale bar 2  $\mu$ m (C) left, schematic showing the orientation and polarity of the growing MTs. Right, Kymograph analysis of each channel. Note, both ends of the overlap as observed Feo-GFP completely stops growing. Scale bar horizontal 1  $\mu$ m, vertical 10 sec (D) MT growths were measured for individual MT pairs before and right after their contact (n=8). Paired t-test,  $p = 0.0306$ . Error bars indicate SD.

### **Asymmetric antiparallel overlaps can be generated by patterned microtubule growth**

I hypothesised that the core structure of the central spindle consists of numerous antiparallel contacts, aligned and bundled in the midzone and could be replicated by significantly enriching for the probability of antiparallel encounters by patterning MT seeds to a high density. I patterned short, GMPPCP MTs in parallel bars to a high density through neutravidin attached to patterned fibrinogen-biotin anchor as described previously (see Chapter 4 and Materials and Methods). I added 5 nM of Feo-GFP and 15 nM of Klp3A-GFP along with 13.5  $\mu$ M of Rhodamine tubulin in mid-salt buffer to trigger polymerisation. MTs regularly grew out of these patterns with longer plus ends, a result of their higher polymerisation speed, poised to make antiparallel contacts (Fig 24A). Immediately after addition, Feo-Klp3A complex is detected on short MT contacts in the patterned region (Fig 24B, 0min). These contacts are presumably made within the pattern by high density of growing plus ends and severely limits the overall number of plus ends emerging out of the pattern, capable of making contacts with similarly nucleated MTs from neighbouring patterns. In other words, what is gained in the ability to stabilize overlaps, is lost in the number of overlaps made.

Even with such limited encounters I clearly saw instances of stable antiparallel contacts between MTs growing from patterned seeds on either side (Fig 24B, 12min). I wondered whether given the propensity of antiparallel contacts in such assays I could detect asymmetric overlaps by chance. Strikingly, careful examination of such contacts revealed that indeed asymmetric overlaps are formed, albeit rarely, by sequential antiparallel contacts between a single MT from one pattern interacting with two neighbouring MTs, growing in parallel manner, from another pattern (Fig 24C). After an initial contact is established between an antiparallel pair (Fig 24C, fourth row, 04:00min), a third MT makes a second contact with the pair at an adjacent point in the lattice (Fig 24C, sixth row, 06:40min). Such asymmetric overlaps are never seen without patterns. Importantly, the key activity of the Klp3A-Feo system under carefully selected salt condition, ensures that MTs undergo minimal buckling (Fig 24C, rows seven to nine) till these two adjacent contacts merge to form a single, stable asymmetric antiparallel overlap. This is the first instance of a reconstituted stable asymmetric central spindle-like arrangement in vitro.

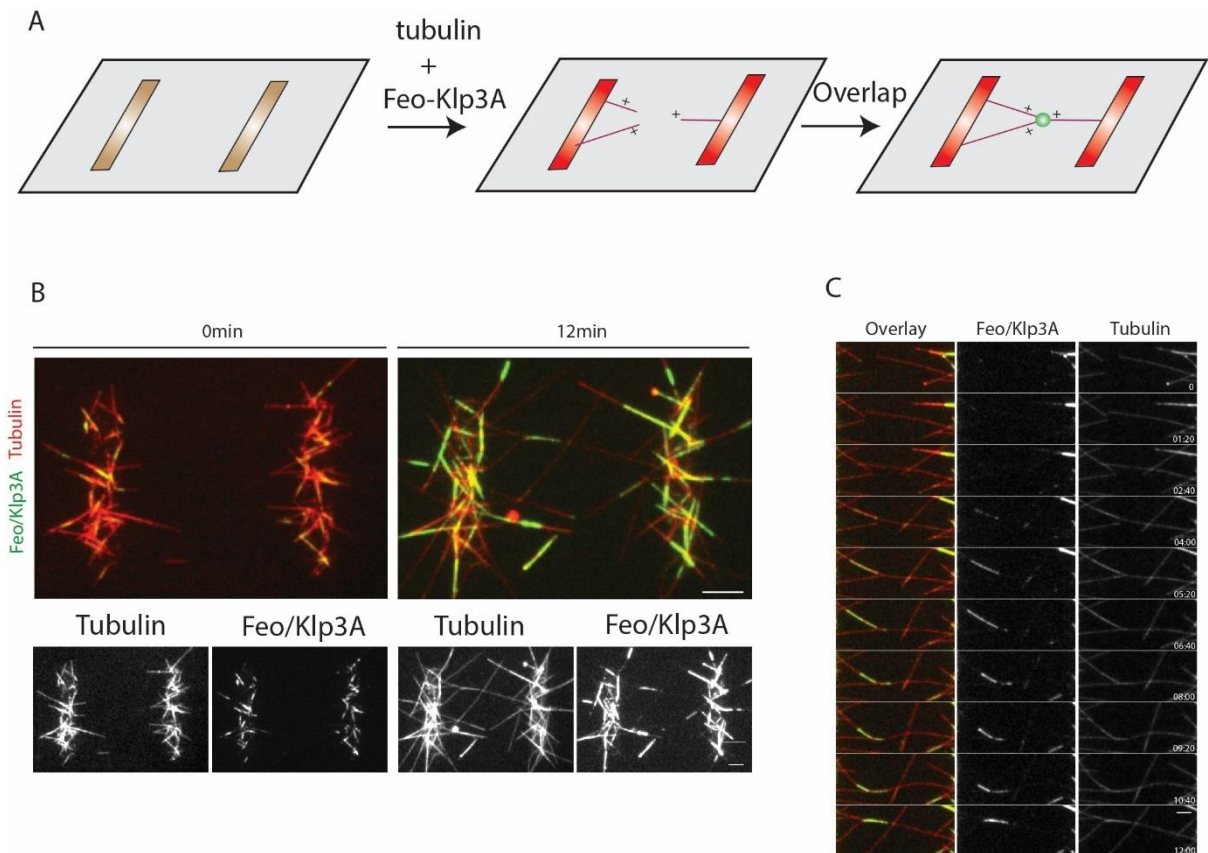


**Fig 24. Feo-Klp3A can form stable asymmetric overlaps.** (A) Schematic of the assay. MT seeds (in red) were micropatterned and allowed to grow in presence of 5 nM Feo-GFP and 15 nM Klp3A-GFP and 13.5  $\mu$ M tubulin. (B) Snapshots of MT growth at 0 min and 12 min post tubulin addition. Note, GFP can be observed on patterns and few MTs grow out of them (bottom panel at time 0). On right, at 12min, contacts are seen to form between few growing MTs. Scale bar 5  $\mu$ m (C) Time lapse of overlap formation. Initial contact is made at 5:20 min between two MTs. This is further joined by a third MT at 8min. Eventually they collapse to form a single stable asymmetric overlap. Scale bar 2  $\mu$ m.

## **Discussion**

### **Relative sliding of microtubules by a Motor-non Motor MAP combination**

Under low salt conditions, using stable MTs I could reconstitute sliding activity of Feo-Klp3A complex, similar to PRC1-KIF4A system described previously (Wijeratne and Subramanian, 2018). MT sliding activity of PRC1-KIF4A system, like Kinesin-5 and Kinesin -6, was shown to be important for spindle elongation in U20S cells recently (Vukušić et al., 2021). Hence, Feo-Klp3A sliding may represent a physiologically relevant step in spindle elongation. Previous reports of sliding activity of a motor in conjunction with PRC1 family member Ase1p from fission yeast identified a crucial ability of Ase1p to resist filament sliding beyond a certain threshold (Braun et al., 2011). As MTs shorten, Ase1p is exclusively accumulated into the shortening overlap. This produces an entropic force resisting further sliding (Lansky et al., 2015). However, such an entropic barrier is not offered by mammalian PRC1 which acts like a mechanical dashpot where the resistive force scales with sliding velocity but does not oppose further sliding at any point (Gaska et al., 2020). Using Feo-GFP, I saw a gradual decline in total GFP intensity but a relative increase in mean GFP intensity over time that did not change the velocity of sliding. Feo-GFP thus acts in similar fashion to PRC1 as a leaky binder, that concentrates in the shrinking overlap with an appreciable off-rate.

### **Emergent control of antiparallel overlaps by a two-component system**

I have now established a minimal two-component system for organising stable antiparallel overlap in vitro. This concerted action is dependent on three key properties of the Feo and Klp3A system: -a) Selective recognition of antiparallel contacts by Faschetto, b) Formation of the Feo-Klp3A complex and c) Inhibition of plus end MT dynamics by Klp3A. Of these, both formation of the complex and inhibition of plus end dynamics is strictly dependent on ionic strength of the buffer. This might explain the different effects of this two-component system reported previously by different groups (Bieling et al., 2010; Subramanian et al., 2013). In low salt condition, Feo-Klp3A complex appears as end caps on MTs and readily inhibits plus end dynamics as described previously for PRC1-KIF4A system in vitro (Subramanian et al., 2013). Conversely, at high ionic strength, formation of Feo-Klp3A complex is hindered but Klp3A allows for MT plus end dynamics.

For stable antiparallel overlap to emerge, the system needs to be in a region of the parameter space where both these activities are suitably balanced to allow for plus end growth of single MT and specific growth inhibition of antiparallel pairs. I did find such a nexus point for Feo-

Klp3A, as was previously found for XPRC1 and XKlp1(Bieling et al., 2010). This is in agreement with the observation that upon reduction of Feo or Klp3A levels in cells, central spindle organisation is perturbed and MT bundles assume an elongated bipolar shape that leads to a diffuse localisation of central spindle proteins (Verni et al., 2004).

Specific recognition of antiparallel overlaps appears to be a conserved feature of members of the PRC1 family, although to different extents. Ase1p in fission yeast offers much reduced selectivity as compared to stringent mode of binding by PRC1 (Janson et al., 2007). Feo, the *Drosophila* homologue is more similar to PRC1 than its yeast counterpart. Kinesin-4 homologues are absent in fission yeast. Length control in such systems therefore may have completely different mechanisms.

### **Asymmetric central spindle-like organisation**

Previously, using PRC1 and KIF4A in low salt conditions, a bipolar mini-spindle like architecture was established by Hannabuss et al., 2019. In these conditions, PRC1-KIF4A capped and fused the plus ends of MTs nucleated in solution allowing for extension of such bundles only by minus end polymerisation. In my reconstitution with MT seeds, majority of which are surface immobilised, under low salt conditions, I did observe occasional fusion of Feo-Klp3A caps and extension by minus end growth. This indicates the two systems are equivalent in MT organisation capabilities. With freely nucleated MTs in solution Hannabus et al. repeatedly observed formation of symmetric central spindle like bundles. This argues for an inherent capacity of the PRC1-KIF4A system to establish **symmetric** organisation within MT bundles. How then are asymmetric central spindle organised? Is a third component required to balance an asymmetric network?

Growth from surface anchored patterned seeds imposes a confined geometry on the system by restricting MT movement. In this system MTs are forced to adopt conformations that are otherwise not favoured in a freely diffusible system, perhaps because MT organisation would always rearrange to minimise overall strain in the network. *In vivo*, minus ends of central spindle MTs are possibly anchored to kinetochore MTs and much closely resemble the confined system. Such confined systems could occasionally give rise to asymmetric contacts that are stable for an extended duration. Therefore, asymmetric central spindle like structures can be formed and stabilised by the same two-component system by imposing geometric confinement.

# General Discussion and Future Directions

## Endosomes at the central spindle

In vivo data of late endosomes point towards the existence of symmetrically segregating cargo even in the presence of asymmetric tracks (Fig 5). Their identity remains elusive. Notwithstanding, these results re-enforce my hypothesis that during SOP division only a subset of cargoes are inherited in a biased manner.

While endogenous Rabs is a powerful tool to provide novel insights into the endocytic machinery during division, currently I am unable to confirm the identity of the late delta endosomes.

One possibility is that late Delta endosomes actually represents lysosomes. This is supported by the fact that the same motor that drives Sara positive early delta endosomes, Klp98A, has also been reported to bind autophagosomes and lysosomes, mediating their fusion (Mauvezin et al., 2016). Recruitment at these vesicles is regulated by Rab14. The mammalian orthologue of Klp98A, KIF16B also interacts with Rab14 in mice and is involved in Golgi to endosome transport (Ueno et al., 2011). This highlights that Rab14-KIF16B interaction may be conserved across evolution. In diverse contexts Lysosome transport is driven by kinesin-3, kinesin-1 or even dynein (Cabukusta and Neefjes, 2018). During asymmetric division of hematopoietic stem cells, lysosomes are asymmetrically segregated to the daughter cell and contribute to cell fate (Loeffler et al., 2019; Pu et al., 2015). Therefore, lysosomes are exciting as candidates for vesicles targeted to the central spindle for partitioning during mitosis (Guardia et al., 2016).

Currently analysis of endogenous endosome dynamics is limited by crowding of neighbouring cells. This severely limits the ability to reliably detect the endosomes specifically present in SOPs, particularly in Z-axis. I am currently aiming to alleviate this problem, by using an deGrad-FP (Caussinus and Affolter, 2016) system (and/or GFP-RNAi) homogenously expressed in the tissue but specifically repressed in the SOP. Alternatively, I have recently made flies expressing a nanobody against GFP fused to mCherry under UAS control. This can be specifically expressed in SOPs and will thus provide me with the SOP-specific fraction of the GFP signal into the mCherry channel.

Once I am confident that I have identified a bona fide symmetrically segregating endosome, my next goal would be to identify its associated motors. For this, I have developed a GBP-

BioID2 (Roux et al., 2013) line to selectively attach biotin-ligase, BirA, to GFP tagged compartments using anti-GFP nanobodies. This will allow the identification of the complete set of proteins, in particular motors, present at the surface of endosomes. This will be combined with an RNAi/CRISPR approach to analyse the behaviour of the compartments in mutant background for motors.

## How to build a Central Spindle

### A. Overlap length control

Results with the *Drosophila* version of the PRC1-KIF4A system reveals an extremely narrow region in the parameter space allowed for both growth of single MTs and inhibition of antiparallel overlap extension. This is consistent with previous conflicting reports (Bieling et al., 2010; Subramanian et al., 2013). While using Xenopus proteins, Bieling et al., could generate stable antiparallel overlap with no binding on single MTs, Subramanian et al., reported end- clusters on single MTs. Note in the latter case, tubulin polymerisation was not performed so there is a likelihood, no matter how small, that presence of soluble tubulin alters the binding affinity of PRC1/KIF4A. Much more likely is the conclusion that these experiments were performed in dramatically different ionic conditions (low in case of Subramanian et al., 2013, and high in case of Bieling et al., 2010), which perhaps has a strong effect on MT binding affinity of these two proteins (Gaska et al., 2020). Additionally, I found that the system is extremely sensitive to PRC1/KIF4A concentrations. Balance of activity therefore depends upon three important parameters-1) PRC1 affinity for MTs 2) KIF4A affinity for MTs, with both parameters differing for single vs antiparallel MTs (Fig 15) and 3) probability of PRC1-KIF4A complex formation. If single MTs are allowed to grow whilst inhibit antiparallel MT pair growth, all three activities must reach a critical balancing point. This raises the question of how *in vivo* overlap length of MTs is controlled robustly.

One possibility, recently explored in Mani et al., 2021, invokes a third component-CLASP-1. CLASP-1 promotes MT rescue, thereby promoting MT polymerisation. CLASP-1's affinity for PRC1 is lower than its affinity for KIF4A. Therefore, on regions of MT overlaps, PRC1 can recruit KIF4A efficiently. However, on single MTs, CLASP1 wins the kinetic race and displaces KIF4A. This three-component module can thus offer greater flexibility and robustness to the system (Mani et al., 2021).

It is also likely that *in vivo* these proteins are regulated not only temporally but also spatially. This is supported by evidence from HeLa cells, where a midzone localised pool of Aurora B phosphorylates KIF4A (Nunes Bastos et al., 2013). Phosphorylation dramatically increases its ability to bind both MTs and PRC1. Moreover, in the absence of such phosphorylation, cells have hyper-elongated spindle midzones in anaphase. Midzone localised KIF4A also counteracts Aurora B by recruiting a PP2A phosphatase, creating a feedback loop (Bastos et al., 2014). This highlights how keenly cells regulate their antiparallel overlap length during anaphase.

Though I did find a specific point in the phase diagram that generates stable antiparallel MTs, inclusion of CLASP1 (Orbit in *Drosophila*) may improve robustness of the assay. One recurring problem in my assay was that in the presence of Feo and Klp3A (*Drosophila* KIF4A homologue), few MTs managed to escape the patterned region. This is likely due to formation of overlaps within the micropatterns itself that inhibits their growth (data not shown). Although this underscores the success of regulating overlap length, it hinders my reconstitution attempt because of lack of available MTs growing outwards from the pattern.

To overcome this barrier, I could take two complementary approaches. Firstly, I can introduce KIF4A later in the assay, once sufficient numbers of MTs have grown out from the pattern. Procedurally, this means tubulin is double injected, first with and then once without KIF4A. The second approach involves taking advantage of dual micropatterning. In this strategy, KIF4A could be anchored to the surface, in the midzone between MT nucleation regions. Absence of soluble KIF4A should allow for unhindered MT growth till the midzone where I would expect surface bound KIF4A to exert its action. I do realise this strategy requires surface bound KIF4A to still inhibit MT growth. While surface bound KIF4A can definitely bind and move stabilised MTs (Fig 20E, gliding assay), I currently do not know whether surface bound KIF4A can inhibit MT growth.

#### B. Shape of the central spindle

Central spindle is characterised by its hourglass shape, where opposing flayed parallel arrays of MTs bundle in the middle, in an antiparallel manner. This focusing of plus ends is thought to be brought about by the ingressing contractile ring, although direct evidence is lacking. How can I recapitulate this *in vitro*?

In self-organisation assays, tetrameric motors with a high dwell time at MT ends, can form asters (Karsenti et al., 2006; Surrey et al., 2001). In fact, modelling shows that if motor speed

is higher than MT polymerisation speed then by reaching the MT ends motors can crosslink MT networks (Karsenti et al., 2006). However, kinesin-5, KIF11, a slow moving motor that is still faster than MT polymerisation speed does not lead to aster formation in such assays (Hentrich and Surrey, 2010). Recently, KIF11 mediated asters were seen under conditions of low MT polymerisation speed and critically, high motor numbers (Roostalu et al., 2018). Two important parameters are shown to be critical for MT organisation in such assays-first is the ratio between MT polymerisation speed and motor speed with a low ratio favouring aster formation and second is the ratio between motor number and MT number with a high ratio leading to aster formation (Roostalu et al., 2018).

I showed Centralspindlin complex can dwell on MT plus ends (Fig 15). Furthermore, with polymerising MTs, Pav-GFP is seen to decorate all plus ends, indicating that in my assay conditions motor speed is indeed higher than MT growth speed. Therefore, one prediction of increasing Pav-GFP concentration (High motor number/ MT number ratio) would be formation of focused MT plus ends (because in the micropatterning assay, MTs are anchored at the pattern, an aster like structure seems unlikely to form). If this is true, then a bipolar hourglass shaped central spindle can be formed in vitro.

### **Reconstituting central spindle motion**

The final aim of this project is to provide a platform to study motility on central spindle MTs. The only motor so far shown to mediate this traffic is Klp98A. I have purified a truncated active construct of Klp98A (1-400) that shows efficient transport on MTs. Currently, my aim is to engage these motors in micropatterned overlap bundles.

This is relatively simple experiment but requires stabilisation of the MTs so that it could support kinesin motion. Although clear data is lacking, previous reports have suggested that PRC-1-KIF4A system can generate MT pairs that are somewhat resistant to depolymerisation (Bieling et al., 2010). If true for Feo/Klp3A system, then it provides a simple solution to the problem. Alternatively, once the bundles have formed, I could stabilise MTs by introducing taxol. This has the potential caveat of increasing overlap length by allowing robust MT polymerisation. It remains to be seen whether a bound KIF4A, can counteract this elongation preference.

## References

- Acharya, U., Mallabiabarrena, A., Acharya, J.K., and Malhotra, V. (1998). Signaling via mitogen-activated protein kinase kinase (MEK1) is required for Golgi fragmentation during mitosis. *Cell* *92*, 183–192.
- Adams, R.R., Tavares, A.A.M., Salzberg, A., Bellen, H.J., and Glover, D.M. (1998). Pavarotti Encodes a Kinesin-Like Protein Required To Organize the Central Spindle and Contractile Ring for Cytokinesis. *Genes Dev.* *12*, 1483–1494.
- Al-Bassam, J., Cui, Y., Klopfenstein, D., Carragher, B.O., Vale, R.D., and Milligan, R.A. (2003). Distinct conformations of the kinesin Unc104 neck regulate a monomer to dimer motor transition. *J. Cell Biol.* *163*, 743–753.
- Al-Bassam, J., Kim, H., Brouhard, G., van Oijen, A., Harrison, S.C., and Chang, F. (2010). CLASP promotes microtubule rescue by recruiting tubulin dimers to the microtubule. *Dev. Cell* *19*, 245–258.
- Albertson, R., Riggs, B., and Sullivan, W. (2005). Membrane traffic: A driving force in cytokinesis. *Trends Cell Biol.* *15*, 92–101.
- Alsop, G.B., and Zhang, D. (2003). Microtubules are the only structural constituent of the spindle apparatus required for induction of cell cleavage. *J. Cell Biol.* *162*, 383–390.
- Andreasson, J.O.L., Milic, B., Chen, G.Y., Guydosh, N.R., Hancock, W.O., and Block, S.M. (2015). Examining kinesin processivity within a general gating framework. *eLife* *4*, e07403.
- Arpağ, G., Norris, S.R., Mousavi, S.I., Soppina, V., Verhey, K.J., Hancock, W.O., and Tüzel, E. (2019). Motor Dynamics Underlying Cargo Transport by Pairs of Kinesin-1 and Kinesin-3 Motors. *Biophys. J.* *116*, 1115–1126.
- Arpağ, G., Shastry, S., Hancock, W.O., and Tüzel, E. (2014). Transport by populations of fast and slow kinesins uncovers novel family-dependent motor characteristics important for *in vivo* function. *Biophys. J.* *107*, 1896–1904.
- Artavanis-Tsakonas, S., Rand, M.D., and Lake, R.J. (1999). Notch signaling: Cell fate control and signal integration in development. *Science* *284*, 770–776.
- Aryaman, J., Hoitzing, H., Burgstaller, J.P., Johnston, I.G., and Jones, N.S. (2017).

Mitochondrial heterogeneity, metabolic scaling and cell death. *BioEssays* 39, 1700001

Asenjo, A.B., Krohn, N., and Sosa, H. (2003). Configuration of the two kinesin motor domains during ATP hydrolysis. *Nat. Struct. Biol.* 10, 836–842.

Asthana, J., Cade, N.I., Normanno, D., Lim, W.M., and Surrey, T. (2021). Gradual Compaction of the Central Spindle Decreases its Dynamicity as Revealed in PRC1 and EB1 Gene-Edited Human Cells. *BioRxiv* 2020.07.09.195347.

Aumeier, C., Schaedel, L., Gaillard, J., John, K., Blanchoin, L., and Théry, M. (2016). Self-repair promotes microtubule rescue. *Nat. Cell Biol.* 18, 1054–1064.

Azioune, A., Carpi, N., Tseng, Q., Théry, M., and Piel, M. (2010). Protein Micropatterns. A Direct Printing Protocol Using Deep UVs. *Methods Cell Biol.* 97, 133–146.

Babour, A., Bicknell, A.A., Tourtellotte, J., and Niwa, M. (2010). A Surveillance Pathway Monitors the Fitness of the Endoplasmic Reticulum to Control Its Inheritance. *Cell* 142, 256–269.

Barr, F.A. (2004). Golgi inheritance: shaken but not stirred. *J. Cell Biol.* 164, 955–958.

Baruni, J.K., Munro, E.M., and von Dassow, G. (2008). Cytokinetic furrowing in toroidal, binucleate and anucleate cells in *C. elegans* embryos. *J. Cell Sci.* 121, 306–316.

Basant, A., Lekomtsev, S., Tse, Y.C., Zhang, D., Longhini, K.M., Petronczki, M., and Glotzer, M. (2015). Aurora B Kinase Promotes Cytokinesis by Inducing Centralspindlin Oligomers that Associate with the Plasma Membrane. *Dev. Cell* 33, 204–215.

Bastos, R.N., Cundell, M.J., and Barr, F.A. (2014). KIF4A and PP2A–B56 form a spatially restricted feedback loop opposing Aurora B at the anaphase central spindle. *J. Cell Biol.* 207, 683–693.

Bélisle, J.M., Kunik, D., and Costantino, S. (2009). Rapid multicomponent optical protein patterning. *Lab Chip* 9, 3580–3585.

Ben-Sasson, A., Watson, J., Sheffler, W., Johnson, M., Bittleston, A., Somasundaram, L., Decarreau, J., Jiao, F., Chen, J., Mela, I., et al. (2021). Design of biologically active binary protein 2D materials. *Nature* 589, 468–473.

van Bergeijk, P., Hoogenraad, C.C., and Kapitein, L.C. (2016). Right Time, Right Place: Probing the Functions of Organelle Positioning. *Trends Cell Biol.* 26, 121–134.

- Bergeland, T., Widerberg, J., Bakke, O., and Nordeng, T.W. (2001). Mitotic partitioning of endosomes and lysosomes. *Curr. Biol.* *11*, 644–651.
- Bhuwania, R., Castro-Castro, A., and Linder, S. (2014). Microtubule acetylation regulates dynamics of KIF1C-powered vesicles and contact of microtubule plus ends with podosomes. *Eur. J. Cell Biol.* *93*, 424–437.
- Bieling, P., Telley, I.A., and Surrey, T. (2010). A minimal midzone protein module controls formation and length of antiparallel microtubule overlaps. *Cell* *142*, 420–432.
- Bielska, E., Schuster, M., Roger, Y., Berepiki, A., Soanes, D.M., Talbot, N.J., and Steinberg, G. (2014). Hook is an adapter that coordinates kinesin-3 and dynein cargo attachment on early endosomes. *J. Cell Biol.* *204*, 989–1007.
- Blatner, N., Wilson, M., Lei, C., Hong, W., Murray, D., Williams, R., and Cho, W. (2007). The structural basis of novel endosome anchoring activity of KIF16B kinesin. *EMBO J.* *26*, 3709–3719.
- Blin, G. (2021). Quantitative developmental biology in vitro using micropatterning. *Development* *148*, dev186387.
- Boucrot, E., and Kirchhausen, T. (2007). Endosomal recycling controls plasma membrane area during mitosis. *Proc. Natl Acad. Sci. USA* *104*, 7939–7944.
- Bratman, S. V., and Chang, F. (2007). Stabilization of Overlapping Microtubules by Fission Yeast CLASP. *Dev. Cell* *13*, 812–827.
- Braun, M., Lansky, Z., Fink, G., Ruhnow, F., Diez, S., and Janson, M.E. (2011). Adaptive braking by Ase1 prevents overlapping microtubules from sliding completely apart. *Nat. Cell Biol.* *13*, 1259–1264.
- Bray, S.J. (2006). Notch signalling: a simple pathway becomes complex. *Nat. Rev. Mol. Cell Biol.* *7*, 678–689.
- Bringmann, H., Skiniotis, G., Spilker, A., Kandels-Lewis, S., Vernos, I., and Surrey, T. (2004). A Kinesin-like Motor Inhibits Microtubule Dynamic Instability. *Science* *303*, 1519–1522.
- Bucci, C., Parton, R.G., Mather, I.H., Stunnenberg, H., Simons, K., Hoflack, B., and Zerial, M. (1992). The small GTPase rab5 functions as a regulatory factor in the early endocytic

pathway. *Cell* *70*, 715–728.

Bucciarelli, E., Giansanti, M.G., Bonaccorsi, S., and Gatti, M. (2003). Spindle assembly and cytokinesis in the absence of chromosomes during *Drosophila* male meiosis. *J. Cell Biol.* *160*, 993–999.

Burute, M., and Kapitein, L.C. (2019). Cellular Logistics: Unraveling the Interplay Between Microtubule Organization and Intracellular Transport. *Annu. Rev. Cell Dev. Biol.* *35*, 29–54.

Cabukusta, B., and Neefjes, J. (2018). Mechanisms of lysosomal positioning and movement. *Traffic* *19*, 761–769.

Canman, J.C., Hoffman, D.B., and Salmon, E.D. (2003). The role of pre- and post-anaphase microtubules in the cytokinesis phase of the cell cycle. *Curr. Biol.* *10*, 611–614.

Carlton, J.G., Jones, H., and Eggert, U.S. (2020). Membrane and organelle dynamics during cell division. *Nat. Rev. Mol. Cell Biol.* *21*, 151–166.

Carmena, M., Wheelock, M., Funabiki, H., and Earnshaw, W.C. (2012). The chromosomal passenger complex (CPC): from easy rider to the godfather of mitosis. *Nat. Rev. Mol. Cell Biol.* *13*, 789–803.

Caussinus, E., and Affolter, M. (2016). deGradFP: A System to Knockdown GFP-Tagged Proteins. *Methods in Molecular Biology* *1478*, 177–187.

Chang-Jie, J., and Sonobe, S. (1993). Identification and preliminary characterization of a 65 kDa higher-plant microtubule-associated protein. *J. Cell Sci.* *105*, 891–901.

Chang, F., and Martin, S.G. (2009). Shaping Fission Yeast with Microtubules. *Cold Spring Harb. Perspect. Biol.* *1*, 1347–1348.

Chaudhary, A.R., Lu, H., Krementsova, E.B., Bookwalter, C.S., Trybus, K.M., and Hendricks, A.G. (2019). MAP7 regulates organelle transport by recruiting kinesin-1 to microtubules. *J. Biol. Chem.* *294*, 10160–10171.

Chavrier, P., Parton, R.G., Hauri, H.P., Simons, K., and Zerial, M. (1990). Localization of low molecular weight GTP binding proteins to exocytic and endocytic compartments. *Cell* *62*, 317–329.

Cheerambathur, D.K., Civelekoglu-Scholey, G., Brust-Mascher, I., Sommi, P., Mogilner, A., and Scholey, J.M. (2007). Quantitative analysis of an anaphase B switch: Predicted role for a

- microtubule catastrophe gradient. *J. Cell Biol.* *177*, 995–1004.
- Chesneau, L., Dambourret, D., MacHicoane, M., Kouranti, I., Fukuda, M., Goud, B., and Echard, A. (2012). An ARF6/Rab35 GTPase cascade for endocytic recycling and successful cytokinesis. *Curr. Biol.* *22*, 147–153.
- Chung, J.Y.M., Steen, J.A., and Schwarz, T.L. (2016). Phosphorylation-Induced Motor Shedding Is Required at Mitosis for Proper Distribution and Passive Inheritance of Mitochondria. *Cell Rep.* *16*, 2142–2155.
- Colanzi, A., Hidalgo Carcedo, C., Persic, A., Cericola, C., Turacchio, G., Bonazzi, M., Luini, A., and Corda, D. (2007). The Golgi mitotic checkpoint is controlled by BARS-dependent fission of the Golgi ribbon into separate stacks in G2. *EMBO J.* *26*, 2465–2476.
- Coumailleau, F., Fürthauer, M., Knoblich, J.A., and González-Gaitán, M. (2009). Directional Delta and Notch trafficking in Sara endosomes during asymmetric cell division. *Nature* *458*, 1051–1055.
- Coy, D.L., Wagenbach, M., and Howard, J. (1999a). Kinesin takes one 8-nm step for each ATP that it hydrolyzes. *J. Biol. Chem.* *274*, 3667–3671.
- Coy, D.L., Hancock, W.O., Wagenbach, M., and Howard, J. (1999b). Kinesin's tail domain is an inhibitory regulator of the motor domain. *Nat. Cell Biol.* *1*, 288–292.
- Cross, R.A. (2016). Review: Mechanochemistry of the kinesin-1 ATPase. *Biopolymers* *105*, 476–482.
- D'Avino, P.P., Archambault, V., Przewloka, M.R., Zhang, W., Lilley, K.S., Laue, E., and Glover, D.M. (2007). Recruitment of polo kinase to spindle midzone during cytokinesis requires the Feo/Klp3A complex. *PLoS One* *2*, e572 .
- Davies, T., Kodera, N., Schierle, G.S.K., Rees, E., Erdelyi, M., Kaminski, C.F., Ando, T., and Mishima, M. (2015). CYK4 Promotes Antiparallel Microtubule Bundling by Optimizing MKLP1 Neck Conformation. *PLoS Biol.* *13*, e1002121.
- Demitrack, E.S., and Samuelson, L.C. (2016). Notch regulation of gastrointestinal stem cells. *J. Physiol.* *594*, 4791–4803.
- Derivery, E., Seum, C., Daeden, A., Loubéry, S., Holtzer, L., Jülicher, F., and Gonzalez-Gaitan, M. (2015). Polarized endosome dynamics by spindle asymmetry during asymmetric

- cell division. *Nature* *528*, 280–285.
- Dixit, R., Ross, J.L., Goldman, Y.E., and Holzbaur, E.L.F. (2008). Differential regulation of dynein and kinesin motor proteins by tau. *Science* *319*, 1086–1089.
- Doherty, G.J., and McMahon, H.T. (2009). Mechanisms of Endocytosis. *Annu. Rev. Biochem.* *78*, 857–902.
- Dunster, K., Toh, B.H., and Sentry, J.W. (2002). Early endosomes, late endosomes, and lysosomes display distinct partitioning strategies of inheritance with similarities to Golgi-derived membranes. *Eur. J. Cell Biol.* *81*, 117–124.
- Echard, A., Jollivet, F., Martinez, O., Lacapère, J.J., Rousselet, A., Janoueix-Lerosey, I., and Goud, B. (1998). Interaction of a Golgi-associated kinesin-like protein with Rab6. *Science* *279*, 580–585.
- Emery, G., Hutterer, A., Berdnik, D., Mayer, B., Wirtz-Peitz, F., Gaitan, M.G., and Knoblich, J.A. (2005). Asymmetric Rab11 endosomes regulate delta recycling and specify cell fate in the *Drosophila* nervous system. *Cell* *122*, 763–773.
- Farmaki, T., Ponnambalam, S., Prescott, A.R., Clausen, H., Tang, B.L., Hong, W., and Lucocq, J.M. (1999). Forward and retrograde trafficking in mitotic animal cells. ER-Golgi transport arrest restricts protein export from the ER into COPII-coated structures. *J. Cell Sci.* *112*, 589–600.
- Fehon, R.G., Kooh, P.J., Rebay, I., Regan, C.L., Xu, T., Muskavitch, M.A.T., and Artavanis-Tsakonas, S. (1990). Molecular interactions between the protein products of the neurogenic loci Notch and Delta, two EGF-homologous genes in *Drosophila*. *Cell* *61*, 523–534.
- Fielding, A., Willox, A., Okeke, E., and Royle, S. (2012). Clathrin-mediated endocytosis is inhibited during mitosis. *Proc. Natl Acad. Sci. USA* *109*, 6572–6577.
- Fielding, A.B., Schonteich, E., Matheson, J., Wilson, G., Yu, X., Hickson, G.R.X., Srivastava, S., Baldwin, S.A., Prekeris, R., and Gould, G.W. (2005). Rab11-FIP3 and FIP4 interact with Arf6 and the Exocyst to control membrane traffic in cytokinesis. *EMBO J.* *24*, 3389–3399.
- Flemming, W. (1882). Zellsubstanz, Kern und Zelltheilung. (F.C.W. Vogel, Leipzig)
- Foe, V.E., and Von Dassow, G. (2008). Stable and dynamic microtubules coordinately shape

- the myosin activation zone during cytokinetic furrow formation. *J. Cell Biol.* *183*, 457–470.
- Forth, S., Hsia, K.C., Shimamoto, Y., and Kapoor, T.M. (2014). Asymmetric Friction of Nonmotor MAPs Can Lead to Their Directional Motion in Active Microtubule Networks. *Cell* *157*, 420–432.
- Friedman, D.S., and Vale, R.D. (1999). Single-molecule analysis of kinesin motility reveals regulation by the cargo-binding tail domain. *Nat. Cell Biol.* *1*, 293–297.
- Fu, C., Ward, J.J., Loiodice, I., Velve-Casquillas, G., Nedelec, F.J., and Tran, P.T. (2009). Phospho-Regulated Interaction between Kinesin-6 Klp9p and Microtubule Bundler Ase1p Promotes Spindle Elongation. *Dev. Cell* *17*, 257–267.
- Gaiano, N., and Fishell, G. (2003). The Role of Notch in Promoting Glial and Neural Stem Cell Fates. *Annu. Rev. Neuro.* *25*, 471–490.
- Gaillard, J., Neumann, E., Van Damme, D., Stoppin-Mellet, V., Ebel, C., Barbier, E., Geelen, D., and Vantard, M. (2008). Two microtubule-associated proteins of *Arabidopsis* MAP65s promote antiparallel microtubule bundling. *Mol. Biol. Cell* *19*, 4534–4544.
- Gaska, I., Armstrong, M.E., Alfieri, A., and Forth, S. (2020). The Mitotic Crosslinking Protein PRC1 Acts Like a Mechanical Dashpot to Resist Microtubule Sliding. *Dev. Cell* *54*, 367–378.
- Glotzer, M. (2005). The molecular requirements for cytokinesis. *Science* *307*, 1735–1739.
- Glotzer, M. (2009). The 3Ms of central spindle assembly: microtubules, motors and MAPs. *Nat. Rev. Mol. Cell Biol.* *10*, 9–20.
- Glotzer, M. (2017). Cytokinesis in Metazoa and Fungi. *Cold Spring Harb. Perspect. Biol.* *9*, a022343.
- Gonzalez-Gaitan, M., and Jülicher, F. (2014). The role of endocytosis during morphogenetic signaling. *Cold Spring Harb. Perspect. Biol.* *6*, a016881.
- Gordon, W.R., Vardar-Ulu, D., Histen, G., Sanchez-Irizarry, C., Aster, J.C., and Blacklow, S.C. (2007). Structural basis for autoinhibition of Notch. *Nat. Struct. Mol. Biol.* *14*, 295–300.
- Gordon, W.R., Zimmerman, B., He, L., Miles, L.J., Huang, J., Tiyanont, K., McArthur, D.G., Aster, J.C., Perrimon, N., Loparo, J.J., et al. (2015). Mechanical Allostery: Evidence for a Force Requirement in the Proteolytic Activation of Notch. *Dev. Cell* *33*, 729–736.

Gorvel, J.P., Chavrier, P., Zerial, M., and Gruenberg, J. (1991). rab5 controls early endosome fusion in vitro. *Cell* *64*, 915–925.

Goshima, G., and Vale, R.D. (2003). The roles of microtubule-based motor proteins in mitosis: Comprehensive RNAi analysis in the Drosophila S2 cell line. *J. Cell Biol.* *162*, 1003–1016.

Goshima, G., Mayer, M., Zhang, N., Stuurman, N., and Vale, R.D. (2008). Augmin: A protein complex required for centrosome-independent microtubule generation within the spindle. *J. Cell Biol.* *181*, 421–429.

Goyal, A., Takaine, M., Simanis, V., and Nakano, K. (2011). Dividing the spoils of growth and the cell cycle: The fission yeast as a model for the study of cytokinesis. *Cytoskeleton (Hoboken)*. *68*, 69–88.

Green, R.A., Paluch, E., and Oegema, K. (2012). Cytokinesis in Animal Cells. *Annu. Rev. Cell Dev. Biol.* *28*, 29–58.

Guardia, C.M., Farías, G.G., Jia, R., Pu, J., and Bonifacino, J.S. (2016). BORC Functions Upstream of Kinesins 1 and 3 to Coordinate Regional Movement of Lysosomes Along Different Microtubule Tracks. *Cell Rep.* *17*, 1950–1961.

Güttinger, S., Laurell, E., and Kutay, U. (2009). Orchestrating nuclear envelope disassembly and reassembly during mitosis. *Nat. Rev. Mol. Cell Biol.* *10*, 178–191.

Hackney, D.D. (1988). Kinesin ATPase: Rate-limiting ADP release. *Proc. Natl. Acad. Sci. U. S. A.* *85*, 6314–6318.

Hackney, D.D. (1994). Evidence for alternating head catalysis by kinesin during microtubule-stimulated ATP hydrolysis. *Proc. Natl. Acad. Sci. U. S. A.* *91*, 6865–6869.

Hall, D., and Hedgecock, E. (1991). Kinesin-related gene unc104 is required for axonal transport of synaptic vesicles in *C. elegans*. *Cell* *65*, 837–847.

Hammond, J.W., Cai, D., Blasius, T.L., Li, Z., Jiang, Y., Jih, G.T., Meyhofer, E., and Verhey, K.J. (2009). Mammalian Kinesin-3 motors are dimeric in vivo and move by processive motility upon release of autoinhibition. *PLoS Biol.* *7*, 0650–0663.

Hancock, W.O., and Howard, J. (1999). Kinesin's processivity results from mechanical and chemical coordination between the ATP hydrolysis cycles of the two motor domains. *Proc.*

Natl. Acad. Sci. U. S. A. 96, 13147–13152.

Hannabuss, J., Lera-Ramirez, M., Cade, N.I., Fourniol, F.J., Nédélec, F., and Surrey, T. (2019). Self-Organization of Minimal Anaphase Spindle Midzone Bundles. *Curr. Biol.* 29, 2120–2130.

Hartenstein, V., and Posakony, J.W. (1990). A dual function of the Notch gene in Drosophila sensillum development. *Dev. Biol.* 142, 13–30.

Heald, R., Tournebize, R., Blank, T., Sandaltzopoulos, R., Becker, P., Hyman, A., and Karsenti, E. (1996). Self-organization of microtubules into bipolar spindles around artificial chromosomes in Xenopus egg extracts. *Science* 382, 420–425.

Hehnly, H., and Doxsey, S. (2014). Rab11 Endosomes Contribute to Mitotic Spindle Organization and Orientation. *Dev. Cell* 28, 497–507.

Helenius, J., Brouhard, G., Kalaidzidis, Y., Diez, S., and Howard, J. (2006). The depolymerizing kinesin MCAK uses lattice diffusion to rapidly target microtubule ends. *Nature* 441, 115–119.

Hentrich, C., and Surrey, T. (2010). Microtubule organization by the antagonistic mitotic motors kinesin-5 and kinesin-14. *J. Cell Biol.* 189, 465–480.

Hidalgo Carcedo, C., Donazzi, M., Spano, S., Turacchio, G., Colanzi, A., Luini, A., and Corda, D. (2004). Mitotic Golgi partitioning is driven by the membrane-fissioning protein CtBP3/BARS. *Science* 305, 93–96.

Higuchi, T., and Uhlmann, F. (2005). Stabilization of microtubule dynamics at anaphase onset promotes chromosome segregation. *Nature* 433, 171–176.

Hinze, C., and Boucrot, E. (2018). Endocytosis in proliferating, quiescent and terminally differentiated cells. *J. Cell Sci.* 131, jcs216804.

Hirokawa, N., Noda, Y., Tanaka, Y., and Niwa, S. (2009). Kinesin superfamily motor proteins and intracellular transport. *Nat. Rev. Mol. Cell Biol.* 10, 682–696.

Hirokawa, N., Niwa, S., and Tanaka, Y. (2010). Molecular Motors in Neurons: Transport Mechanisms and Roles in Brain Function, Development, and Disease. *Neuron* 68, 610–638.

Hoepfner, S., Severin, F., Cabezas, A., Habermann, B., Runge, A., Gillooly, D., Stenmark, H., and Zerial, M. (2005). Modulation of receptor recycling and degradation by the

endosomal kinesin KIF16B. *Cell* *121*, 437–450.

Holtzer, L. and Schmidt, T. (2009). The Tracking of Individual Molecules in Cells and Tissues. In *Single Particle Tracking and Single Molecule Energy Transfer*, C. Bräuchle, D.C. Lamb and J. Michaelis ed.(Wiley-VCH Verlag GmbH), pp 25–42.

Hooikaas, P.J., Martin, M., Mühlthaler, T., Kuijntjes, G.J., Peeters, C.A.E., Katrukha, E.A., Ferrari, L., Stucchi, R., Verhagen, D.G.F., Van Riel, W.E., et al. (2019). MAP7 family proteins regulate kinesin-1 recruitment and activation. *J. Cell Biol.* *218*, 1298–1318.

Hou, M.-C., Guertin, D. a, and McCollum, D. (2004). Initiation of cytokinesis is controlled through multiple modes of regulation of the Sid2p-Mob1p kinase complex. *Mol. Cell. Biol.* *24*, 3262–3276.

Hsia, K.C., Wilson-Kubalek, E.M., Dottore, A., Hao, Q., Tsai, K.L., Forth, S., Shimamoto, Y., Milligan, R.A., and Kapoor, T.M. (2014). Reconstitution of the augmin complex provides insights into its architecture and function. *Nat. Cell Biol.* *16*, 852–863.

Hu, C.-K., Coughlin, M., and Mitchison, T.J. (2012). Midbody assembly and its regulation during cytokinesis. *Mol. Biol. Cell* *23*, 1024-1034.

Hu, C.-K.K., Coughlin, M., Field, C.M.M., and Mitchison, T.J.J. (2011). KIF4 regulates midzone length during cytokinesis. *Curr. Biol.* *21*, 815–824.

Huh, D., and Paulsson, J. (2011). Random partitioning of molecules at cell division. *Proc. Natl. Acad. Sci. U. S. A.* *108*, 15004–15009.

Huo, L., Yue, Y., Ren, J., Yu, J., Liu, J., Yu, Y., Ye, F., Xu, T., Zhang, M., and Feng, W. (2012). The CC1-FHA Tandem as a Central Hub for Controlling the Dimerization and Activation of Kinesin-3 KIF1A. *Structure* *20*, 1550–1561.

Hutterer, A., Glotzer, M., and Mishima, M. (2009). Clustering of Centralspindlin Is Essential for Its Accumulation to the Central Spindle and the Midbody. *Curr. Biol.* *19*, 2043–2049.

Hwang, W., Lang, M.J., and Karplus, M. (2008). Force Generation in Kinesin Hinges on Cover-Neck Bundle Formation. *Structure* *16*, 62–71.

Ikegami, K., Heier, R.L., Taruishi, M., Takagi, H., Mukai, M., Shimma, S., Taira, S., Hatanaka, K., Morone, N., Yao, I., et al. (2007). Loss of  $\alpha$ -tubulin polyglutamylation in ROSA22 mice is associated with abnormal targeting of KIF1A and modulated synaptic

- function. Proc. Natl. Acad. Sci. U. S. A. *104*, 3213–3218.
- Ito, A., and Goshima, G. (2015). Microcephaly protein Asp focuses the minus ends of spindle microtubules at the pole and within the spindle. J. Cell Biol. *211*, 999–1009.
- Jagrić, M., Risteski, P., Martinčić, J., Milas, A., and Tolić, I.M. (2021). Optogenetic control of prc1 reveals its role in chromosome alignment on the spindle by overlap length-dependent forces. eLife *10*, e61170.
- Jajoo, R., Jung, Y., Huh, D., Viana, M.P., Rafelski, S.M., Springer, M., and Paulsson, J. (2016). Accurate concentration control of mitochondria and nucleoids. Science *351*, 169–172.
- Janke, C. (2014). The tubulin code: Molecular components, readout mechanisms, functions. J. Cell Biol. *206*, 461–472.
- Janson, M.E., Loughlin, R., Loiodice, I., Fu, C., Brunner, D., Nédélec, F.J., and Tran, P.T. (2007). Crosslinkers and Motors Organize Dynamic Microtubules to Form Stable Bipolar Arrays in Fission Yeast. Cell *128*, 357–368.
- Jantsch-Plunger, V., Gönczy, P., Romano, A., Schnabel, H., Hamill, D., Schnabel, R., Hyman, A.A., and Glotzer, M. (2000). CYK-4: A Rho family GTPase activating protein (GAP) required for central spindle formation and cytokinesis. J. Cell Biol. *149*, 1391–1404.
- Jarriault, S., Brou, C., Logeat, F., Schroeter, E.H., Kopan, R., and Israel, A. (1995). Signalling downstream of activated mammalian Notch. Nature *377*, 355–358.
- Jesch, S.A., Mehta, A.J., Velliste, M., Murphy, R.F., and Linstedt, A.D. (2001). Mitotic Golgi is in a dynamic equilibrium between clustered and free vesicles independent of the ER. Traffic *2*, 873–884.
- Jiang, K., Rezabkova, L., Hua, S., Liu, Q., Capitani, G., Altelaar, A.F.M., Heck, A.J.R., Kammerer, R.A., Steinmetz, M.O., and Akhmanova, A. (2017). Microtubule minus-end regulation at spindle poles by an ASPM–katanin complex. Nat. Cell Biol. *19*, 480–492.
- Jiang, W., Jimenez, G., Wells, N.J., Hope, T.J., Wahl, G.M., Hunter, T., and Fukunaga, R. (1998). PRC1: a human mitotic spindle-associated CDK substrate protein required for cytokinesis. Mol. Cell *2*, 877–885.
- Jongsma, M.L.M., Berlin, I., and Neefjes, J. (2015). On the move: organelle dynamics during mitosis. Trends Cell Biol. *25*, 112–124.

- Kageyama, R., Ohtsuka, T., Shimojo, H., and Imayoshi, I. (2008). Dynamic Notch signaling in neural progenitor cells and a revised view of lateral inhibition. *Nat. Neurosci.* *11*, 1247–1251.
- Kajtez, J., Solomatina, A., Novak, M., Polak, B., Vukušić, K., Rüdiger, J., Cojoc, G., Milas, A., Šumanovac Šestak, I., Risteski, P., Tavano, F., Klemm, A.H., Roscioli, E., Welburn, J., Cimini, D., Glunčić, M., Pavlin, N., and Tolić, I.M. (2016). Overlap microtubules link sister k-fibres and balance the forces on bi-oriented kinetochores. *Nat. Commun.* *7*, 10298.
- Kamasaki, T., O'Toole, E., Kita, S., Osumi, M., Usukura, J., McIntosh, R.R., and Goshima, G. (2013). Augmin-dependent microtubule nucleation at microtubule walls in the spindle. *J. Cell Biol.* *202*, 25–32.
- Kapitein, L.C., Peterman, E.J., Kwok, B.H., Kim, J.H., Kapoor, T.M., and Schmidt, C.F. (2005). The bipolar mitotic kinesin Eg5 moves on both microtubules that it crosslinks. *Nature* *435*, 114–118.
- Kapitein, L.C., Janson, M.E., van den Wildenberg, S.M.J.L., Hoogenraad, C.C., Schmidt, C.F., and Peterman, E.J.G. (2008). Microtubule-Driven Multimerization Recruits ase1p onto Overlapping Microtubules. *Curr. Biol.* *18*, 1713–1717.
- Kapoor, T.M. (2017). Metaphase Spindle Assembly. *Biology* *6*, 8.
- Karsenti, E., Nédélec, F., and Surrey, T. (2006). Modelling microtubule patterns. *Nat. Cell Biol.* *8*, 1204–1211.
- Kashatus, D.F., Lim, K.H., Brady, D.C., Pershing, N.L.K., Cox, A.D., and Counter, C.M. (2011). RALA and RALBP1 regulate mitochondrial fission at mitosis. *Nat. Cell Biol.* *13*, 1108–1115.
- Katajisto, P., Döhla, J., Chaffer, C.L., Pentimikko, N., Marjanovic, N., Iqbal, S., Zoncu, R., Chen, W., Weinberg, R.A., and Sabatini, D.M. (2015). Stem cells. Asymmetric apportioning of aged mitochondria between daughter cells is required for stemness. *Science* *348*, 340–343.
- Kellogg, E.H., Howes, S., Ti, S.-C., Ramírez-Aportela, E., Kapoor, T.M., Chacón, P., and Nogales, E. (2016). Near-atomic cryo-EM structure of PRC1 bound to the microtubule. *Proc. Natl. Acad. Sci. U.S.A.* *113*, 9430–9439.
- Kellogg, E.H., Hejab, N.M.A., Poepsel, S., Downing, K.H., DiMaio, F., and Nogales, E. (2018). Near-atomic model of microtubule-tau interactions. *Science* *360*, 1242–1246.

- Khalil, A.S., Appleyard, D.C., Labno, A.K., Georges, A., Karplus, M., Belcher, A.M., Hwang, W., and Lang, M.J. (2008). Kinesin's cover-neck bundle folds forward to generate force. *Proc. Natl. Acad. Sci. U. S. A.* *105*, 19247–19252.
- Kikkawa, M., Okada, Y., and Hirokawa, N. (2000). 15 Å resolution model of the monomeric kinesin motor, KIF1A. *Cell* *100*, 241–252.
- Klopfenstein, D.R., Tomishige, M., Stuurman, N., and Vale, R.D. (2002). Role of phosphatidylinositol(4,5)bisphosphate organization in membrane transport by the Unc104 kinesin motor. *Cell* *109*, 347–358.
- Knoblauch, B., and Rachubinski, R.A. (2016). How peroxisomes partition between cells. A story of yeast, mammals and filamentous fungi. *Curr. Opin. Cell Biol.* *41*, 73–80.
- Kopan, R., Nye, J.S., and Weintraub, H. (1994). The intracellular domain of mouse Notch: a constitutively activated repressor of myogenesis directed at the basic helix-loop-helix region of MyoD. *Development* *120*, 2385–2396.
- Kopp, P., Lammers, R., Aepfelbacher, M., Woehlke, G., Rudel, T., Machuy, N., Steffen, W., and Linder, S. (2006). The Kinesin KIF1C and Microtubule Plus Ends Regulate Podosome Dynamics in Macrophages. *Mol. Biol. Cell* *17*, 2811–2823.
- Kouranti, I., Sachse, M., Arouche, N., Goud, B., and Echard, A. (2006). Rab35 regulates an endocytic recycling pathway essential for the terminal steps of cytokinesis. *Curr. Biol.* *16*, 1719–1725.
- Kozielski, F. (1997). The crystal structure of dimeric kinesin and implications for microtubule-dependent motility. *Cell* *91*, 985–994.
- Kressmann, S., Campos, C., Castanon, I., Fürthauer, M., and González-Gaitán, M. (2015). Directional Notch trafficking in Sara endosomes during asymmetric cell division in the spinal cord. *Nat. Cell Biol.* *17*, 333–339.
- Krüger, N., and Tolić-Nørrelykke, I.M. (2008). Association of mitochondria with spindle poles facilitates spindle alignment. *Curr. Biol.* *18*, 646–647.
- Krüger, L.K., Sanchez, J.L., Paoletti, A., and Tran, P.T. (2019). Kinesin-6 regulates cell-size-dependent spindle elongation velocity to keep mitosis duration constant in fission yeast. *eLife* *8*, e42182.

Krüger, L.K., Gélin, M., Ji, L., Kikuti, C., Houdusse, A., Théry, M., Blanchoin, L., and Tran, P.T. (2021). Kinesin-6 Klp9 orchestrates spindle elongation by regulating microtubule sliding and growth. *eLife* *10*, e67489.

Kull, F.J., Sablin, E.P., Lau, R., Fletterick, R.J., and Vale, R.D. (1996). Crystal structure of the kinesin motor domain reveals a structural similarity to myosin. *Nature* *380*, 550–555.

Kumar, J., Yu, H., and Sheetz, M.P. (1995). Kinectin, an essential anchor for kinesin-driven vesicle motility. *Science* *267*, 1834–1837.

Kurasawa, Y., Earnshaw, W.C., Mochizuki, Y., Dohmae, N., and Todokoro, K. (2004). Essential roles of KIF4 and its binding partner PRC1 in organized central spindle midzone formation. *EMBO J.* *23*, 3237–3248.

Labbé, K., Murley, A., and Nunnari, J. (2014). Determinants and Functions of Mitochondrial Behavior. *Annu. Rev. Cell Dev. Biol.* *30*, 357–391.

Lansky, Z., Braun, M., Lüdecke, A., Schlierf, M., Ten Wolde, P.R., Janson, M.E., and Diez, S. (2015). Diffusible crosslinkers generate directed forces in microtubule networks. *Cell* *160*, 1159–1168.

Lawrence, C.J., Dawe, R.K., Christie, K.R., Cleveland, D.W., Dawson, S.C., Endow, S.A., Goldstein, L.S., Goodson, H.V., Hirokawa, N., Howard, J., et al. (2004). A standardized kinesin nomenclature. *J. Cell Biol.* *167*, 19–22.

Lee, K.-Y., Esmaeili, B., Zealley, B., and Mishima, M. (2015). Direct interaction between centralspindlin and PRC1 reinforces mechanical resilience of the central spindle. *Nat. Commun.* *6*, 7290.

Lee, P.L., Ohlson, M.B., and Pfeffer, S.R. (2015). The Rab6-regulated KIF1C kinesin motor domain contributes to Golgi organization. *eLife* *4*. e06029

Lehmann, R., Jiménez, F., Dietrich, U., and Campos-Ortega, J.A. (1983). On the phenotype and development of mutants of early neurogenesis in *Drosophila melanogaster*. *Wilhelm Roux's Arch. Dev. Biol.* *192*, 62–74.

Lekomtsev, S., Su, K.C., Pye, V.E., Blight, K., Sundaramoorthy, S., Takaki, T., Collinson, L.M., Cherepanov, P., Divecha, N., and Petronczki, M. (2012). Centralspindlin links the mitotic spindle to the plasma membrane during cytokinesis. *Nature* *492*, 276–279.

- Lessard, D. V., Zinder, O.J., Hotta, T., Verhey, K.J., Ohi, R., and Berger, C.L. (2019). Polyglutamylation of tubulin's C-terminal tail controls pausing and motility of kinesin-3 family member KIF1A. *J. Biol. Chem.* **294**, 6353–6363.
- Lieber, T., Kidd, S., Alcamo, E., Corbin, V., and Young, M.W. (1993). Antineurogenic phenotypes induced by truncated Notch proteins indicate a role in signal transduction and may point to a novel function for Notch in nuclei. *Genes Dev.* **7**, 1949–1965.
- Lipka, J., Kapitein, L.C., Jaworski, J., and Hoogenraad, C.C. (2016). Microtubule-binding protein doublecortin-like kinase 1 (DCLK1) guides kinesin-3-mediated cargo transport to dendrites. *EMBO J.* **35**, 302–318.
- Liu, J., Wang, Z., Jiang, K., Zhang, L., Zhao, L., Hua, S., Yan, F., Yang, Y., Wang, D., Fu, C., et al. (2009). PRC1 cooperates with CLASP1 to organize central spindle plasticity in mitosis. *J. Biol. Chem.* **284**, 23059–23071.
- Lo, K.Y., Kuzmin, A., Unger, S.M., Petersen, J.D., and Silverman, M.A. (2011). KIF1A is the primary anterograde motor protein required for the axonal transport of dense-core vesicles in cultured hippocampal neurons. *Neurosci. Lett.* **491**, 168–173.
- Loeffler, D., Wehling, A., Schneiter, F., Zhang, Y., Müller-Bötticher, N., Hoppe, P.S., Hilsenbeck, O., Kokkaliaris, K.D., Endele, M., and Schroeder, T. (2019). Asymmetric lysosome inheritance predicts activation of haematopoietic stem cells. *Nature* **573**, 426–429.
- Loiodice, I., Staub, J., Setty, T.G., Nguyen, N.-P.T., Paoletti, A., and Tran, P.T. (2005). Ase1p Organizes Antiparallel Microtubule Arrays during Interphase and Mitosis in Fission Yeast. *Mol. Biol. Cell* **16**, 1756–1768.
- Loubéry, S., and González-Gaitán, M. (2014). Monitoring Notch/Delta Endosomal Trafficking and Signaling in Drosophila. *Methods Enzymol.* **534**, 301–321.
- Loubéry, S., Seum, C., Moraleda, A., Daeden, A., Fürthauer, M., and Gonzalez-Gaitan, M. (2014). Uninflatable and Notch Control the Targeting of Sara Endosomes during Asymmetric Division. *Curr. Biol.* **24**, 2142–2148.
- Lowe, M., and Barr, F.A. (2007). Inheritance and biogenesis of organelles in the secretory pathway. *Nat. Rev. Mol. Cell Biol.* **8**, 429–439.
- Lu, B., Ackerman, L., Jan, L.Y., and Jan, Y.N. (1999). Modes of Protein Movement that Lead to the Asymmetric Localization of Partner of Numb during Drosophila Neuroblast

Division. Mol. Cell 4, 883–891.

Lu, L., Ladinsky, M.S., and Kirchhausen, T. (2009). Cisternal organization of the endoplasmic reticulum during mitosis. Mol. Biol. Cell 20, 3471–3480.

Mallavarapu, A., Sawin, K., and Mitchison, T. (1999). A switch in microtubule dynamics at the onset of anaphase B in the mitotic spindle of *Schizosaccharomyces pombe*. Curr. Biol. 9, 1423–1428.

Manenica, M., Koprivec, I., Štimac, V., Simunić, J., and Tolić, I.M. (2020). Augmin regulates kinetochore tension and spatial arrangement of spindle microtubules by nucleating bridging fibers. BioRxiv 2020.09.10.291740.

Mani, N., Jiang, S., Neary, A.E., Wijeratne, S.S., and Subramanian, R. (2021). Differential regulation of single microtubules and bundles by a three-protein module. Nat. Chem. Biol. 17, 964–974.

Maruyama, Y., Sugawa, M., Yamaguchi, S., Davies, T., Osaki, T., Kobayashi, T., Yamagishi, M., Takeuchi, S., Mishima, M., and Yajima, J. (2021). CYK4 relaxes the bias in the off-axis motion by MKLP1 kinesin-6. Commun. Biol. 4, 180.

Mastronarde David N. , McDonald Kent L, Rubai Ding, and J.R.M.L. (1993). Interpolar Spindle Microtubules in PTK Cells. J. Cell Biol. 123, 1475–1489.

Mauvezin, C., Neisch, A.L., Ayala, C.I., Kim, J., Beltrame, A., Braden, C.R., Gardner, M.K., Hays, T.S., and Neufeld, T.P. (2016). Coordination of autophagosome–lysosome fusion and transport by a Klp98A–Rab14 complex in *Drosophila*. J. Cell Sci. 129, 971–982.

Mazumdar, M., Sundareshan, S., and Misteli, T. (2004). Human chromokinesin KIF4A functions in chromosome condensation and segregation. J. Cell Biol. 166, 613–620.

McCaffrey, M.W., Bielli, A., Cantalupo, G., Mora, S., Roberti, V., Santillo, M., Drummond, F., and Bucci, C. (2001). Rab4 affects both recycling and degradative endosomal trafficking. FEBS Lett. 495, 21–30.

McFaline-Figueroa, J.R., Vevea, J., Swayne, T.C., Zhou, C., Liu, C., Leung, G., Boldogh, I.R., and Pon, L.A. (2011). Mitochondrial quality control during inheritance is associated with lifespan and mother-daughter age asymmetry in budding yeast. Aging Cell 10, 885–895.

Mickolajczyk, K.J., and Hancock, W.O. (2017). Kinesin Processivity Is Determined by a

- Kinetic Race from a Vulnerable One-Head-Bound State. *Biophys. J.* *112*, 2615–2623.
- Milic, B., Andreasson, J.O.L., Hancock, W.O., and Block, S.M. (2014). Kinesin processivity is gated by phosphate release. *Proc. Natl. Acad. Sci. U.S.A.* *111*, 14136–14140.
- Mishima, M. (2017). Preparation of centralspindlin as an active heterotetramer of kinesin and GTPase activating protein subunits for in vitro structural and functional assays. *Methods Cell Biol.* *137*, 371-385.
- Mishima, M., Kaitna, S., and Glotzer, M. (2002). Central spindle assembly and cytokinesis require a kinesin-like protein/RhoGAP complex with microtubule bundling activity. *Dev. Cell* *2*, 41–54.
- Mishima, M., Pavicic, V., Gruneberg, U., Nigg, E.A., and Glotzer, M. (2004). Cell cycle regulation of central spindle assembly. *Nature* *430*, 908–913.
- Mishra, P., and Chan, D.C. (2014). Mitochondrial dynamics and inheritance during cell division, development and disease. *Nat. Rev. Mol. Cell Biol.* *15*, 634–646.
- Mitsushima, M. (2010). Revolving movement of a dynamic cluster of actin filaments during mitosis. *J. Cell Biol.* *191*, 453–462.
- Miyazaki, M., Chiba, M., Eguchi, H., Ohki, T., and Ishiwata, S. (2015). Cell-sized spherical confinement induces the spontaneous formation of contractile actomyosin rings in vitro. *Nat. Cell Biol.* *17*, 480–489.
- Mogre, S.S., Brown, A.I., and Koslover, E.F. (2020). Getting around the cell: physical transport in the intracellular world. *Phys. Biol.* *17*, 061003.
- Mollinari, C., Kleman, J.P., Jiang, W., Schoehn, G., Hunter, T., and Margolis, R.L. (2002). PRC1 is a microtubule binding and bundling protein essential to maintain the mitotic spindle midzone. *J. Cell Biol.* *157*, 1175–1186.
- Monroy, B.Y., Sawyer, D.L., Ackermann, B.E., Borden, M.M., Tan, T.C., and Ori-McKenney, K.M. (2018). Competition between microtubule-associated proteins directs motor transport. *Nat. Commun.* *9*, 1487.
- Monroy, B.Y., Tan, T.C., Oclaman, J.M., Han, J.S., Simó, S., Niwa, S., Nowakowski, D.W., McKenney, R.J., and Ori-McKenney, K.M. (2020). A Combinatorial MAP Code Dictates Polarized Microtubule Transport. *Dev. Cell* *53*, 60-72.

Montagne, C., and Gonzalez-Gaitan, M. (2014). Sara endosomes and the asymmetric division of intestinal stem cells. *Development* *141*, 2014–2023.

Moore, A.S., Coscia, S.M., Simpson, C.L., Ortega, F.E., Wait, E.C., Heddleston, J.M., Nirschl, J.J., Obara, C.J., Guedes-Dias, P., Boecker, C.A., et al. (2021). Actin cables and comet tails organize mitochondrial networks in mitosis. *Nature* *591*, 659–664.

Mumm, J.S., Schroeter, E.H., Saxena, M.T., Griesemer, A., Tian, X., Pan, D.J., Ray, W.J., and Kopan, R. (2000). A Ligand-Induced Extracellular Cleavage Regulates  $\gamma$ -Secretase-like Proteolytic Activation of Notch1. *Mol. Cell* *5*, 197–206.

Murthy, K., and Wadsworth, P. (2008). Dual role for microtubules in regulating cortical contractility during cytokinesis. *J. Cell Sci.* *121*, 2350–2359.

Nguyen, P.A., Field, C.M., and Mitchison, T.J. (2018). Prc1E and Kif4A control microtubule organization within and between large *Xenopus* egg asters. *Mol. Biol. Cell* *29*, 304–316.

Nishimura, Y., and Yonemura, S. (2006). Centralspindlin regulates ECT2 and RhoA accumulation at the equatorial cortex during cytokinesis. *J. Cell Sci.* *119*, 104–114.

Nislow, C., Lombillo, V.A., Kuriyama, R., and McIntosh, J.R. (1992). A plus-end-directed motor enzyme that moves antiparallel microtubules in vitro localizes to the interzone of mitotic spindles. *Nature* *359*, 543–547.

Nunes Bastos, R., Gandhi, S.R., Baron, R.D., Gruneberg, U., Nigg, E.A., and Barr, F.A. (2013). Aurora B suppresses microtubule dynamics and limits central spindle size by locally activating KIF4A. *J. Cell Biol.* *202*, 605–621.

Okada, Y., and Hirokawa, N. (1999). A processive single-headed motor: Kinesin superfamily protein KIF1A. *Science* *283*, 1152–1157.

Okada, Y., and Hirokawa, N. (2000). Mechanism of the single-headed processivity: Diffusional anchoring between the K-loop of kinesin and the C terminus of tubulin. *Proc. Natl. Acad. Sci. U. S. A.* *97*, 640–645.

Okada, Y., Higuchi, H., and Hirokawa, N. (2003). Processivity of the single-headed kinesin KIF1A through biased binding to tubulin. *Nature* *424*, 574–577.

Orci, L., Glick, B.S., and Rothman, J.E. (1986). A new type of coated vesicular carrier that appears not to contain clathrin: Its possible role in protein transport within the Golgi stack.

Cell 46, 171–184.

Oriola, D., Roth, S., Dogterom, M., and Casademunt, J. (2015). Formation of helical membrane tubes around microtubules by single-headed kinesin KIF1A. *Nat. Commun.* 6, 8025.

Ovesný, M., Křížek, P., Borkovec, J., Švindrych, Z., and Hagen, G.M. (2014). ThunderSTORM: a comprehensive ImageJ plug-in for PALM and STORM data analysis and super-resolution imaging. *Bioinformatics* 30, 2389–2390.

Park, Y.Y., and Cho, H. (2012). Mitofusin 1 is degraded at G2/M phase through ubiquitylation by MARCH5. *Cell Div.* 7, 25.

Parks, A.L., Klueg, K.M., Stout, J.R., and Muskavitch, M.A.T. (2000). Ligand endocytosis drives receptor dissociation and activation in the Notch pathway. *Development* 127, 1373–1385.

Pavicic-Kaltenbrunner, V., Mishima, M., and Glotzer, M. (2007). Cooperative Assembly of CYK-4/MgcRacGAP and ZEN-4/MKLP1 to Form the Centralspindlin Complex. *Mol. Biol. Cell* 19, 308–317.

Pellman, D., Bagget, M., Tu, Y.H., Fink, G.R., and Tu, H. (1995). Two microtubule-associated proteins required for anaphase spindle movement in *Saccharomyces cerevisiae*. *J. Cell Biol.* 130, 1373–1385.

Pinot, M., Chesnel, F., Kubiak, J.Z., Arnal, I., Nedelec, F.J., and Gueroui, Z. (2009). Effects of Confinement on the Self-Organization of Microtubules and Motors. *Curr. Biol.* 19, 954–960.

Polak, B., Risteski, P., Lesjak, S., and Tolić, I.M. (2017). PRC 1-labeled microtubule bundles and kinetochore pairs show one-to-one association in metaphase . *EMBO Rep.* 18, 217–230.

Portran, D., Gaillard, J., Vantard, M., and Thery, M. (2013). Quantification of MAP and molecular motor activities on geometrically controlled microtubule networks. *Cytoskeleton* 70, 12–23.

Poulson, D.F. (1940). The effects of certain X-chromosome deficiencies on the embryonic development of *Drosophila melanogaster*. *J. Exp. Zool.* 83, 271–325.

- Pu, J., Schindler, C., Jia, R., Jarnik, M., Backlund, P., and Bonifacino, J.S. (2015). BORC, a Multisubunit Complex that Regulates Lysosome Positioning. *Dev. Cell* 33, 176–188.
- Puhka, M., Vihinen, H., Joensuu, M., and Jokitalo, E. (2007). Endoplasmic reticulum remains continuous and undergoes sheet-to-tubule transformation during cell division in mammalian cells. *J. Cell Biol.* 179, 895–909.
- Raich, W.B., Moran, A.N., Rothman, J.H., and Hardin, J. (1998). Cytokinesis and midzone microtubule organization in *Caenorhabditis elegans* require the kinesin-like protein ZEN-4. *Mol. Biol. Cell* 9, 2037–2049.
- Rappaport, R. (1971). Cytokinesis in Animal Cells. *Int. Rev. Cytol.* 31, 169–215.
- Rashid, D.J., Bononi, J., Tripet, B.P., Hodges, R.S., and Pierce, D.W. (2005). Monomeric and dimeric states exhibited by the kinesin-related motor protein KIF1A. *J. Pept. Res.* 65, 538–549.
- Reber, S., and Hyman, A.A. (2015). Emergent Properties of the Metaphase Spindle. *Cold Spring Harb. Perspect. Biol.* 7, a015784.
- Ren, J., Zhang, Y., Wang, S., Huo, L., Lou, J., and Feng, W. (2018). Structural Delineation of the Neck Linker of Kinesin-3 for Processive Movement. *J. Mol. Biol.* 430, 2030–2041.
- Rhyu, M.S., Jan, L.Y., and Jan, Y.N. (1994). Asymmetric distribution of numb protein during division of the sensory organ precursor cell confers distinct fates to daughter cells. *Cell* 76, 477–491.
- Rice, S., Lin, A.W., Safer, D., Hart, C.L., Naber, N., Carragher, B.O., Cain, S.M., Pechatnikova, E., Wilson-Kubalek, E.M., Whittaker, M., et al. (1999). A structural change in the kinesin motor protein that drives motility. *Nature* 402, 778–784.
- Rice, S., Cui, Y., Sindelar, C., Naber, N., Matuska, M., Vale, R., and Cooke, R. (2003). Thermodynamic properties of the kinesin neck-region docking to the catalytic core. *Biophys. J.* 84, 1844–1854.
- Rincon, S.A., Lamson, A., Blackwell, R., Syrovatkina, V., Fraisier, V., Paoletti, A., Betterton, M.D., and Tran, P.T. (2017). Kinesin-5-independent mitotic spindle assembly requires the antiparallel microtubule crosslinker Ase1 in fission yeast. *Nat. Commun.* 8, 15286 .

- Rink, J., Ghigo, E., Kalaidzidis, Y., and Zerial, M. (2005). Rab Conversion as a Mechanism of Progression from Early to Late Endosomes. *Cell* *122*, 735–749.
- Rios, R.M., and Bornens, M. (2003). The Golgi apparatus at the cell centre. *Curr. Opin. Cell Biol.* *15*, 60–66
- Rogers, S.L., Rogers, G.C., Sharp, D.J., and Vale, R.D. (2002). Drosophila EB1 is important for proper assembly, dynamics, and positioning of the mitotic spindle. *J. Cell Biol.* *158*, 873–884.
- Roostalu, J., Rickman, J., Thomas, C., Nédélec, F., and Surrey, T. (2018). Determinants of Polar versus Nematic Organization in Networks of Dynamic Microtubules and Mitotic Motors. *Cell* *175*, 796-808.
- Rosenfeld, S.S., Jefferson, G.M., and King, P.H. (2001). ATP Reorients the Neck Linker of Kinesin in Two Sequential Steps. *J. Biol. Chem.* *276*, 40167–40174.
- Roux, K.J., Kim, D.I., and Burke, B. (2013). BioID: A Screen for Protein-Protein Interactions. *Current Protocols in Protein Science* *91*, 19.23.1-19.23.14.
- Saxton, W.M., and McIntosh, J.R. (1987). Interzone microtubule behavior in late anaphase and telophase spindles. *J. Cell Biol.* *105*, 875–886.
- Scarabelli, G., Soppina, V., Yao, X.-Q., Atherton, J., Moores, C.A., Verhey, K.J., and Grant, B.J. (2015). Mapping the processivity determinants of the Kinesin-3 motor domain. *Biophys. J.* *109*, 1537–1540.
- Schindelin, J., Arganda-Carreras, I., Frise, E., Kaynig, V., Longair, M., Pietzsch, T., Preibisch, S., Rueden, C., Saalfeld, S., Schmid, B., et al. (2012). Fiji: an open-source platform for biological-image analysis. *Nat. Methods* *9*, 676–682.
- Schlager, M.A., Kapitein, L.C., Grigoriev, I., Burzynski, G.M., Wulf, P.S., Keijzer, N., De Graaff, E., Fukuda, M., Shepherd, I.T., Akhmanova, A., et al. (2010). Pericentrosomal targeting of Rab6 secretory vesicles by Bicaudal-D-related protein 1 (BICDR-1) regulates neuritogenesis. *EMBO J.* *29*, 1637–1651.
- Schnitzer, M.J., and Block, S.M. (1997). Kinesin hydrolyses one ATP per 8-nm step. *Nature* *388*, 386–390.
- Schroeter, E.H., Kisslinger, J.A., and Kopan, R. (1998). Notch-1 signalling requires ligand-

- induced proteolytic release of intracellular domain. *Nature* *393*, 382–386.
- Schuyler, S.C., Liu, J.Y., and Pellman, D. (2003). The molecular function of Ase1p evidence for a MAP-dependent midzone-specific spindle matrix. *J. Cell Biol.* *160*, 517–528.
- Schweiguth, F. (2015). Asymmetric cell division in the *Drosophila* bristle lineage: from the polarization of sensory organ precursor cells to Notch-mediated binary fate decision. *Wiley Interdiscip. Rev. Dev. Biol.* *4*, 299–309.
- Sekine, Y., Okada, Y., Noda, Y., Kondo, S., Aizawa, H., Takemura, R., and Hirokawa, N. (1994). A novel microtubule-based motor protein (KIF4) for organelle transports, whose expression is regulated developmentally. *J. Cell Biol.* *127*, 187–201.
- Shastry, S., and Hancock, W. (2010). Neck linker length determines the degree of processivity in kinesin-1 and kinesin-2 motors. *Curr. Biol.* *20*, 939–943.
- Shastry, S., and Hancock, W.O. (2011). Interhead tension determines processivity across diverse N-terminal kinesins. *Proc. Natl. Acad. Sci. U. S. A.* *108*, 16253–16258.
- She, Z.-Y., Wei, Y.-L., Lin, Y., Li, Y.-L., and Lu, M.-H. (2019). Mechanisms of the Ase1/PRC1/MAP65 family in central spindle assembly. *Biol. Rev.* *94*, 2033–2048.
- Shigematsu, H., Imasaki, T., Doki, C., Sumi, T., Aoki, M., Uchikubo-Kamo, T., Sakamoto, A., Tokuraku, K., Shirouzu, M., and Nitta, R. (2018). Structural insight into microtubule stabilization and kinesin inhibition by Tau family MAPs. *J. Cell Biol.* *217*, 4155–4163.
- Short, B., Preisinger, C., Schaetzky, J., Kopajtich, R., and Barr, F.A. (2002). The Rab6 GTPase Regulates Recruitment of the Dynactin Complex to Golgi Membranes. *Curr. Biol.* *12*, 1792–1795.
- Siddiqui, N., and Straube, A. (2017). Intracellular cargo transport by kinesin-3 motors. *Biochem.* *82*, 803–815.
- Siddiqui, N., Zwetsloot, A.J., Bachmann, A., Roth, D., Hussain, H., Brandt, J., Kaverina, I., and Straube, A. (2019). PTPN21 and Hook3 relieve KIF1C autoinhibition and activate intracellular transport. *Nat. Commun.* *10*, 2693.
- Silljé, H., Nagel, S., Körner, R., and Nigg, E. (2006). HURP is a Ran-importin beta-regulated protein that stabilizes kinetochore microtubules in the vicinity of chromosomes. *Curr. Biol.* *16*, 731–742.

- Sindelar, C. V., Budny, M.J., Rice, S., Naber, N., Fletterick, R., and Cooke, R. (2002). Two conformations in the human kinesin power stroke defined by X-ray crystallography and EPR spectroscopy. *Nat. Struct. Biol.* *9*, 844–848.
- Sirajuddin, M., Rice, L.M., and Vale, R.D. (2014). Regulation of microtubule motors by tubulin isotypes and post-translational modifications. *Nat. Cell Biol.* *16*, 335–344.
- Smyth, J.T., Beg, A.M., Wu, S., Putney, J.W., Rusan, N.M., and Rusan, N.M. (2012). Phosphoregulation of STIM1 leads to exclusion of the endoplasmic reticulum from the mitotic spindle. *Curr. Biol.* *22*, 1487–1493.
- Soppina, V., and Verhey, K.J. (2014). The family-specific K-loop influences the microtubule on-rate but not the superprocessivity of kinesin-3 motors. *Mol. Biol. Cell* *25*, 2161–2170.
- Soppina, V., Norris, S.R., Dizaji, A.S., Kortus, M., Veatch, S., Peckham, M., and Verhey, K.J. (2014). Dimerization of mammalian kinesin-3 motors results in superprocessive motion. *Proc. Natl. Acad. Sci. U. S. A.* *111*, 5562–5567.
- Stewart, J.B., and Chinnery, P.F. (2020). Extreme heterogeneity of human mitochondrial DNA from organelles to populations. *Nat. Rev. Genet.* *22*, 106–118.
- Strale, P.-O., Azioune, A., Bugnicourt, G., Lecomte, Y., Chahid, M., and Studer, V. (2016). Multiprotein Printing by Light-Induced Molecular Adsorption. *Adv. Mater.* *28*, 2024–2029.
- Struhl, G., and Adachi, A. (1998). Nuclear Access and Action of Notch In Vivo. *Cell* *93*, 649–660.
- Su, K.-C., Bement, W.M., Petronczki, M., and von Dassow, G. (2014). An astral simulacrum of the central spindle accounts for normal, spindle-less, and anucleate cytokinesis in echinoderm embryos. *Mol. Biol. Cell* *25*, 4049–4062.
- Su, K.C., Takaki, T., and Petronczki, M. (2011). Targeting of the RhoGEF Ect2 to the Equatorial Membrane Controls Cleavage Furrow Formation during Cytokinesis. *Dev. Cell* *21*, 1104–1115.
- Subramanian, R., Wilson-Kubalek, E.M., Arthur, C.P., Bick, M.J., Campbell, E.A., Darst, S.A., Milligan, R.A., and Kapoor, T.M. (2010). Insights into Antiparallel Microtubule Crosslinking by PRC1, a Conserved Nonmotor Microtubule Binding Protein. *Cell* *142*, 433–443.

- Subramanian, R., Ti, S.-C., Tan, L., Darst, S.A., and Kapoor, T.M. (2013). Marking and Measuring Single Microtubules by PRC1 and Kinesin-4. *Cell* *154*, 377–390.
- Surrey, T., Nédélec, F., Leibler, S., and Karsenti, E. (2001). Physical properties determining self-organization of motors and microtubules. *Science* *292*, 1167–1171.
- Suzuki, K., Miyazaki, M., Takagi, J., Itabashi, T., and Ishiwata, S. (2017). Spatial confinement of active microtubule networks induces large-scale rotational cytoplasmic flow. *Proc. Natl. Acad. Sci.* *114*, 2922–2927.
- Taguchi, N., Ishihara, N., Jofuku, A., Oka, T., and Mihara, K. (2007). Mitotic phosphorylation of dynamin-related GTPase Drp1 participates in mitochondrial fission. *J. Biol. Chem.* *282*, 11521–11529.
- Tang, D., Yuan, H., Vielemeyer, O., Perez, F., and Wang, Y. (2012). Sequential phosphorylation of GRASP65 during mitotic Golgi disassembly. *Biol. Open* *1*, 1204–1214.
- Tao, L., Fasulo, B., Warecki, B., and Sullivan, W. (2016). Tum/RacGAP functions as a switch activating the Pav/kinesin-6 motor. *Nat. Commun.* *7*, 11182.
- Tatsumoto, T., Xie, X., Blumenthal, R., Okamoto, I., and Miki, T. (1999). Human ECT2 Is an Exchange Factor for Rho GTPases, Phosphorylated in G2/M Phases, and Involved in Cytokinesis. *J. Cell Biol.* *147*, 921–927.
- Tomishige, M., Klopfenstein, D.R., and Vale, R.D. (2002). Conversion of Unc104/KIF1A kinesin into a processive motor after dimerization. *Science* *297*, 2263–2267.
- Tomishige, M., Stuurman, N., and Vale, R.D. (2006). Single-molecule observations of neck linker conformational changes in the kinesin motor protein. *Nat. Struct. Mol. Biol.* *13*, 887–894.
- Tong, Y., Tempel, W., Wang, H., Yamada, K., Shen, L., Senisterra, G., MacKenzie, F., Chishti, A., and Park, H. (2010). Phosphorylation-independent dual-site binding of the FHA domain of KIF13 mediates phosphoinositide transport via centaurin alpha1. *Proc. Natl. Acad. Sci. U. S. A.* *107*, 20346–20351.
- Touré, A., Dorseuil, O., Morin, L., Timmons, P., Jégou, B., Reibel, L., and Gacon, G. (1998). MgRacGAP, a new human GTPase-activating protein for Rac and Cdc42 similar to Drosophila rotundRacGAP gene product, is expressed in male germ cells. *J. Biol. Chem.* *273*, 6019–6023.

- Triclin, S., Inoue, D., Gaillard, J., Htet, Z.M., DeSantis, M.E., Portran, D., Derivery, E., Aumeier, C., Schaadel, L., John, K., et al. (2021). Self-repair protects microtubules from destruction by molecular motors. *Nat. Mater.* *20*, 883–891.
- Uehara, R., and Goshima, G. (2010). Functional central spindle assembly requires de novo microtubule generation in the interchromosomal region during anaphase. *J. Cell Biol.* *191*, 259–267.
- Uehara, R., Nozawa, R., Tomioka, A., Petry, S., Vale, R.D., Obuse, C., and Goshima, G. (2009). The augmin complex plays a critical role in spindle microtubule generation for mitotic progression and cytokinesis in human cells. *Proc. Natl. Acad. Sci. U. S. A.* *106*, 6998–7003.
- Ueno, H., Huang, X., Tanaka, Y., and Hirokawa, N. (2011). KIF16B/Rab14 molecular motor complex is critical for early embryonic development by transporting FGF receptor. *Dev. Cell* *20*, 60–71.
- Vale, R.D. (2003). The molecular motor toolbox for intracellular transport. *Cell* *112*, 467–480.
- Vale, R.D., and Fletterick, R.J. (1997). The design plan of kinesin motors. *Annu. Rev. Cell Dev. Biol.* *13*, 745–777.
- Vale, R.D., Reese, T.S., and Sheetz, M.P. (1985a). Identification of a novel force-generating protein, kinesin, involved in microtubule-based motility. *Cell* *42*, 39–50.
- Vale, R.D., Schnapp, B.J., Reese, T.S., and Sheetz, M.P. (1985b). Organelle, bead, and microtubule translocations promoted by soluble factors from the squid giant axon. *Cell* *40*, 559–569.
- Varga, V., Helenius, J., Tanaka, K., Hyman, A.A., Tanaka, T.U., and Howard, J. (2006). Yeast kinesin-8 depolymerizes microtubules in a length-dependent manner. *Nat. Cell Biol.* *8*, 957–962.
- Venkateswarlu, K., Hanada, T., and Chishti, A.H. (2005). Centaurin- $\alpha$ 1 interacts directly with kinesin motor protein KIF13B. *J. Cell Sci.* *118*, 2471–2484.
- Verbrugghe, K.J.C., and White, J.G. (2004). SPD-1 Is Required for the Formation of the Spindle Midzone but Is Not Essential for the Completion of Cytokinesis in *C. elegans* Embryos. *Curr. Biol.* *14*, 1755–1760.

- Verhey, K.J., and Gaertig, J. (2007). The tubulin code. *Cell Cycle* *6*, 2152–2160.
- Verni, F., Somma, M.P., Gunsalus, K.C., Bonaccorsi, S., Belloni, G., Goldberg, M.L., and Gatti, M. (2004). Feo, the Drosophila Homolog of PRC1, Is Required for Central-Spindle Formation and Cytokinesis. *Curr. Biol.* *14*, 1569–1575.
- Vukušić, K., and Tolić, I.M. (2021). Anaphase B: Long-standing models meet new concepts. *Semin. Cell Dev. Biol.* *117*, 127–139.
- Vukušić, K., Buđa, R., Bosilj, A., Milas, A., Pavin, N., and Tolić, I.M. (2017). Microtubule Sliding within the Bridging Fiber Pushes Kinetochore Fibers Apart to Segregate Chromosomes. *Dev. Cell* *43*, 11-23.
- Vukušić, K., Ponjavić, I., Buda, R., Risteski, P., and Tolić, I.M. (2021). Microtubule-sliding modules based on kinesins EG5 and PRC1-dependent KIF4A drive human spindle elongation. *Dev. Cell* *56*, 1253-1267.
- Wagner, E., and Glotzer, M. (2016). Local RhoA activation induces cytokinetic furrows independent of spindle position and cell cycle stage. *J. Cell Biol.* *213*, 641–649.
- Wakefield, J.G., Bonaccorsi, S., and Gatti, M. (2001). The Drosophila Protein Asp Is Involved in Microtubule Organization during Spindle Formation and Cytokinesis. *J. Cell Biol.* *153*, 637–648.
- Wang, Y., Seemann, J., Pypaert, M., Shorter, J., and Warren, G. (2003). A direct role for GRASP65 as a mitotically regulated Golgi stacking factor. *EMBO J.* *22*, 3279–3290.
- Warren, G., and Wickner, W. (1996). Organelle inheritance. *Cell* *84*, 395–400.
- Watson, J.L., Aich, S., Drabek, A.A., Blacklow, S.C., Chin, J., and Derivery, E. (2021). High-efficacy subcellular micropatterning of proteins using fibrinogen anchors. *J. Cell Biol.* *220*. e202009063
- Wei, J.H., and Seemann, J. (2009). The mitotic spindle mediates inheritance of the Golgi ribbon structure. *J. Cell Biol.* *184*, 391–397.
- Werner, M., Munro, E., and Glotzer, M. (2007). Astral Signals Spatially Bias Cortical Myosin Recruitment to Break Symmetry and Promote Cytokinesis. *Curr. Biol.* *17*, 1286–1297.
- White, J.G., and Borisy, G.G. (1983). On the mechanisms of cytokinesis in animal cells. *J.*

Theor. Biol. 101, 289–316.

Wichmann, H., Hengst, L., and Gallwitz, D. (1992). Endocytosis in yeast: Evidence for the involvement of a small GTP-binding protein (Ypt7p). *Cell* 71, 1131–1142.

Wijeratne, S., and Subramanian, R. (2018). Geometry of antiparallel microtubule bundles regulates relative sliding and stalling by PRC1 and kif4A. *eLife* 7, e32595.

Williams, B.C., Riedy, M.F., Williams, E. V., Gatti, M., and Goldberg, M.L. (1995). The Drosophila kinesin-like protein KLP3A is a midbody component required for central spindle assembly and initiation of cytokinesis. *J. Cell Biol.* 129, 709–723.

Wilson, G.M., Fielding, A.B., Simon, G.C., Yu, X., Andrews, P.D., Haines, R.S., Frey, A.M., Peden, A.A., Gould, G.W., and Prekeris, R. (2005). The FIP3-Rab11 protein complex regulates recycling endosome targeting to the cleavage furrow during late cytokinesis. *Mol. Biol. Cell* 16, 849–860.

Yaffe, M.P., Harata, D., Verde, F., Eddison, M., Toda, T., and Nurse, P. (1996). Microtubules mediate mitochondrial distribution in fission yeast. *Proc. Natl. Acad. Sci. U. S. A.* 93, 11664–11668.

Yamada, K.H., Hanada, T., and Chishti, A.H. (2007). The effector domain of human Dlg tumor suppressor acts as a switch that relieves autoinhibition of kinesin-3 motor GAKIN/KIF13B. *Biochemistry* 46, 10039–10045.

Yildiz, A., Tomishige, M., Vale, R., and Selvin, P. (2004). Kinesin walks hand-over-hand. *Science* 303, 676–678.

Yildiz, A., Tomishige, M., Gennerich, A., and Vale, R. (2008). Intramolecular strain coordinates kinesin stepping behavior along microtubules. *Cell* 134, 1030–1041.

Yoshimura, Y., Terabayashi, T., and Miki, H. (2010). Par1b/MARK2 Phosphorylates Kinesin-Like Motor Protein GAKIN/KIF13B To Regulate Axon Formation. *Mol. Cell. Biol.* 30, 2206–2219.

Yu, C.-H., Redemann, S., Wu, H.-Y., Kiewisz, R., Yoo, T.Y., Conway, W., Farhadifar, R., Müller-Reichert, T., and Needleman, D. (2019). Central-spindle microtubules are strongly coupled to chromosomes during both anaphase A and anaphase B. *Mol. Biol. Cell* 30, 2503–2514.

- Yu, X., Prekeris, R., and Gould, G.W. (2007). Role of endosomal Rab GTPases in cytokinesis. *Eur. J. Cell Biol.* *86*, 25–35.
- Yüce, Ö., Piekny, A., and Glotzer, M. (2005). An ECT2-centralspindlin complex regulates the localization and function of RhoA. *J. Cell Biol.* *170*, 571–582.
- Zaal, K.J.M., Smith, C.L., Polishchuk, R.S., Altan, N., Cole, N.B., Ellenberg, J., Hirschberg, K., Presley, J.F., Roberts, T.H., Siggia, E., et al. (1999). Golgi membranes are absorbed into and reemerge from the ER during mitosis. *Cell* *99*, 589–601.
- Zaniewski, T.M., Gicking, A.M., Fricks, J., and Hancock, W.O. (2020). A kinetic dissection of the fast and superprocessive kinesin-3 KIF1A reveals a predominant one-head-bound state during its chemomechanical cycle. *J. Biol. Chem.* *295*, 17889–17903.
- Zeng, C., Younger-Shepherd, S., Jan, L.Y., and Jan, Y.N. (1998). Delta and Serrate are redundant Notch ligands required for asymmetric cell divisions within the Drosophila sensory organ lineage. *Genes Dev.* *12*, 1086–1091.
- Zhu, C., and Jiang, W. (2005). Cell cycle-dependent translocation of PRC1 on the spindle by Kif4 is essential for midzone formation and cytokinesis. *Proc. Natl. Acad. Sci. U. S. A.* *102*, 343–348.
- Zhu, C., Lau, E., Schwarzenbacher, R., Bossy-Wetzel, E., and Jiang, W. (2006). Spatiotemporal control of spindle midzone formation by PRC1 in human cells. *Proc. Natl. Acad. Sci. U. S. A.* *103*, 6196–6201.